Contribution to the study and design of antennas for the generation of radio waves bearing orbital angular momentum

Wenlong Wei

ANNÉE 2016

THÈSE / UNIVERSITÉ DE RENNES 1
sous le sceau de l'Université Bretagne Loire

pour le grade de

DOCTEUR DE L'UNIVERSITÉ DE RENNES 1

Mention : Traitement du Signal et Télécommunications

Ecole doctorale Matisse

présentée par

Wenlong WEI

Préparée à l'unité de recherche UMR CNRS 6164 - IETR
Institut d'Electronique et de Télécommunications de Rennes
ISTIC – UFR Informatique Electronique

Contribution à l'étude et la conception d'antennes pour la génération d'ondes radiofréquences transportant du moment angulaire orbital

Thèse soutenue à Rennes le 21/11/2016

devant le jury composé de :

Olivier PASCAL
Professeur, Université Toulouse 3 / *rapporteur*

Eric LHEURETTE
Professeur, Université de Lille 1 / *rapporteur*

Xavier BEGAUD
Professeur, Télécom Paris Tech / *examinateur*

Habiba OUSLIMANI
Professeur, Université Paris Ouest Nanterre La Défense / *examinateur*

Olivier EMILE
Professeur, Université de Rennes 1 / *examinateur*

Kouroch MAHDJOUBI
Professeur, Université de Rennes 1 / *directeur de thèse*

Christian BROUSSEAU
Maitre de conférences - HDR, Université de Rennes 1 / *co-directeur de thèse*

Ala Sharaiha
Professeur, Université de Rennes 1 / *invité*

Acknowledgements

First and foremost I would like to express my deepest gratitude to my supervisor Prof. Kouroch Mahdjoubi for providing me the chance to study at IETR, University of Rennes 1, and for directing this thesis. His scientific intuition, knowledge, guidance and patience have contributed significantly to this work and inspired me a lot.

I would also like to express my deep gratitude to Dr. Christian Brousseau for his co-supervision and the great support he has given me throughout this work, and to Prof. Olivier Emile for valuable discussions and suggestions. Their contributions make this thesis possible.

In addition, I would like to thank Prof. Ala Sharaiha for supporting me to attend the EuCAP conference and for helping present the paper at the LAPC conference.

Many thanks to Laurent Le Coq, Xavier Morvan, Jean-Christophe Le Cun, Eric Moricet, Christophe Guiton and David Levalois for technical advices and willingness to help me realize the antennas and perform the measurements.

I also wish to express my gratitude to all the staff at IETR for passing through a beautiful and unforgettable time together and for the help they have given me during these years. Especially I thank the PhD student Abdullah Haskou for his enthusiasm and the secretary Noëlle Le Ber for her kindness.

I would like to thank my parents for all their support during my study. I thank my wife Wenlin Kuai for her encouragement and company and for giving birth to our baby which is the biggest gift for me till now in my life.

I would also like to acknowledge the China Scholarship Council (CSC) for the scholarship support during my PhD study.

Résumé en Français

I. Introduction et objectifs

Le fait que les ondes électromagnétiques (EM) peuvent porter du moment angulaire est connu depuis assez longtemps, mais c'est seulement en 1992 qu'il a été démontré théoriquement par Allen *et al.* [1] que certains types de faisceaux pouvaient porter un moment angulaire orbital (OAM en anglais) de $\ell\hbar$ par photon, où ℓ est un nombre entier appelé "charge topologique" ou l'ordre du mode OAM. Alors que la phase d'une onde plane habituelle est constante sur le front d'onde, la phase α des ondes OAM possède une variation linéaire le long de la coordonnée angulaire φ (angle de roulis): $\alpha = \ell\varphi$. Si l'on décrit le champ dans le front d'onde en coordonnées polaires, il varie comme $e^{-j\ell\varphi}.f_\ell(r).e^{-jkz}$, où k est le vecteur d'onde, z, l'axe de propagation et $f_\ell(r)$, la variation du champ le long de la coordonnée radiale.

Les propriétés de l'OAM ont suscité beaucoup d'intérêt dans de nombreux domaines. Les premières études concernant l'interaction de l'OAM avec la matière ont cité comme exemples d'applications potentielles, les pinces optiques [2], le lecteur optique de micromachines [3], le piégeage et guidage des atomes [4], etc. Dans le domaine radiofréquence, l'OAM a été proposé pour améliorer l'efficacité spectrale [5-9] dans les communications sans fil, en créant plusieurs sous-canaux de propagation correspondant aux différents modes ℓ du moment angulaire orbital. Il existe également des applications possibles dans le domaine de l'identification d'objet [10] ou celui des radars [11-13].

Depuis 1992, plusieurs méthodes ont été proposées pour générer des ondes portant de l'OAM. Dans le champ optique, il existe principalement trois techniques: la lame de phase spirale [22-24], les modes Laguerre-Gauss [1, 28, 29] et le réseau diffractant [34]. Dans le domaine de la radio, deux grandes familles d'antennes ont été proposées pour générer des ondes OAM. La première est basée sur la transformation de l'onde plane en une onde OAM. Pour cela on peut citer: la lame de phase spirale [40, 41], la lame de phase plate [42, 43], le réseau diffractant [45] et le réflecteur en spirale [6, 47]. La deuxième famille est basée sur l'emploi de réseaux circulaires de dipôle à phase contrôlée [5, 36].

La deuxième méthode est en réalité une étude purement théorique qui n'a pas été suivie de réalisation et d'expérimentation à cause de complexités d'ordre pratique. L'objectif de cette thèse est donc de concevoir et de réaliser de nouveaux types d'antenne dans la gamme des

radiofréquences pour répondre aux besoins actuels et futurs des applications nécessitant des ondes électromagnétiques ayant un moment angulaire orbital.

II. Génération d'OAM avec déphaseur circulaire et réseau d'antennes patch

Nous présentons d'abord un réseau circulaire à commande de phase à l'aide d'un déphaseur original pour générer le mode $\ell = 1$ du moment angulaire orbital. Ce générateur d'ondes OAM utilise quatre antennes « patch » alimentées par une ligne de transmission circulaire originale fonctionnant à la fréquence 2.5 GHz.

1. Conception d'antenne

Pour la création d'un mode OAM $\ell = 1$, nous avons utilisé $N = 4$ antennes avec un écart de phase entre élément successifs de 90° ($2\pi\ell/N = \pi/2$ radians). A cet effet, nous avons conçu un déphaseur circulaire qui non seulement fournit l'écart de phase de 90° mais aussi assure l'adaptation d'impédance à chaque discontinuité en utilisant des transformateur quart-d'onde (Fig. 1a). Le déphaseur fonctionne à 2.5 GHz et dispose de 5 ports: le port1 est l'entrée et est adaptée à 50 Ω, tandis que les autres ports sont adaptés à 100Ω et utilisés comme sorties pour alimenter les antennes patch situées sur un cercle. Le logiciel HFSS a été utilisé pour optimiser la longueur et la largeur des arcs micro-rubans et permettre l'adaptation de l'antenne, ainsi que l'obtention d'une amplitude uniforme et un écart de phase de 90° au niveau des ports de sortie.

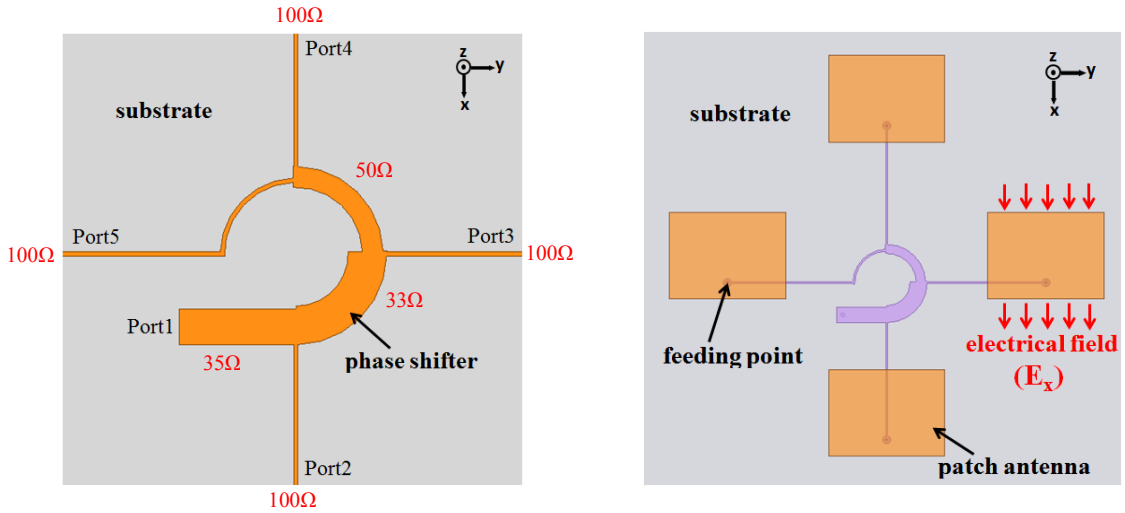

(a) (b)

Fig. 1: Les modèles de simulation : (a) Géométrie du déphaseur circulaire; (b) Configuration de l'antenne OAM

Le réseau d'antenne est composé de 4 « patchs » micro-rubans comme le montre la Fig. 1b. La longueur et la largeur d'une antenne patch sont respectivement de 27.4 mm et de 36.5

mm. Le déphaseur et le réseau d'antennes patch sont fabriqués sur des substrats FR4 ayant une épaisseur de 1.6 mm et une permittivité relative de 4.4. Les patches sont connectés au déphaseur à travers des sondes. Pour satisfaire l'adaptation d'impédance, la position du point d'alimentation est optimisée à 5.1 mm du bord inférieur de l'antenne patch. Les prototypes réalisés du déphaseur et l'antenne OAM sont présentés à la Fig. 2.

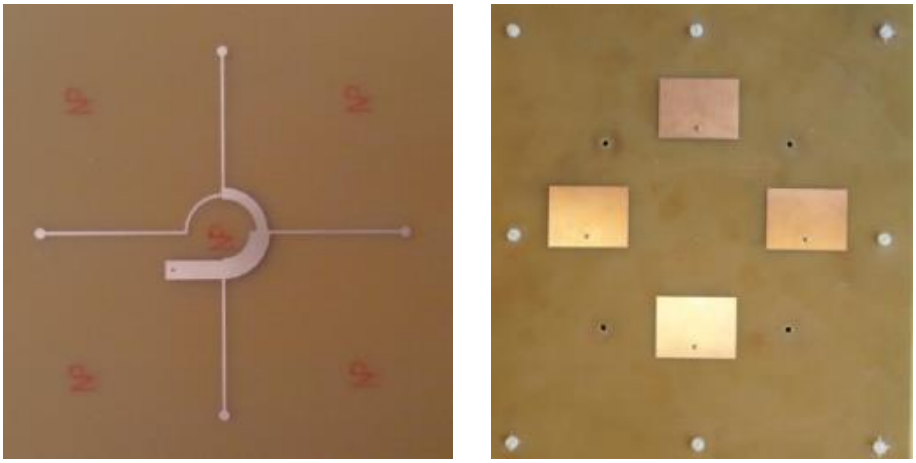

Fig. 2: Prototypes du déphaseur (à gauche) et du réseau d'antennes à onde OAM (à droite)

2. Résultats de simulation et de mesure

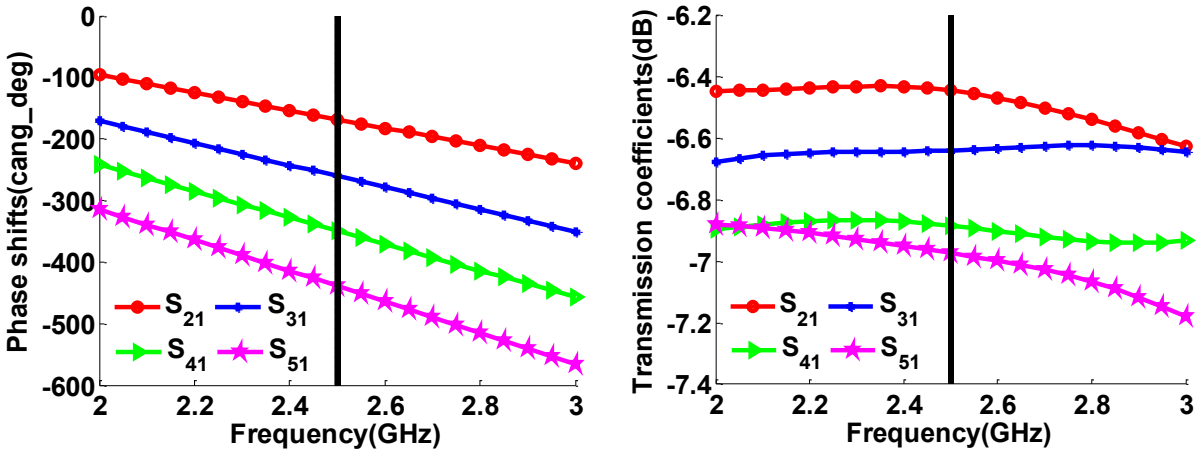

Fig. 3: Caractéristiques simulées du déphaseur: les déphasages (à gauche) et les coefficients de transmission (à droite) à 2.5 GHz. Le déphasage des S_{21}, S_{31}, S_{41}, S_{51} est de -168 ° -261 ° -350 ° -439°, respectivement; et leur amplitude, de -6.4 dB, -6,6 dB, -6,9 dB, -7 dB.

Les résultats simulés du déphaseur sont présentés à la Fig. 3. Nous pouvons observer qu'à 2.5 GHz (ligne verticale noire), entre deux ports voisins, l'erreur de phase est de 4° et l'erreur d'amplitude de 0.6 dB. Ainsi, le déphaseur a un très bon accord avec les spécifications requises.

La Fig. 4 montre la cartographie 2D de l'amplitude et la phase de la composante E_x du champ électrique dans un plan perpendiculaire parallèle à la surface de l'antenne et situé à 60

mm au-dessus de celle-ci. On peut voir qu'au centre, l'amplitude est beaucoup plus faible qu'en périphérie, ce qui montre la présence du vortex caractéristique des ondes à OAM. La phase tourne autour du centre avec un déphasage de 2π en un tour. Ceci démontre en effet que l'amplitude et la phase correspondent à une onde ayant un OAM de $\ell = 1$. La Fig. 5 présente les diagrammes de rayonnement et de phase en 3D de l'antenne OAM pour la polarisation principale E_x (voir Fig. 1b). On retrouve sur le diagramme 3D de l'amplitude, le trou central caractéristique des ondes OAM. La forme en spirale du diagramme de phase, tracée en coordonnées polaires, correspondant à la variation linéaire de la phase en fonction de l'angle de roulis (φ, sur la Fig. 5).

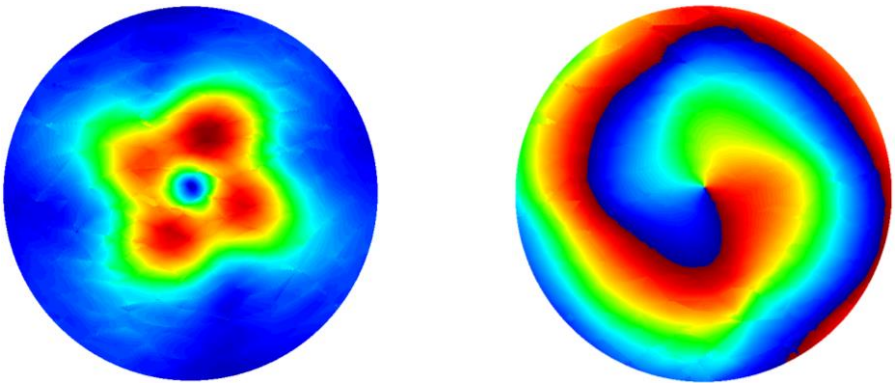

Fig. 4: Cartographie 2D en amplitude (à gauche) et en phase (à droit) du composant E_x pour l'antenne OAM à 2.5 GHz

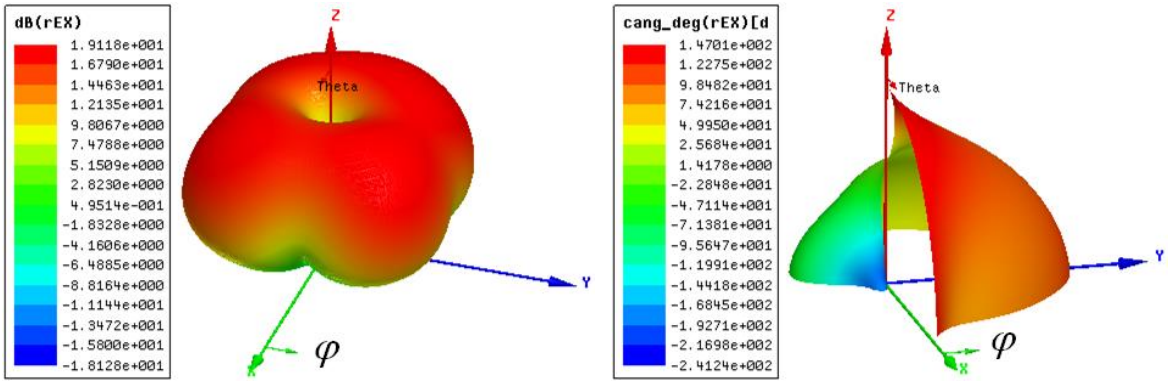

(a) (b)

Fig. 5: Diagrammes de rayonnement et de phase en 3D de l'antenne OAM à 2.5 GHz : (a) Amplitude; (b) Phase.

L'adaptation de l'antenne, montrée sur la Fig. 6, est bonne autour de la fréquence centrale de 2.5 GHz. Les S_{11} simulés et mesurés ont la même forme. Les diagrammes de rayonnement 2D de la Fig. 7a, correspondant aux coupes xOz ($\varphi = 0°$) et yOz ($\varphi = 90°$), montrent également un très bon accord entre les résultats de mesure et de simulation. Les diagrammes de phase sont

représentés à la Fig. 7b. Nous y comparons les résultats théoriques, simulés et expérimentaux pour trois coupes du diagramme 3D de la Fig. 5b, correspondant aux angles d'ouverture θ de 10°, 30° et 50°. Aussi bien les résultats simulés que mesurés, assurent une variation de phase de 360° sur un tour correspondant au mode d'OAM $\ell = 1$. La différence entre les résultats théoriques et expérimentaux est très faible pour les angles θ faibles, mais augmente avec θ. Par conséquent, le comportement « OAM » idéal est respecté aux voisinages du tourbillon central et ce, jusqu'environ une ouverture de $\theta = 30°$, où l'amplitude du faisceau est maximale.

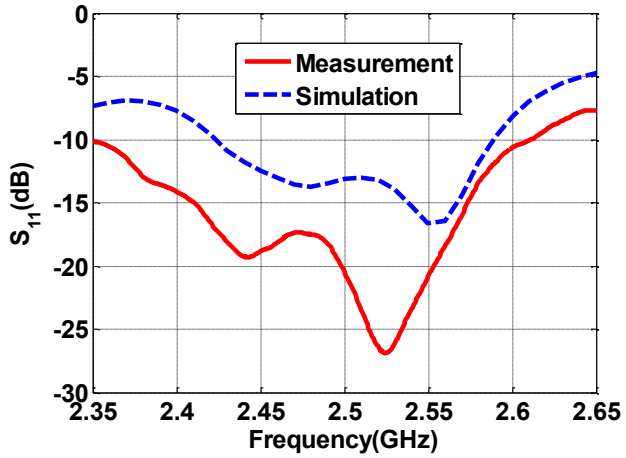

Fig. 6: Coefficient de réflexion S_{11} simulé et mesuré de l'antenne OAM

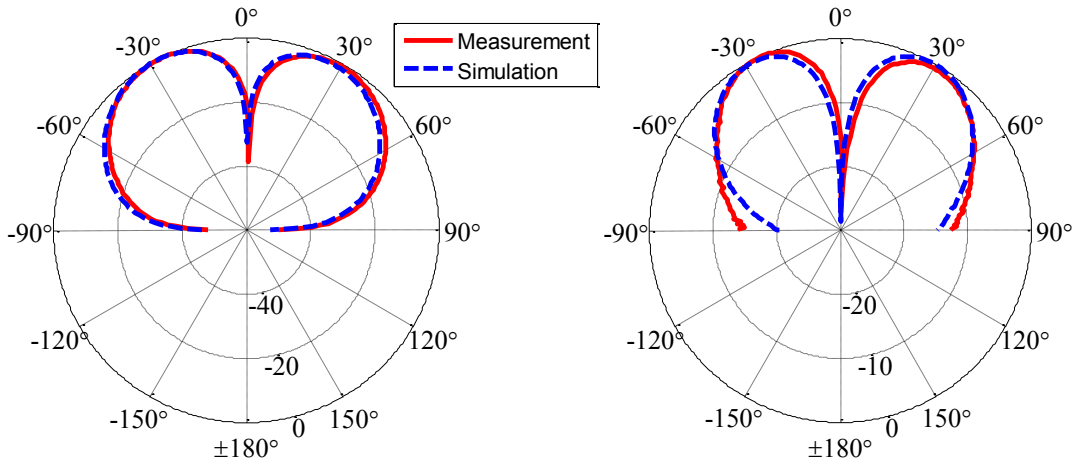

E-plane (coupe xOz) *E-plane (coupe yOz)*

(a)

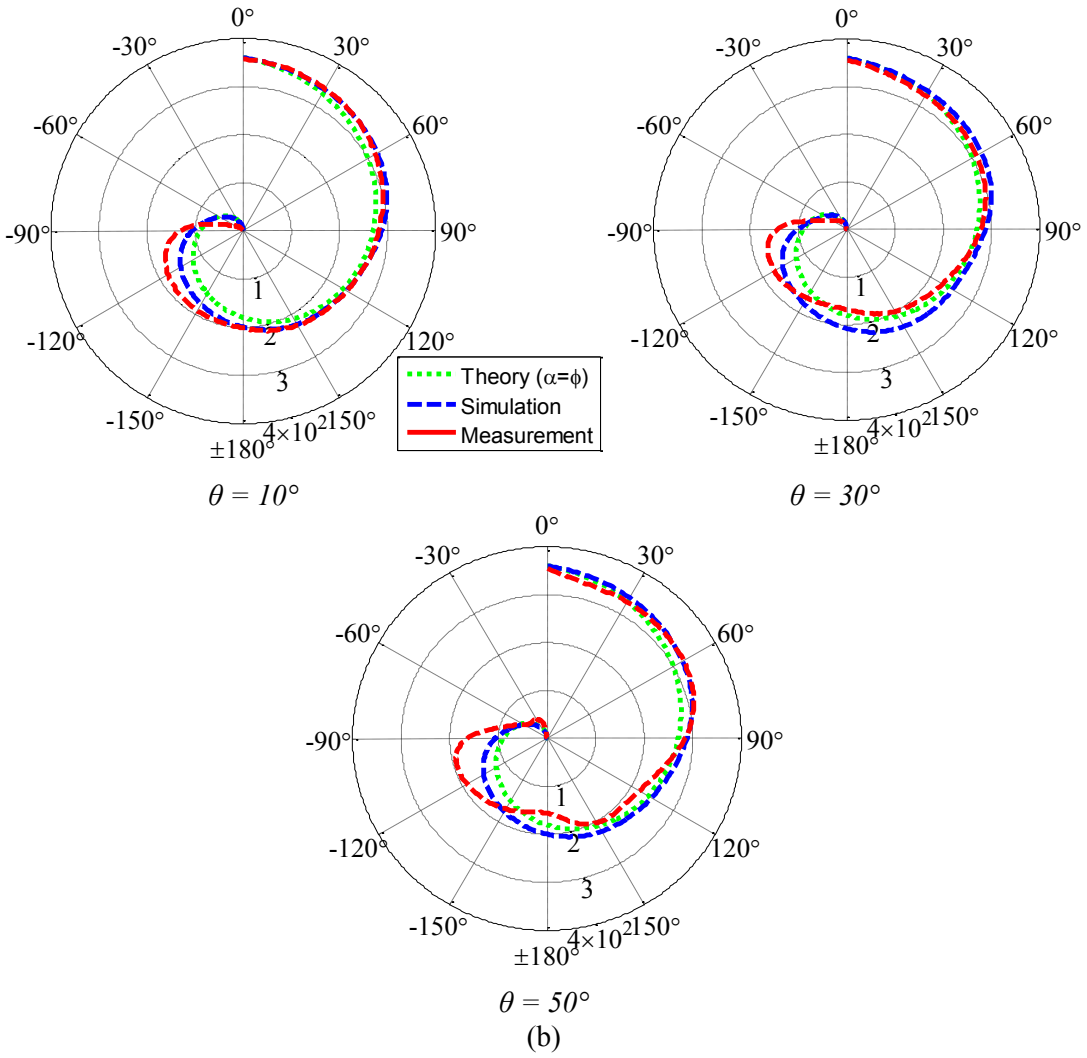

Fig. 7: Diagrammes de rayonnement 2D simulé et mesuré de l'antenne OAM à 2.5GHz : (a) Diagrammes en amplitude normalisés; (b) Diagrammes en phase normalisée (en degrés).

III. Conception d'une antenne directive OAM en utilisant la cavité de Fabry-Perot

L'antenne précédente est simple, compact et facile à réaliser, mais sa directivité est relativement faible. Dans ce chapitre, nous allons l'intégrons dans une cavité Fabry-Perot (FP) pour améliorer sa directivité.

1. Structure de base de la cavité Fabry-Perot

La cavité FP est très sélective en fréquence et a été utilisée à l'origine, comme un filtre de fréquence en optique. Dans les applications antennaires, elle est souvent utilisée en tant que filtre spatial pour améliorer les performances de l'antenne telles que la directivité [53-55].

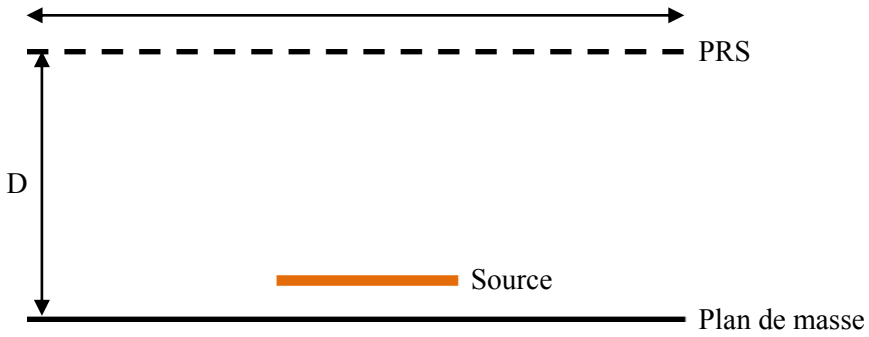

Fig. 8: Structure de la cavité FP

La structure de la cavité FP est représentée à la Fig. 8. Elle est généralement composée d'un plan de masse, qui élimine le rayonnement arrière, d'une source primaire située à l'intérieur et d'une surface partiellement réfléchissante (PRS). Le plan de masse et le PRS sont séparés d'une distance *D* qui est l'épaisseur de la cavité, et est donnée par [63]:

$$D = \frac{c}{4\pi f_0 \cos\theta_0}[\alpha + (2n+1)\pi], \quad \text{n} = 0, 1, 2, 3\ldots\ldots \tag{1}$$

où *c* est la vitesse de la lumière à l'intérieur de la cavité (espace libre), f_0, la fréquence de travail, *n*, un nombre entier correspondant au numéro de mode de cavité, α, la phase du coefficient de réflexion du PRS et θ_0, l'angle de dépointage du faisceau sortant. Dans notre étude, *n* est choisi à 0 pour utiliser le premier mode et donc l'épaisseur *D* minimale.

2. Conception d'antenne directive à base de cavité FP

Nous avons étudiée 2 structures différentes pour la surface réfléchissante PRS : une avec des lignes micro-rubans métallisés déposés sur un substrat FR4 et l'autre composée de tubes métalliques. Ici nous allons présenter la deuxième qui a été retenue pour la réalisation. La géométrie de cette antenne FP OAM est représentée à la Fig. 9. Étant donné que les ondes OAM générées par le réseau circulaire sont plus directives lorsque le rayon du réseau devient plus grand, nous choisissons un rayon de réseau de 110 mm à la fréquence de 2.5 GHz. La directivité de l'antenne dépend de la réflectivité de la surface PRS (c'est-à-dire du diamètre et de la périodicité des tubes), de l'épaisseur *D* de la cavité et de la superficie du PRS. Pour obtenir une meilleure directivité de l'antenne OAM, ces paramètres ont été optimisés à l'aide du logiciel HFSS et nous obtenons les valeurs suivantes :

- Diamètre des tubes: 4 mm
- Période des tubes: 26 mm
- Epaisseur de la cavité: 58 mm
- Ouverture de la cavité: 600 mm × 600 mm

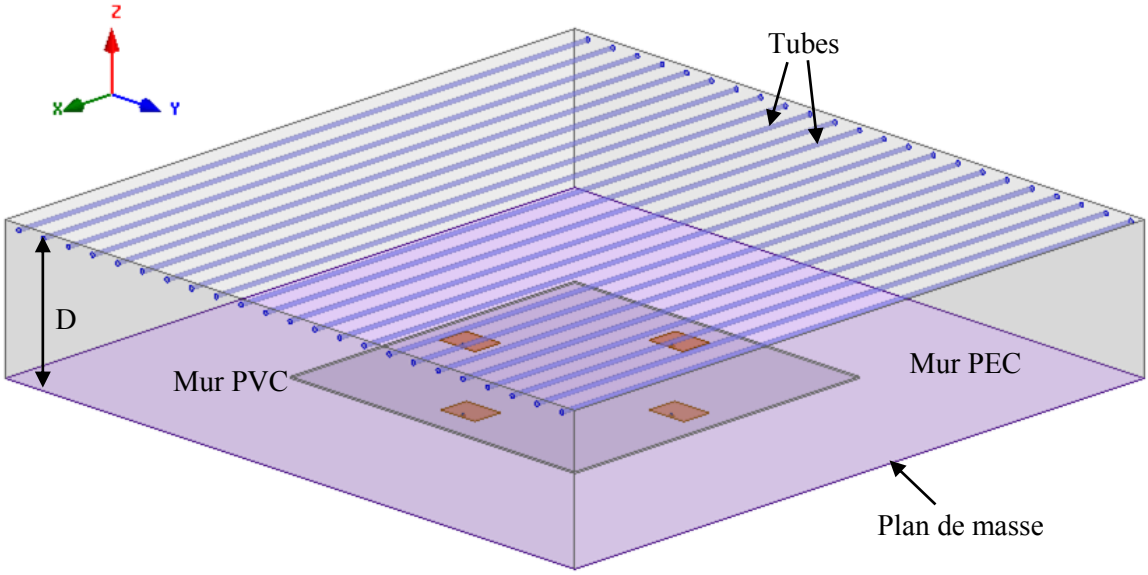

Fig. 9: Géométrie de l'antenne à cavité FP

La cavité FP est fermée sur les côtés à l'aide de 4 murs: 2 murs PEC (Perfect electric conductor) dans le plan E et 2 murs PVC (PolyChlorure de Vinyle) dans le plan H. Les murs PEC sont utilisés pour diminuer le niveau des lobes secondaires du diagramme de rayonnement dans le plan H. Les murs PVC sont utilisés pour supporter les tubes métalliques. D'après les simulations, afin de diminuer le niveau des lobes secondaires dans le plan E, l'épaisseur du mur PVC doit être aussi faible que possible. Cependant, cette épaisseur doit également permettre aux murs PVC de bien assembler les murs PEC et le plan de masse. Pour répondre aux deux exigences, nous avons finalement choisi une épaisseur de 6 mm.

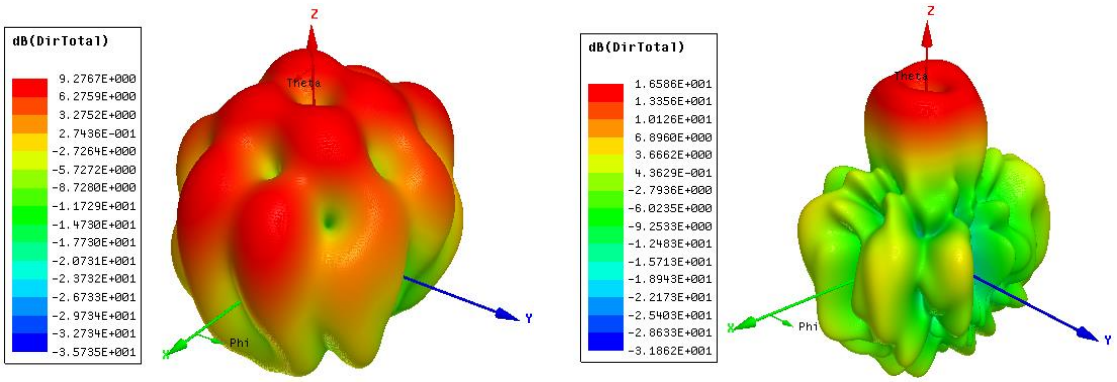

(a) (b)

Fig. 10 Les diagrammes de rayonnement 3D du réseau d'antenne OAM : (a) sans cavité FP; (b) avec cavité FP

La Fig. 10 présente les diagrammes de rayonnement 3D du réseau d'antennes patch (rayon de réseau égal à 110 mm) avec et sans cavité FP. On remarque la présence d'un vortex au centre,

qui est caractéristique des ondes OAM. En outre, avec l'utilisation de la cavité FP, la directivité de l'antenne est augmentée et les lobes secondaires sont sensiblement atténués.

Pour donner une meilleure vue de l'influence de la cavité FP sur la directivité de l'antenne OAM, nous faisons une comparaison des diagrammes de rayonnement E-plan à la Fig. 11. On peut voir qu'avec l'utilisation de la cavité FP, la directivité de l'antenne passe de 7 à 16.6 dB. La directivité maximale est obtenue pour un angle de 10 °.

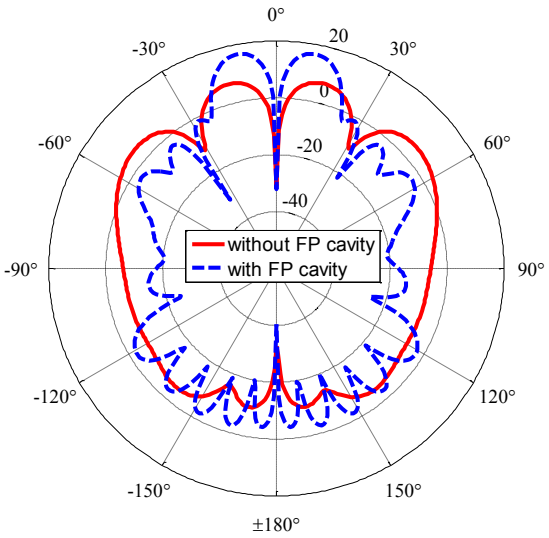

Fig. 11: Comparaison des diagrammes de rayonnement dans le plan E de l'antenne OAM avec et sans cavité FP (rayon de réseau égal à 110mm)

La géométrie de l'antenne à cavité FP excitée par le réseau de patch et son déphaseur associé est montrée à la Fig. 12. Dans cette conception, le diamètre des tubes est fixé à 4 mm. La directivité maximale est obtenue pour une période de tubes de 26 mm, une épaisseur de cavité de 58 mm et une surface de réfléchissante de 600 mm × 600 mm.

Pour obtenir un bon diagramme de rayonnement et satisfaire l'adaptation d'impédance, la longueur et la largeur de l'antenne patch unique sont optimisés à respectivement 26.5 mm et 36.5 mm et la position du point d'alimentation est à 7.4 mm du bord inférieur de l'antenne patch.

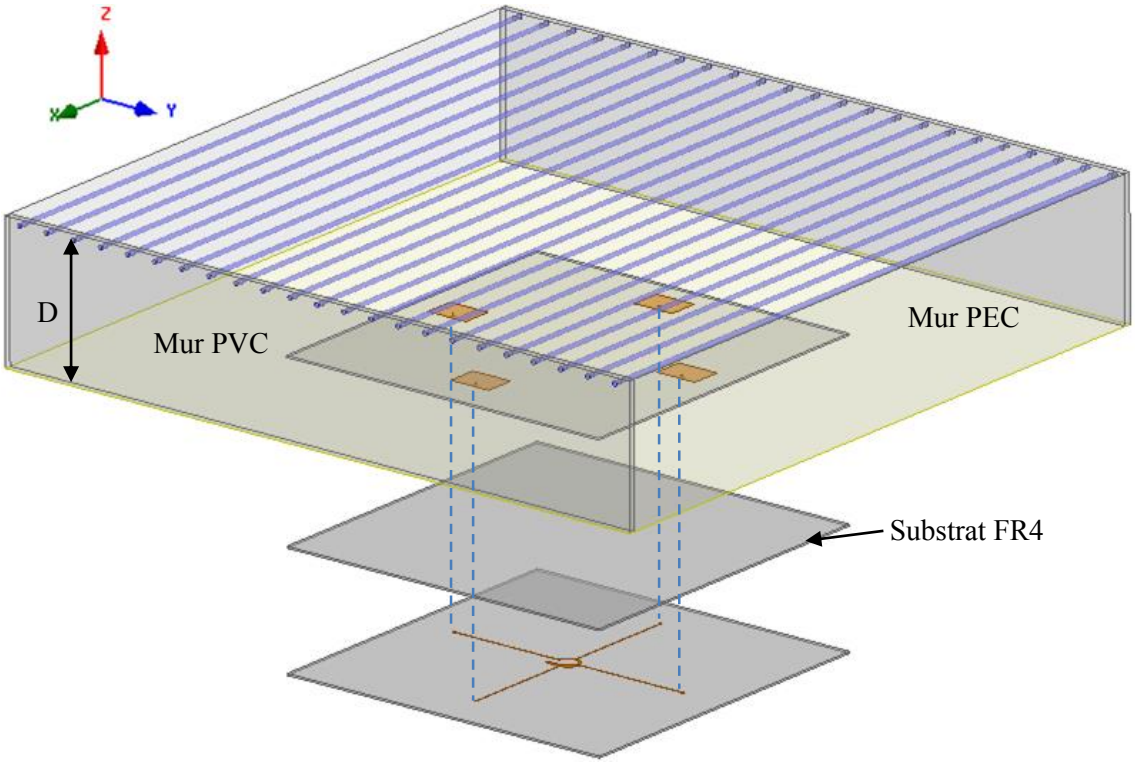

Fig. 12: Géométrie de l'antenne à cavité FP avec le réseau de patch à onde OAM son déphaseur

Les cartographies 2D en amplitude et en phase du composant E_x (Fig. 1b) de l'onde propagée, observées dans un plan parallèle à la cavité et à 30 mm au-dessus du PRS, sont présentées à la Fig. 13. La fenêtre d'observation est une zone circulaire de rayon de 300 mm. On peut noter la présence des propriétés caractéristiques d'une onde porteuse d'un OAM de $\ell = 1$, à savoir : une amplitude minimale au centre et une variation régulière de la phase autour du centre avec un déphasage de 2π en un tour.

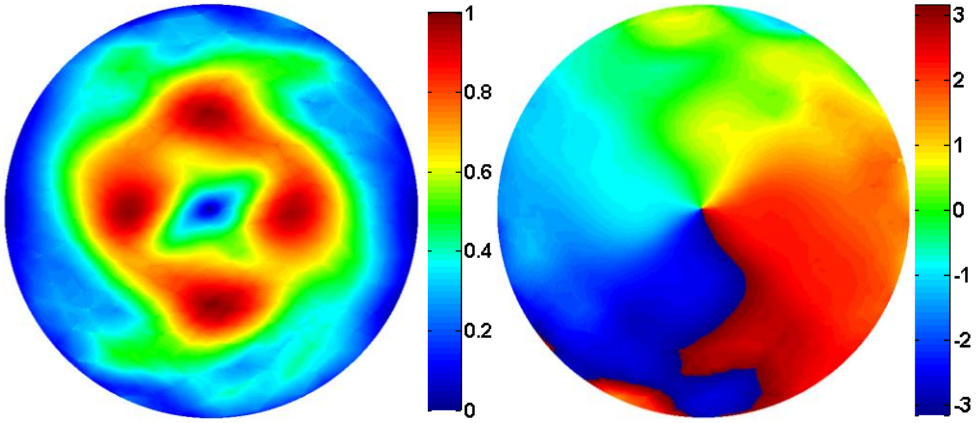

Fig. 13: Cartographie 2D en amplitude (à gauche) et en phase (à droit) du composant E_x pour l'antenne à cavité FP à 2.5 GHz

IV. Génération d'onde guidée à OAM dans guide circulaire

La lame de phase spiral (SPP – Spiral Phase Plate) a été proposée pour transformer une onde plane en une onde transportant du moment angulaire orbital [22-24]. Elle a été utilisée en optique et en radiofréquence pour générer des ondes à OAM dans l'espace libre, mais très rarement dans un guide d'onde, sauf dans [69]. Nous présentons dans ce chapitre, deux antennes cornets coniques générant des faisceaux directifs à OAM. Ces cornets sont excités par des guides d'ondes circulaires, où les modes guidés classiques sont transformés en mode OAM grâce aux lames SPP. Le premier cornet est basé sur le mode TE_{11} (Transverse Electric), et le second sur le mode TM_{01} (Transverse Magnetic).

1. Mode TE_{11} et une seule SPP

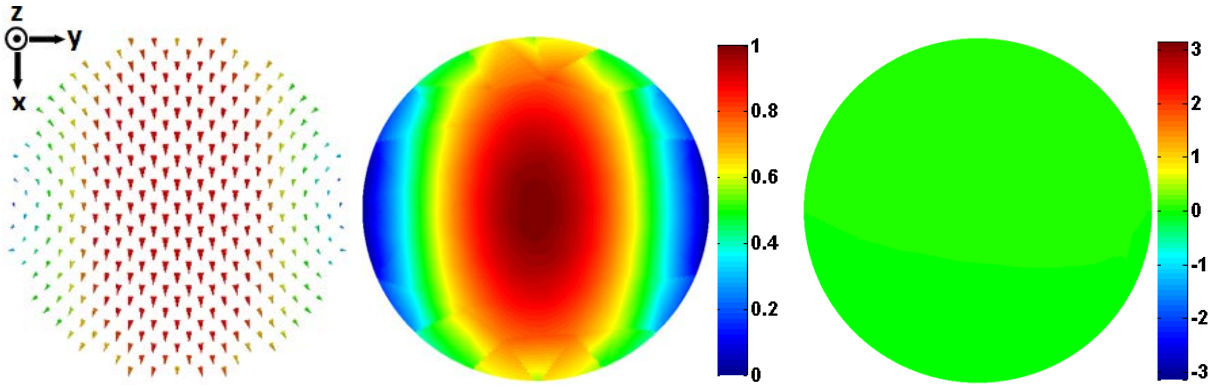

(a) (b) (c)

Fig. 14: Mode TE_{11} circulaire classique. (a) Distribution du champ électrique; (b) Amplitude normalisée de la composante E_x ; (c) Phase de la composante E_x

La distribution du champ électrique pour le mode TE_{11} classique dans un guide circulaire, ainsi que la répartition de l'amplitude et la phase de sa composante E_x sont rappelées sur la Fig. 14. On remarque que l'amplitude du champ électrique est très forte au centre, alors qu'elle devrait être nulle ou très faible pour l'onde OAM en raison du vortex ou de la singularité champ créé par la variation linéaire de la phase sur le front d'onde. Par conséquent, il est très difficile de générer des ondes OAM à l'intérieur du guide d'onde à partir du mode TE_{11}. Les simulations montrent que, lorsque la SPP est placée à l'intérieur du guide d'onde, il faut augmenter la fréquence de travail jusqu'à 10 fois la fréquence de coupure du mode TE_{11}, pour que l'onde à OAM (avec un creux au centre) puisse s'installer. A cette fréquence élevée les modes guidés d'ordre supérieur se génèrent abondamment et rendent difficile l'obtention d'un mode TE_{11} pur. Pour contourner ce problème, nous proposons une conception pratique qui consiste à placer la SPP à l'intérieur du cornet au lieu de l'intérieur du guide d'onde, comme le montre la Fig. 15.

De cette manière, la fréquence de travail peut être réduite et être assez proche de la fréquence coupure du mode TE_{11}.

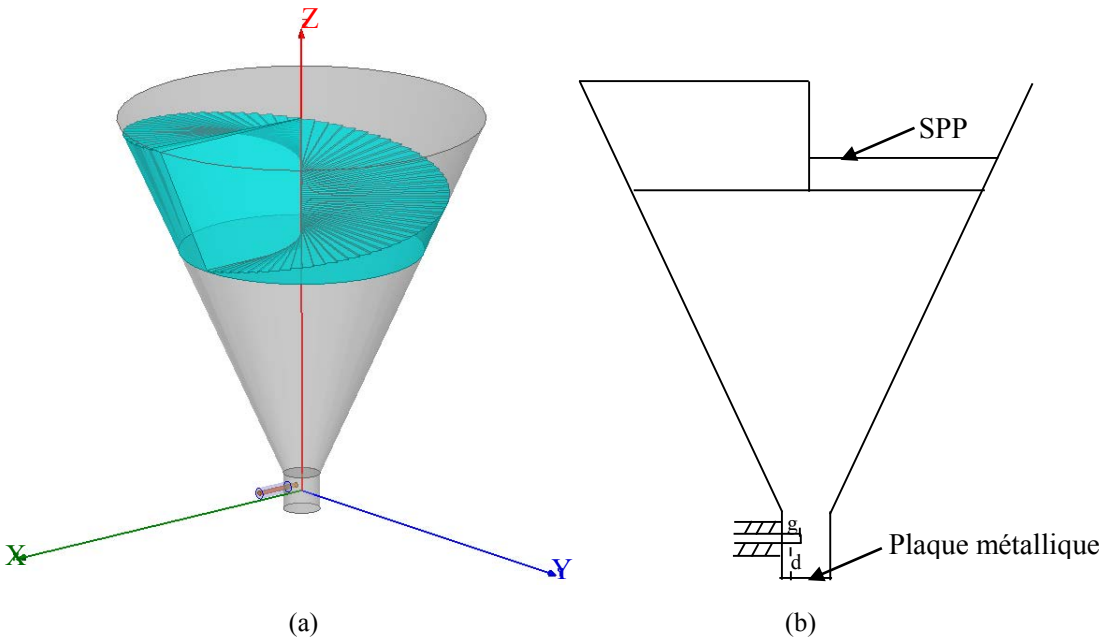

Fig. 15: Géométrie de l'antenne cornet OAM avec un SPP unique (SPP dans la corne): (a) vue 3D de la structure d'antenne; (b) vue 2D pour montrer les paramètres de la sonde

Dans cette conception, le guide d'onde vide possède un diamètre de 1 cm et la fréquence de coupure correspondante du mode TE_{11} est de 17.6 GHz. L'ouverture du cornet a un diamètre de 10 cm. Les hauteurs du guide d'onde et du cornet sont respectivement de 1 et de 10 cm. Nous avons choisi une fréquence de travail de 20 GHz pour être sûr que la longueur d'onde est suffisamment faible par rapport à l'ouverture du cornet. Le mode TE_{11} est créé par une sonde qui est placée perpendiculairement à la paroi métallique du guide circulaire et à une distance d = 0.7 cm au-dessus de la plaque métallique (voir Fig. 15b). La longueur g de la sonde est optimisée à 0.3 cm pour réaliser une bonne adaptation d'impédance à 50Ω. La hauteur de la SPP est optimisée à 3.7 cm pour générer une onde OAM avec $\ell = 1$.

La Fig. 16 montre le diagramme de rayonnement 3D du cornet à 20 GHz. Le diagramme montre bien rayonnement nul au centre qui est la signature des ondes à OAM. Les diagrammes en amplitude et en phase de l'onde propagée, observé dans un plan perpendiculaire à la direction de propagation, sont représentés à la Fig. 17. La zone d'observation a un rayon de 5 cm, et est située à 2 cm au-dessus de l'ouverture du cornet. On peut constater que l'amplitude est minimale au niveau du centre et la phase tourne autour de ce centre avec un déphasage de 2π sur un tour. Cela confirme la génération d'une onde ayant un OAM de $\ell = 1$. Nous pouvons observer que la qualité de l'amplitude du champ E_x n'est pas très satisfaisante, car les lobes secondaires sont

nombreux et ont un niveau relativement élevé. Pour améliorer cette situation, dans le paragraphe suivant, nous développons une autre antenne cornet basé sur le mode TM_{01}.

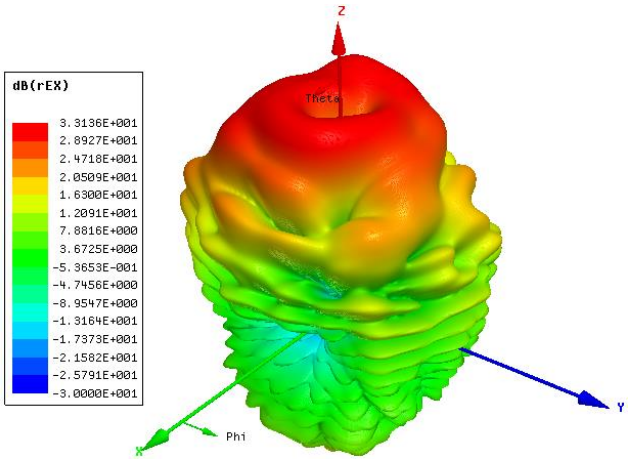

Fig. 16: Diagramme de rayonnement 3D de l'antenne cornet OAM à la fréquence de 20 GHz avec un seul SPP placé à l'intérieur du cornet

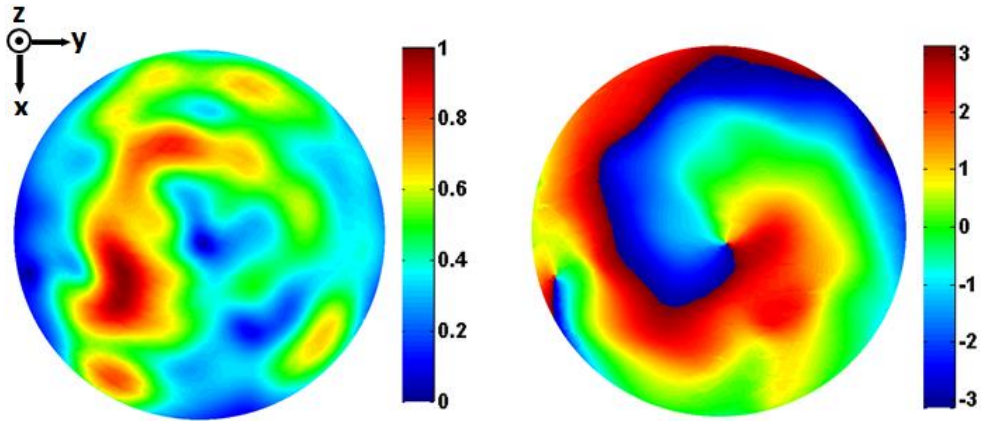

Fig. 17: Les diagrammes en magnitude normalisée (à gauche) et en phase (à droite) du composant E_x pour l'antenne cornet OAM avec un SPP unique à la fréquence de 20 GHz

2. Mode TM_{01} et deux demi-SPPs

La Fig. 18 rappelle la distribution du champ électrique, ainsi que celle de l'amplitude et de la phase de la composante E_x, pour le mode TM_{01}. L'amplitude du champ électrique est minimum au centre et à cet égard; il satisfait une des conditions nécessaire pour l'existence de l'onde OAM dans le guide d'onde. D'après la Fig. 18c, la phase de la composante E_x de ce mode classique est constante par demi-cercle et subit un saut de π d'un demi-cercle à l'autre. Ainsi, pour créer le mode OAM $\ell = 1$, nous avons conçu deux SPPs. Chaque SPP ne devra réaliser qu'un décalage de phase de π ce qui réduit la hauteur des SPP de moitié. De cette façon, le déphasage total en un tour répondra à l'exigence de 2π.

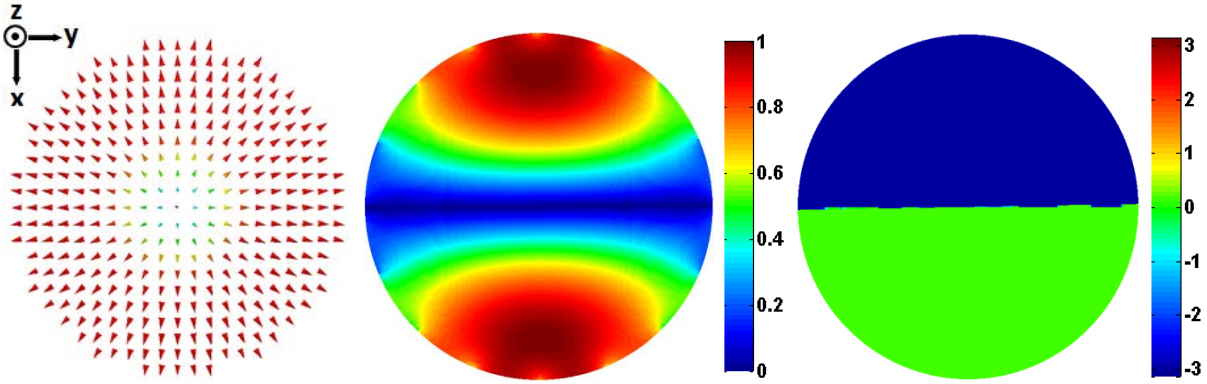

(a) (b) (c)

Fig. 18: Mode guidé classique TM_{01} dans un guide d'onde circulaire : (a) Distribution de champ électrique; (b) Amplitude normalisée de la composante E_x; (c) Phase de la composante E_x.

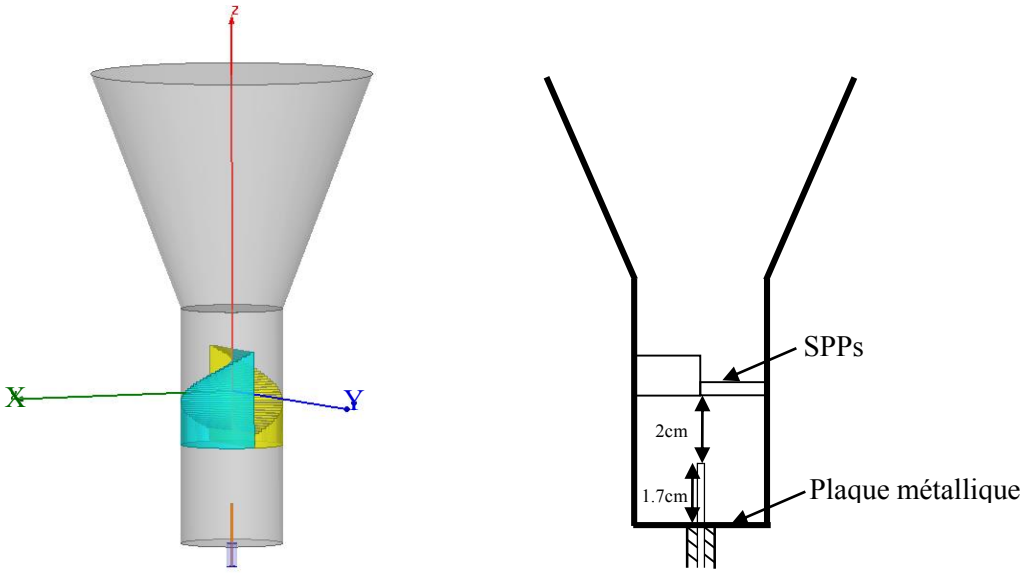

(a) (b)

Fig. 19: Géométrie de l'antenne cornet OAM avec deux demi SPPs:(a) vue 3D de la structure d'antenne; (b) vue 2D pour montrer les paramètres de la sonde

La géométrie de l'antenne à cornet conique à onde OAM, basée sur le mode TM_{01}, est montrée à la Fig. 19. Les diamètres du guide d'onde et l'ouverture de cornet sont respectivement de 4.4 et 12 cm, et les hauteurs sont toutes deux de 10 cm. La fréquence de coupure du mode TM_{01} est de 5.2 GHz. Pour la fréquence de travail nous choisissons 7.4 GHz. Les deux demi-SPPs sont placées à l'intérieur du guide d'onde. Elles sont réalisées en téflon et ont une hauteur de 3.6 cm. Une ligne coaxiale excite la sonde monopolaire placée au fond du guide d'onde et au milieu de la plaque métallique comme le montre la Fig. 19. Les SPPs sont placées à 2 cm au-dessus de la sonde. Pour satisfaire l'adaptation d'impédance, la longueur de la sonde est optimisée à 1.7 cm.

Le diagramme de rayonnement 3D à 7.4 GHz est présenté à la Fig. 20. Nous pouvons constater la présence du vortex central. Comparé à l'antenne précédente, le diagramme de rayonnement est de meilleure qualité car il possède moins de lobes secondaires et est plus symétrique. Sur la Fig. 21 sont tracées les cartographies en amplitude et en phase du champ électrique, dans un plan situé à 1 cm au-dessus de l'ouverture du cornet. Nous pouvons observer que l'amplitude au centre est beaucoup plus faible qu'ailleurs et la phase a une variation de 2π sur un tour. Ceci démontre la prédominance du mode OAM avec $\ell = 1$. De plus, par rapport à l'antenne cornet précédente, le diagramme du champ E_x est mieux formé.

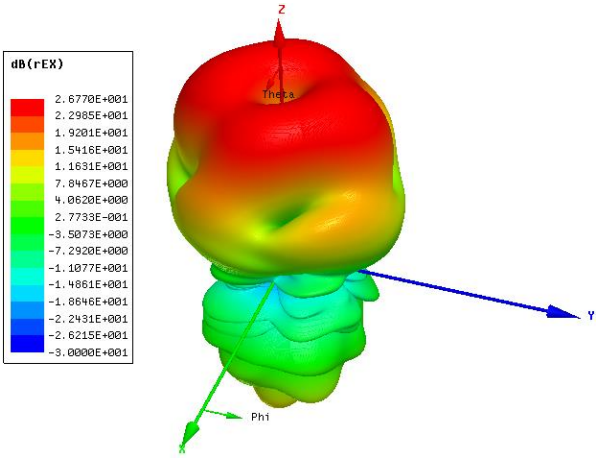

Fig. 20 : Diagramme de rayonnement 3D de l'antenne cornet OAM avec deux demi-SPPs à la fréquence de 7.4 GHz

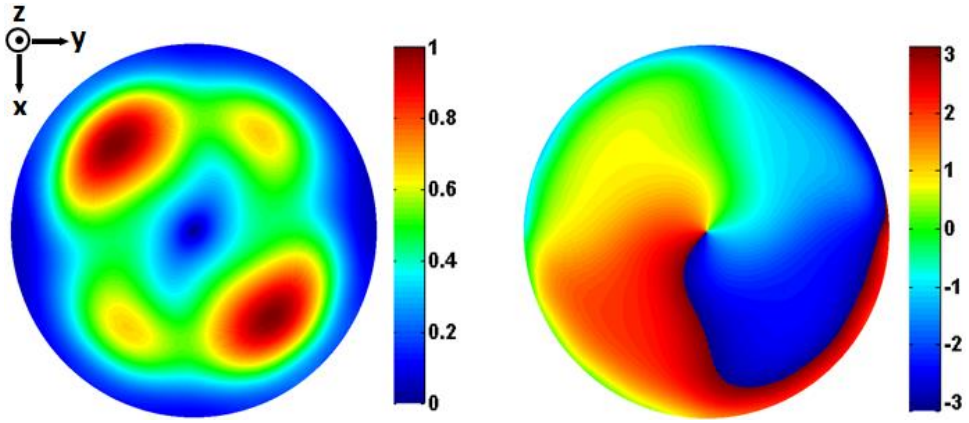

Fig. 21: Cartographie en amplitude normalisée (à gauche) et en phase (à droite) de la composante E_x du champ électrique à la fréquence de 7.4 GHz et à 1cm de l'ouverture du cornet excitée par deux demi-SPPs

V. Génération d'OAM dans un guide d'onde circulaire en combinant des modes guidés

Il a été démontré en optique que les modes de Laguerre-Gauss (LG) peuvent être produits en combinant deux modes Hermite-Gauss (HG). Suivant cette idée, un guide d'onde rectangulaire en silicium a été utilisé pour générer des faisceaux OAM optiques en combinant les modes E^x_{21} et E^x_{12} [70].

De la même manière, en combinant certains modes propres d'un guide d'onde métallique, on peut créer des ondes OAM dans les bandes de fréquences radio. Dans cette partie, nous proposons deux méthodes pour obtenir le mode OAM $\ell = 1$: i) la combinaison de deux types de modes TE_{21}; ii) la combinaison des modes TM_{01} et TE_{21}.

1. Combinaison de deux types de modes TE_{21}

La Fig. 22 montre la distribution du champ électrique, ainsi que celle de l'amplitude et de la phase de la composante E_x du premier type de mode TE_{21} et la Fig. 23, celles du deuxième type de mode TE_{21}. On peut voir que les diagrammes du champ E des deux types de mode TE_{21} sont assez similaires. La différence est une rotation de $\pi/2$ entre les deux diagrammes aussi bien en champ qu'en amplitude et en phase. Il en va de même pour la composante E_y.

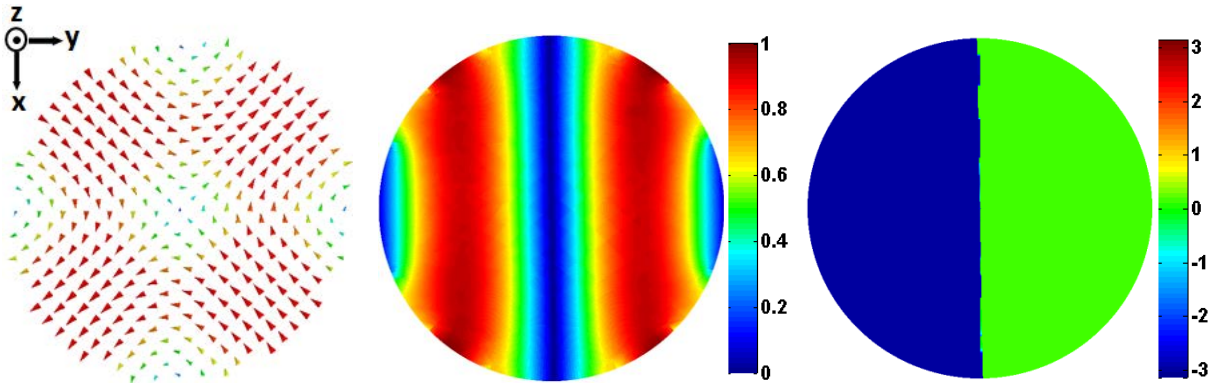

(a) (b) (c)

Fig. 22: Mode guidé classique TE_{21} (premier type) le guide d'onde circulaire : (a) Distribution de champ électrique; (b) Amplitude normalisée de la composante E_x; (c) Phase de la composante E_x

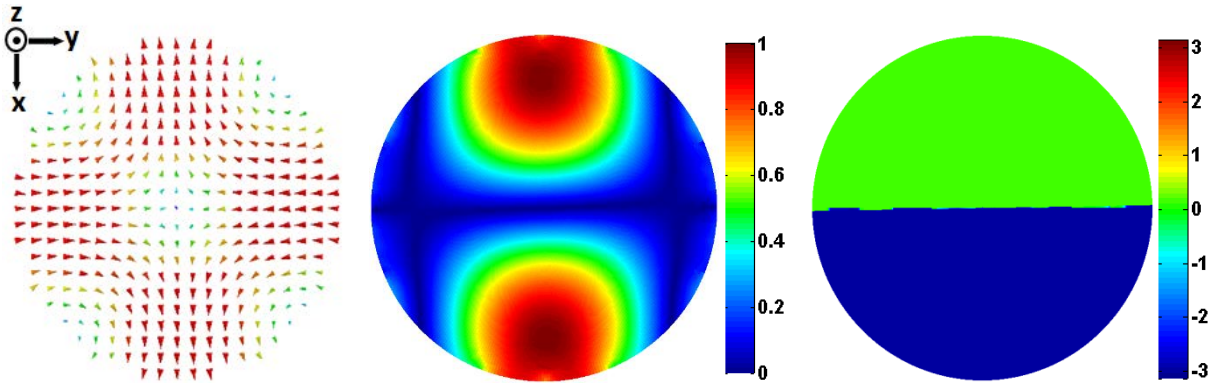

(a) (b) (c)

Fig. 23: Mode guidé classique TE_{21} (deuxième type) le guide d'onde circulaire : (a) Distribution de champ électrique; (b) Amplitude normalisée de la composante E_x; (c) Phase de la composante E_x

En excitant simultanément les deux types de mode TE_{21} avec une différence de phase de $\pi/2$, on obtient une onde guidée à comportement « OAM » comme le montrent les figures 24 (pour E_x) et 25 (pour E_y). On peut voir que la distribution de l'amplitude est relativement uniforme et présente bien un minimum prononcé au centre. La phase à son tour fait une variation de 2π sur un tour. Cela montre en effet pour chaque composante du champ E, un mode OAM ℓ égal à 1.

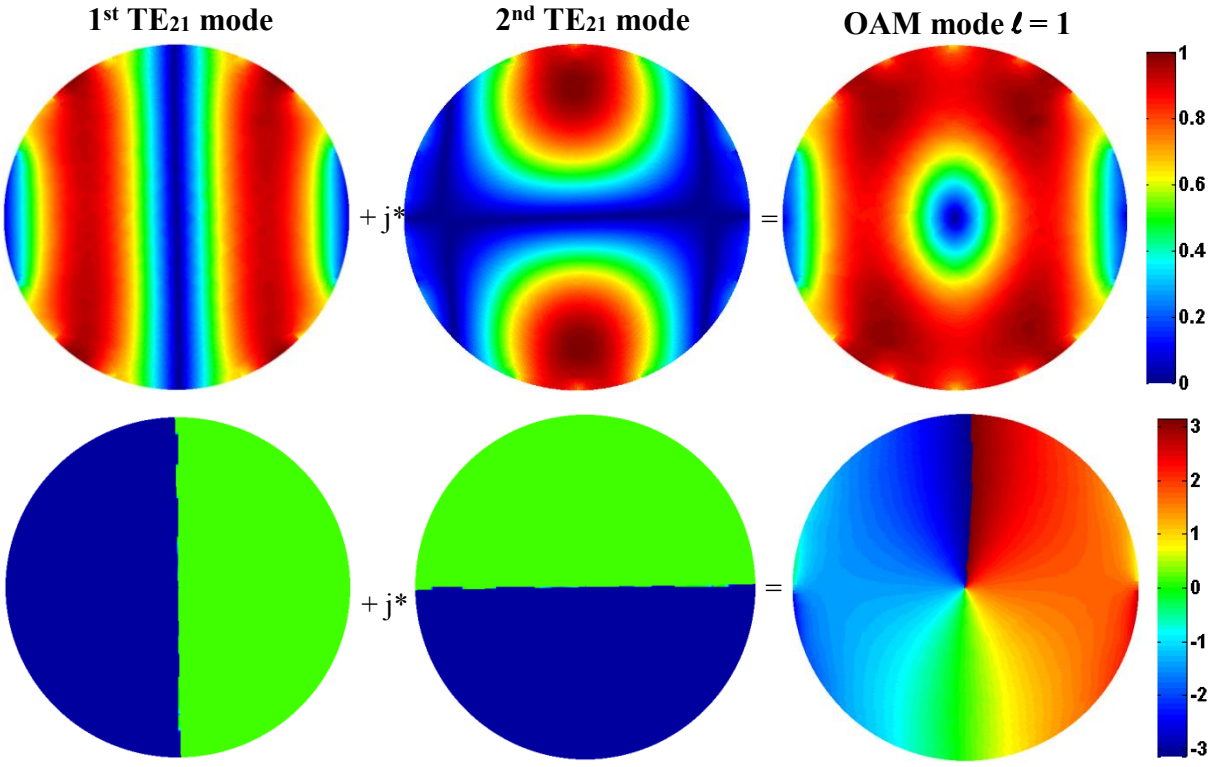

Fig. 24: Evolutions des diagrammes en amplitude (en haut) et en phase (en bas) de la composante E_x pour la génération d'une onde OAM, en combinant deux types de mode de TE_{21} avec une différence de phase de $\pi/2$ entre les deux

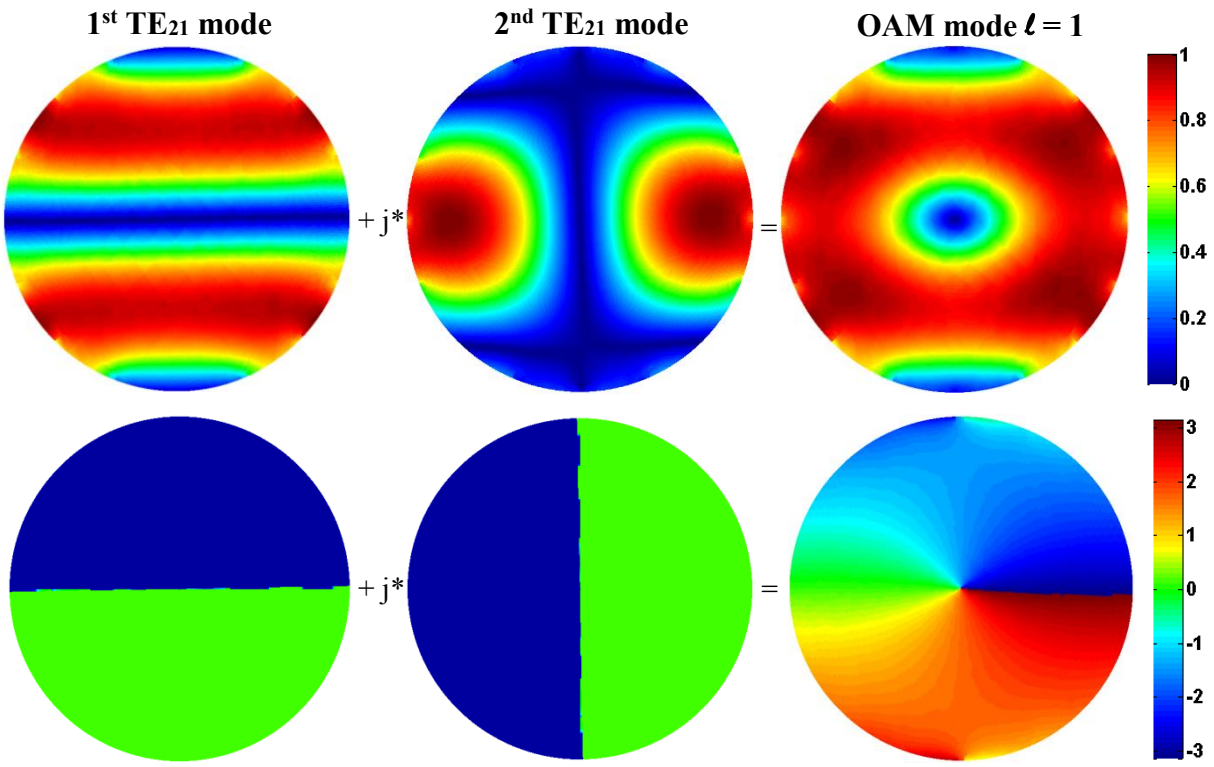

Fig. 25: Evolutions des diagrammes en amplitude (en haut) et en phase (en bas) de la composante E_y pour la génération d'une onde OAM, en combinant deux types de mode de TE_{21} avec une différence de phase de $\pi/2$ entre les deux

Cependant, il est difficile d'obtenir le mode TE_{21} pur en pratique. Dans le paragraphe suivant, nous présentons une autre méthode en combinant les modes TM_{01} et TE_{21}.

2. Combinaison de modes TM_{01} et TE_{21}

De la même manière que précédemment, on peut créer une onde OAM en combinant le mode TM_{01} et le premier type de mode TE_{21} avec une différence de phase de $\pi/2$ en entre les deux.

Pour réaliser cette antenne, nous introduisons deux monopôles imprimés à l'intérieur d'un guide d'onde circulaire métallique pour créer simultanément les modes TM_{01} et TE_{21}. La distribution du champ électrique, de son amplitude et de sa phase pour les modes TM_{01} et le premier type de mode TE_{21} ont été fournis précédemment dans les figures 18 et 22 respectivement et sont rappelée à la Fig. 26 pour simplifier la compréhension de la conception de l'antenne. Nous pouvons constater que pour créer ces deux modes simultanément, on peut placer deux sondes d'excitation sur la même ligne et en opposition de phase. A cet effet, nous avons créé deux petites antennes (sondes) monopolaires reliées à une ligne de transmission, elle-même connectée au l'âme centrale d'un câble coaxial de 50 Ω comme le montre la Fig. 27.

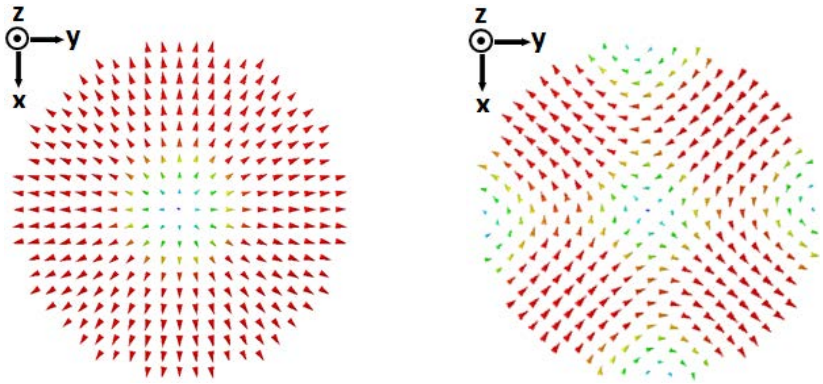

(a) (b)

Fig. 26 : Distributions du champ électrique pour les modes TM_{01} et TE_{21} : (a) TM_{01} (b) TE_{21} de type 1

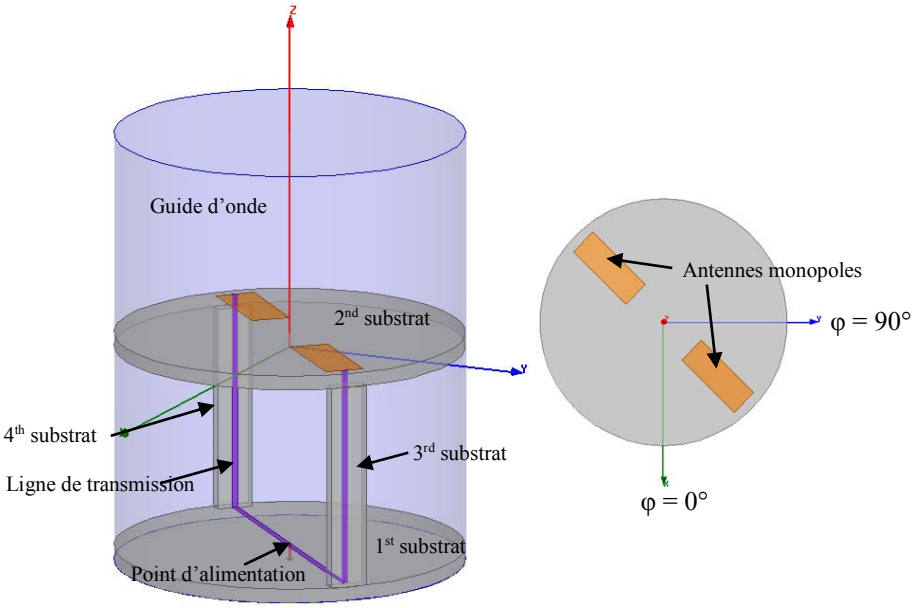

Fig. 27: Géométrie de l'antenne OAM réalisée pour la combinaison des modes TE_{21} et TM_{01}

Etant donné que l'intensité du champ du mode TE_{21} est maximale à $\varphi = \pm 45°$ et $\pm 135°$, les antennes monopôles doivent également être placés dans ces positions angulaires. Dans notre conception, nous plaçons les monopôles à $\varphi = 45°$ et -135°.

Les monopôles et leur lignes d'alimentation sont fabriqués en cuivre sur du substrat FR4 ayant une épaisseur de 1.6 mm et une permittivité relative de 4.4. Le circuit d'excitation comprend 4 parties. La première est un disque placé au fond du guide d'onde et est de même diamètre que celui-ci. La deuxième est également un disque qui supporte les monopoles et est situé à mi-hauteur du guide d'onde. Les 3ème et 4ème parties constituent les lignes de transmission et sont placés le long de la paroi latérale du guide et sont utilisés pour connecter les 1er et 2ème disques entre eux. Les lignes de transmission ont une largeur de 0.7 mm et une impédance de

100 Ω. Pour satisfaire l'adaptation d'impédance à la fréquence de travail, la longueur et la largeur de chaque antenne monopôle sont respectivement optimisées à 12 et 4.5 mm.

Le guide d'onde est vide et a un diamètre de 4 cm et une hauteur de 5 cm. Les fréquences de coupure des modes TE_{21} et TM_{01} sont respectivement de 5.7 et 7.3 GHz. Nous choisissons une fréquence de travail de 8.3 GHz pour permettre la propagation des deux modes tout en empêchant les modes d'ordre supérieur.

Les cartographies en amplitude et en phase de l'onde propagée, observées dans un plan perpendiculaire à la direction de propagation et se trouvant 1 cm au-dessus de l'ouverture du guide d'onde, sont présentés à la Fig. 28. . On peut constater que, les deux composants Ex et Ey satisfont les conditions du mode OAM $\ell = 1$ (amplitude faible au centre et déphasage de 2π sur un tour).

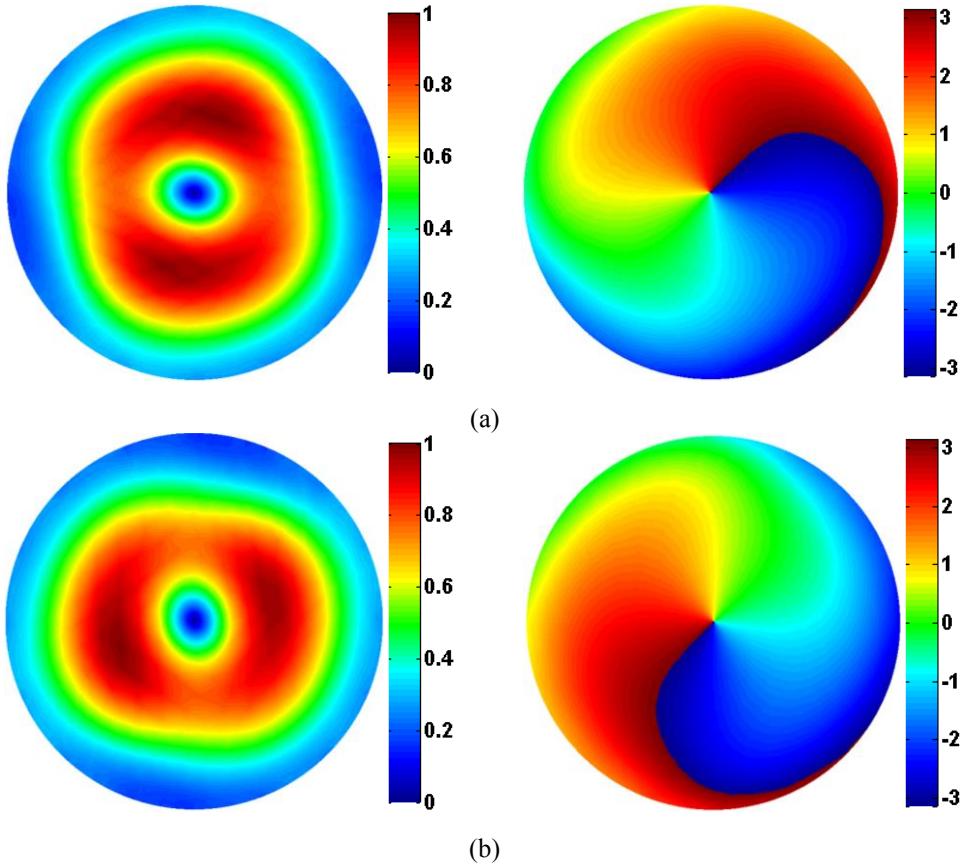

Fig. 28: Diagrammes en amplitude (à gauche) et en phase (à droite) de l'onde propagée: (a) Composante E_x; (b) Composante E_y

La Fig. 29 montre les diagrammes de rayonnement et de phase en 3D de l'antenne OAM. Pour chaque composante, les diagrammes ont l'aspect d'un tourbillon qui est caractéristique

d'une onde OAM. La forme en « escargot » de la phase, tracée en coordonnées polaires, correspond à la variation de la phase avec l'angle de roulis ($\alpha = \ell\varphi$).

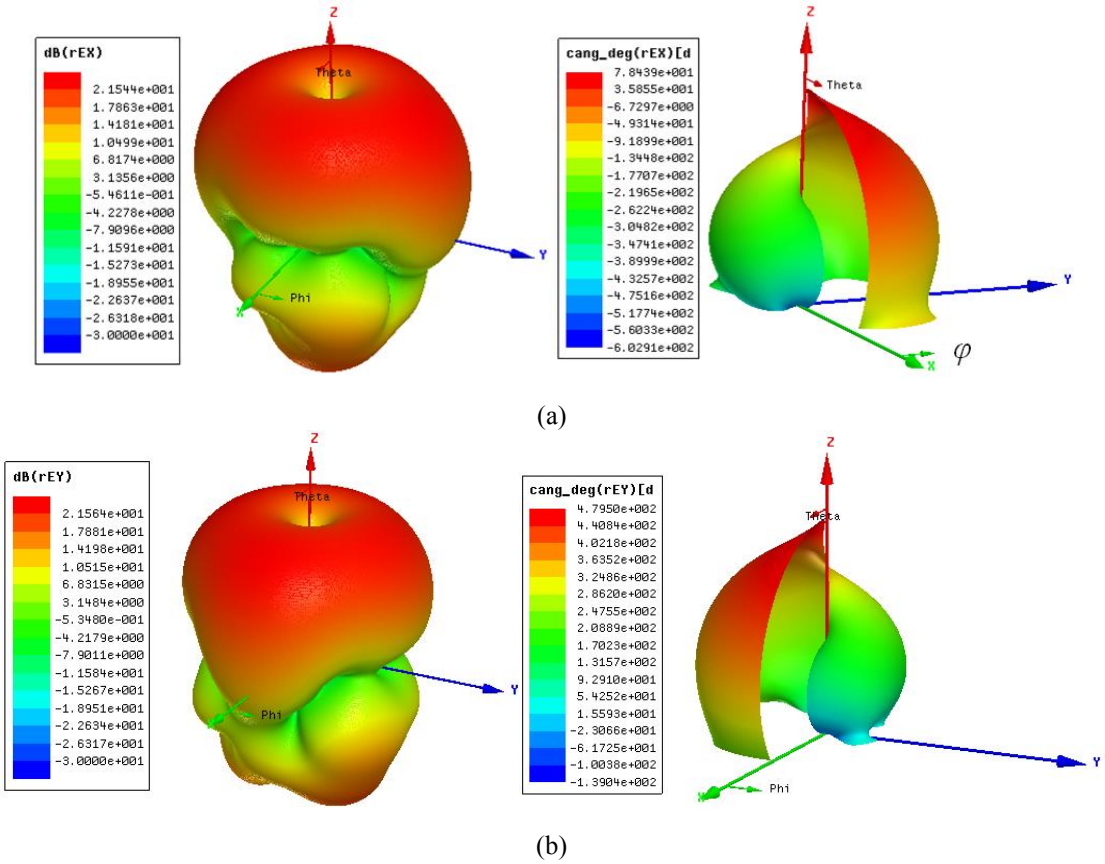

Fig. 29 : Diagrammes de rayonnement (à gauche) et de phase (à droite) 3D de l'antenne OAM à 8.3 GHz : (a) Composant E_x; (b) Composante E_y

VI. Conclusions et perspectives

Dans cette thèse, nous avons proposé plusieurs nouvelles antennes afin de générer des ondes ayant de l'OAM en radiofréquence. La première antenne est basée sur un déphaseur circulaire et un réseau de 4 patchs, et peut générer une onde OAM $\ell = 1$.

Pour améliorer la directivité de cette antenne OAM, nous l'avons insérée à l'intérieur d'une cavité Fabry-Perot. Les résultats de simulation montrent que la directivité de l'antenne passe de 7 dB à 16.6 dB.

Enfin, nous avons proposé plusieurs antennes à cornet, ainsi qu'une antenne à guide d'onde pour obtenir des directivités moyennes.

Dans le prolongement de cette thèse, les perspectives suivantes sont envisagées:

- Réaliser les antennes cornets et l'antenne en guide d'onde pour valider les résultats de la simulation.
- Placer ces cornets sur le foyer d'un réflecteur parabolique classique pour obtenir des directivités élevées à un coût faible.
- Utiliser le cornet OAM comme une «source primaire» pour les réflecteurs paraboliques torsadés (à OAM) pour produire avec un ordre OAM plus élevé tout en conservant une directivité élevée.
- Appliquer les antennes OAM proposées dans les communications sans fil et les radars.

Contribution to the Study and Design of Antennas for the Generation of Radio Waves Bearing Orbital Angular Momentum

General Introduction

Context and objectives of the study

It is well known from Maxwell's theory that electromagnetic (EM) radiation carries both linear momentum (energy) and angular momentum. The latter has two parts: Spin Angular Momentum (SAM) which corresponds to the polarization of an EM wave and Orbital Angular Momentum (OAM) which is associated with the spatial distribution of an EM wave.

The SAM of an EM wave carries $\pm\hbar$ per photon and it has been recognized for a long time. However, the OAM has not attracted the attention of the researchers until 1992 when Allen *et al.* [1] recognized that some types of beams possess an orbital angular momentum of $\ell\hbar$ per photon, where ℓ is an integer called the "topological charge" or the order of the OAM mode. Whereas the phase of a usual plane wave is constant on the wavefront, the phase α of OAM waves undergoes a linear variation along the angular coordinate φ (roll angle): $\alpha = \ell\varphi$. The field hence varies as $e^{-j\ell\varphi}.f_\ell(r).e^{-jkz}$, where k is the wave vector, z is the propagation axis and $f_\ell(r)$ represents the field variation along the radial coordinate.

The special characteristics of OAM have attracted a great deal of interests from many domains. The early studies concerning the interaction of OAM with matter evoked the applications of optical tweezers [2], optical drive of micro-machines [3], atoms trapping and guiding [4]. In radio domain, OAM has been firstly proposed to improve spectral efficiency [5-9] in radio communications, by creating multiple sub-channels of propagation corresponding to the twisting degree of the EM wave. Despite this point is still subject to intense debates [6, 10-13], there are also possible applications of OAM for object identification [14] and radars [15-17].

The OAM beams can be generated easily in optical domain, especially when the programmable spatial light modulator (SLM) is available [18]. The existing optical devices can also provide mature schemes to manipulate the OAM beams such as combining, splitting, collimation, concentrating, and detecting [19-22]. Hence, the optical OAM beams can be deftly applied to many fields. However, when it comes to the radio domain, as the wavelength is much longer than the optics, it is difficult to manipulate the radio OAM beams, such as beam combining and splitting, so that the coaxially transmitting cannot be easily ensured. Therefore, among the applications of OAM at radio frequencies, the generation of OAM is very important and sometimes decides the performance of the whole system.

Up to now, in the radio domain, two main families of antennas have been proposed to generate OAM waves. In the first one, the OAM wave is generated by a transformation of a plane wave. This can be achieved by using the spiral phase plate [23], flat drilled phase plate [23-25] and spiral reflectors [6, 26]. In the second family, the OAM wave is directly generated using some circular phased arrays [5, 27-30].

The main objective of this thesis is to design several new antennas for the generation of radio OAM waves, which is necessary for any existing and future application.

Outline of the thesis

This thesis consists of 4 major chapters:

In the first chapter we introduce the properties of EM waves bearing OAM and review the typical methods for generating these waves in both optical and radio domains.

In the second chapter an OAM antenna using 4 patches and an original circular phase shifter-power divider is developed. This antenna works at 2.5 GHz and generates an OAM wave with $\ell = 1$. This chapter consists of two major parts. The first part is the parametric study of an ideal phased patch array, which is necessary for the design of a practical OAM antenna; the second part presents the design procedure, the simulation data and the measurements of this novel OAM antenna.

In the third chapter we present a method to enhance the directivity of the previously developed OAM antenna by using the Fabry-Perot (FP) cavity. A FP cavity is generally composed of a ground plane, an air cavity and a partially reflecting surface (PRS). It is highly frequency selective and is often used to improve the antenna directivity in antenna applications. We embed the previous OAM antenna inside the FP cavity with two different PRS. The first one is made of periodic metallic strips printed on a FR4 substrate, and the second, made of periodic metallic tubes. Each FP cavity is optimized associated with the phased patch array to obtain a maximum antenna directivity. The design procedure and the simulation data of the two FP OAM antennas are given, as well as the measurements of the second antenna.

In the fourth and last chapter, we present some horn antennas and a waveguide antenna for the generation of radio OAM waves. These structures are all based on a circular metallic waveguide. Actually, we have developed two major methods to obtain the OAM mode: i) transformation of the guided modes of a circular waveguide by using the spiral phase plate; ii) combination of the guided modes. The field distributions and the corresponding field patterns (magnitude and phase) of the utilized guided modes are given and analyzed. Besides, both the

ideal model and the practical design of the proposed antennas are presented and characterized based on simulations.

Table of Contents

Chapter I

Orbital Angular Momentum of Electromagnetic Waves

I.1 What is the Orbital Angular Momentum?

It is well known from Maxwell's theory that electromagnetic (EM) radiation carries both energy and momentum. The momentum may have two parts of contributions: linear momentum and angular momentum [1]; the latter can be decomposed into two distinct components: spin and orbital. The spin angular momentum (SAM) corresponds to the polarization of an EM wave and the orbital angular momentum (OAM) is associated with the spatial distribution of an EM wave.

Since the concept of momentum is not specific to the EM waves, it is also related to the classical mechanics, we will firstly give a brief presentation of this concept in this area before turning to the EM waves. Thereafter, a vector is represented by a bold letter (e.g. $\boldsymbol{E}$ represents the electric field vector).

I.1.1 Momentum in classical mechanics

The second law of Newton which was published in 1687 states that for a body with a constant mass *m*, the acceleration suffered by the body is proportional to the net force applied and inversely proportional to its mass *m*. A more general form is to say that the force is equal to the change of momentum per unit time:

$$\boldsymbol{F} = \frac{d\boldsymbol{p}}{dt} \tag{I-1}$$

where $\boldsymbol{F}$ is the force applied on the object, and $\boldsymbol{p} = m\boldsymbol{v}$ is the momentum equal to the product of its mass *m* and its speed $\boldsymbol{v}$.

The angular momentum of a point *M* is the moment of the momentum $\boldsymbol{p}$ with respect to an original point *O* ($\overrightarrow{OM} \times \boldsymbol{p}$). Therefore it plays a role similar to the linear momentum, but in the case of rotation. We will find again these two conceptions concerning the EM waves.

I.1.2 Momentum of electromagnetic waves

I.1.2.1 Linear momentum: Poynting vector

The Poynting vector is a vector whose direction indicates the direction of propagation of an EM wave in the absence of angular momentum, and whose intensity is equal to the wave power density. It is expressed in W/m² and is defined by:

$$\boldsymbol{S} = \boldsymbol{E} \times \boldsymbol{H} \tag{I-2}$$

where $\boldsymbol{E}$ and $\boldsymbol{H}$ represent respectively the electric and magnetic fields.

The momentum $\boldsymbol{p}$ of a photon is then expressed as:

$$\boldsymbol{p} = \hbar k \tag{I-3}$$

where *k* represents the wave number and $\hbar$ the reduced Plank constant.

I.1.2.2 Angular momentum: SAM and OAM

In 1909, Poynting made the hypothesis that a circularly polarized EM wave carries angular momentum [31]. His reasoning is based on an analogy between a mechanical model – a uniformly revolving shaft of circular section, and a beam of circularly polarized light. He concluded that the angular momentum delivered to unit area per second is:

$$\frac{P\lambda}{2\pi}$$

where P is the radiation pressure exerted on a surface by a beam of wavelength λ. In current notation, this amounts to writing that the angular momentum is equal to $\sigma\hbar$, with $\sigma = \pm 1$ corresponding respectively to the left and right circular polarization.

This component of the angular momentum is called the spin angular momentum (SAM), because it is associated with the spin of the photon (see Figure I-1a) which can be visualized by rotating the photon itself around its axis. Consequently, it can exist two values of σ, of which each corresponds to one direction of rotation [32]. Since it is not necessary for the photon to have an external reference, the SAM is also called the intrinsic angular momentum.

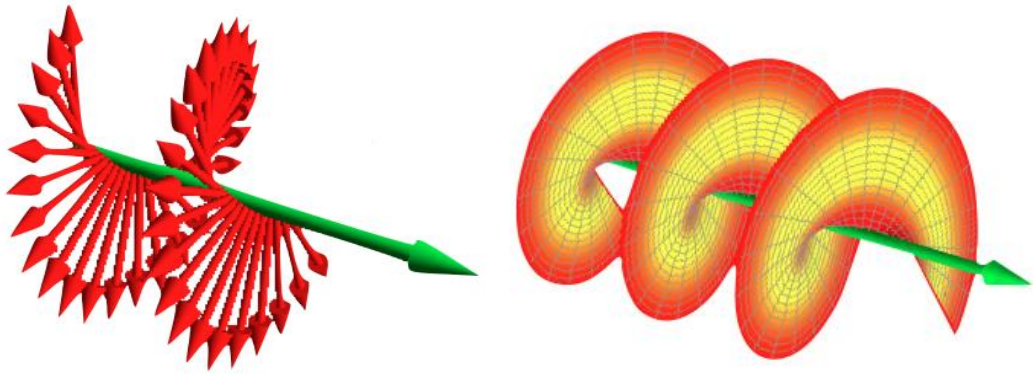

(a) (b)

Figure I–1: (a) The SAM of an EM wave; (b) the OAM of an EM wave [33]

There exists a second type of angular momentum which is defined in relation to an external reference: it is therefore an extrinsic angular momentum. It can be represented by an orbit of the photon around a point (see Figure I-1b) and that is why it is called the "orbital angular momentum (OAM)". We find the equivalence between the sign ("+" or "-") and the direction of rotation, but this time the value is related to the speed of rotation, i.e. the number of jump of 2π per period. Therefore, it can exist infinitely in theory.

In 1992, a team from the University of Leiden [1] studied again on this subject, especially on the transformation of orbital angular momentum through a Gaussian beam. In particular,

they were interested in the Laguerre-Gaussian (LG) modes which are defined by the polynomials of the same name and possess a varying term of exp(-i$\ell\varphi$) in their expression. Here ℓ is an integer number called the "topological charge" or the order of the OAM mode and φ is the roll angle.

In this case, ℓ is directly involved in the expression of the OAM carried by the beam: more exactly, the latter would be of $\ell\hbar$ per photon to match with the $\sigma\hbar$ of the SAM and the $\hbar k$ of the momentum. The Poynting vectors associated with a linearly polarized LG beam are shown (in the near field and without taking into account the beam divergence) in Figure I-2, with ℓ being related to the number of spirals. We can see that the vectors are not in the beam axis, but turn around.

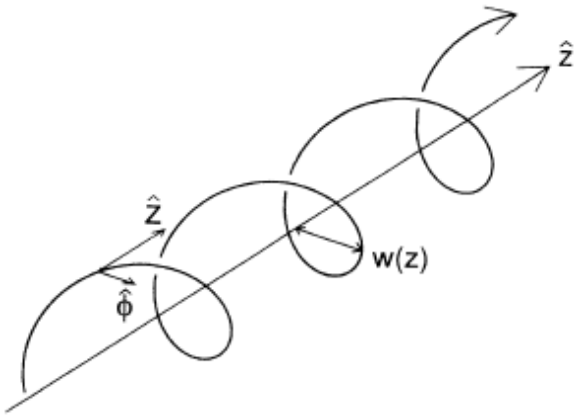

Figure I-2: The spiraling curve represents the Poynting vectors of a linearly polarized LG beam of radius w(z) [1]

Several years later, this phenomenon is observed experimentally by the measurements of the distributions of the intensity and phase [34]. An EM wave carrying OAM can be decomposed into (like any EM wave, within the scope of paraxial approximation) a sum of LG beams, noted LG_{pl} and given by [35-37]:

$$LG_{pl} = \sqrt{\frac{2p!}{\pi(p+|l|)!}}\frac{1}{w(z)}\left[\frac{r\sqrt{2}}{w(z)}\right]^{|l|} exp\left[\frac{-r^2}{w^2(z)}\right] L_p^{|l|}\left[\frac{2r^2}{w^2(z)}\right] exp(il\varphi)$$
$$exp\left[\frac{ik_0 r^2 z}{2(z^2+{z_R}^2)}\right] exp\left[-i(2p+|l|+1)\tan^{-1}\left(\frac{z}{z_R}\right)\right] \quad \text{(I-4)}$$

where the *1/e* radius of the Gaussian term is given by $w(z) = w(0)[(z^2 + {z_R}^2)/{z_R}^2]^{1/2}$ with w(0) being the beam waist, z_R the Rayleigh range, and $(2p + |l| + 1)\tan^{-1}(z/z_R)$ the Gouy phase. $L_p^{|l|}(x)$ is an associated Laguerre polynomial, obtained from the more familiar Laguerre polynomials by:

$$L_p^{|l|}(x) = (-1)^{|l|} \frac{d^{|l|}}{dx^{|l|}} L_{(p+|l|)}(x) \quad \text{(I-5)}$$

ℓ is the order of the OAM mode and p is the number of radial nodes in the intensity distribution. For the order $\ell = 0$, we find a Gaussian distribution. For any other value of ℓ, the intensity is distributed in the form of a ring (donut) centered on the beam axis. As an example, the intensity and phase plots of LG modes of LG_{01}, LG_{11} and LG_{21} are plotted in Figure I-3. It can be seen that in terms of its intensity on a plane perpendicular to the propagation axis, an LG mode comprises $p + 1$ concentric rings with a zero on-axis intensity. In addition, the phase distribution varies from 0 to 2π along the roll angle for each ring.

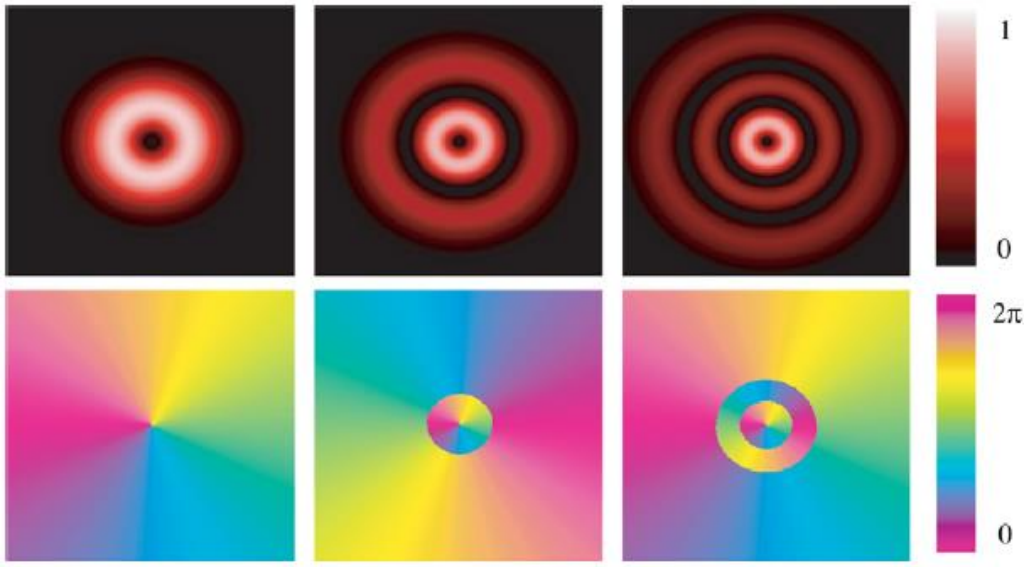

Figure I-3: Normalized intensity (top) and phase (bottom) plots of LG modes: LG_{0l}, LG_{11}, and LG_{21} (left to right) showing the p + 1 concentric rings and the effect on the phase pattern [38]

I.2 Methods for generating OAM waves at optical frequencies

According to the analysis in the previous section, one can know that the EM waves bearing OAM possess a helical phase front as $exp(-i\ell\varphi)$ (ℓ: the order of the OAM mode, φ: the roll angle), as shown in Figure I-4. Therefore, the key factor for generating OAM waves is to produce the helical phase front.

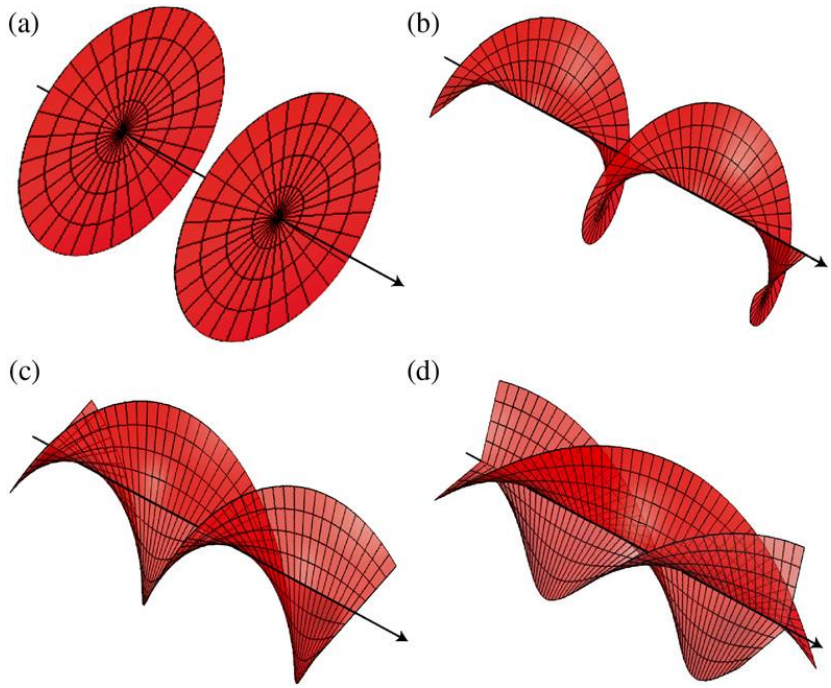

Figure I-4: Plane phase front for (a) $\ell = 0$ and helical phase fronts for (b) $\ell = 1$; (c) $\ell = 2$; (d) $\ell = 3$ [38]

Since Allen's experiment in 1992, many methods for generating OAM waves have been demonstrated. At different frequency bands, these methods can be different from each other. However, since OAM is a physical phenomenon throughout the EM spectrum, each frequency band can also take advantage of the benefits of other ones. In the following parts, we will introduce the methods which are often used at either optics or radio frequency bands.

Because the OAM was firstly studied in the optics field, we will at first introduce the techniques used in this field. In optics, two main families of tools are proposed for generating OAM beams: transformation optics that transforms the fundamental beam to an LG beam using "optics" and diffraction methods that use diffraction.

I.2.1 Spiral phase plate

A spiral phase plate (SPP) is a tool which enables the transformation of a plane wave carrying no orbital angular momentum to a wave bearing topological charge. It has been used in optics for many years [39-41], and can be realized by different techniques, such as vapor deposition [42], lithography [43], etc.

To better explain how the SPP works, let's firstly take a brief look at the concept of wave propagation. When a wave passes through a medium with a refractive index of n_1 and a height of L, its phase $\boldsymbol{\Phi}$ is increased by a quantity expressed by:

$$\Phi = \frac{2\pi}{\lambda} \times n_1 \times L \tag{I-6}$$

where λ is the wavelength.

However, the phase variation of an OAM wave on the wavefront is $2\pi\ell$ in one turn. To transform a plane wave or a wave with a plane wavefront, we can use a plate with a variable thickness. A spiral phase plate is made of the material with a constant refractive index and a varying thickness along the roll angle φ (see Figure I-5).

The phase shift $\delta\boldsymbol{\Phi}$ introduced by the SPP is then proportional to the roll angle and is expressed by:

$$\delta\Phi = \frac{2\pi\times(n_1-n_2)\times L_{max}}{\lambda} \quad \text{(I-7)}$$

where L_{max} corresponds to the height difference for $\varphi = 2\pi$ and n_2, the refractive index of air. Thus, to obtain a $2\pi\ell$ phase variation on the wavefront, the height difference should be equal to:

$$L_{max} = \frac{l\times\lambda}{n_1-n_2} \quad \text{(I-8)}$$

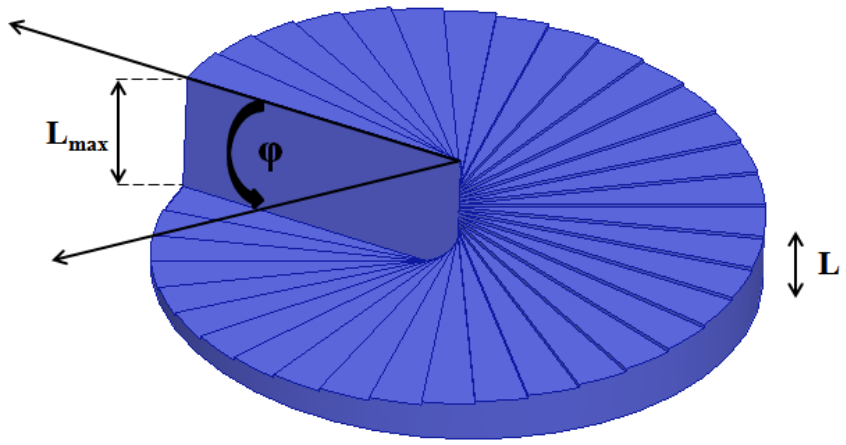

Figure I-5: Geometry of the spiral phase plate with a constant refractive index and a varying thickness along the roll angle φ

Figure I-6 shows that a plane wave is transformed into an OAM wave with $\ell = 2$ after passing through a SPP. Usually, the higher the topological charge is, the bigger the height difference is. It is also possible to maintain the height difference identical to that of the order $\ell = 1$ for the higher order modes by using a SPP with several summits [44].

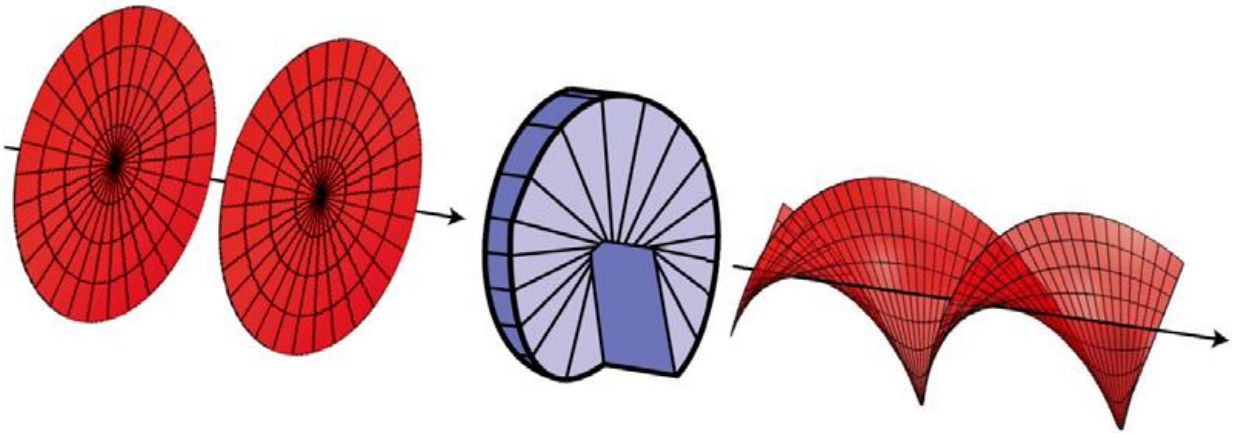

Figure I-6: A helically phased wave with $\ell = 2$ generated from a plane wave using a SPP [38]

I.2.2 Laguerre-Gaussian mode

The experiment investigated by Allen in 1992 shows that the Laguerre-Gaussian (LG) modes have rotational symmetry along their propagation axis and carry an orbital angular momentum of $\ell\hbar$ per photon [1]. The LG mode can be directly generated [45], transformed from a Hermite-Gaussian (HG) mode using a cylindrical lens mode converter [46], or produced by properly combining two HG modes [1]. For instance, a LG_{01} mode can be obtained by combining two HG modes of HG_{01} and HG_{10} with a $\pi/2$ phase difference between them, as shown in Figure I-7.

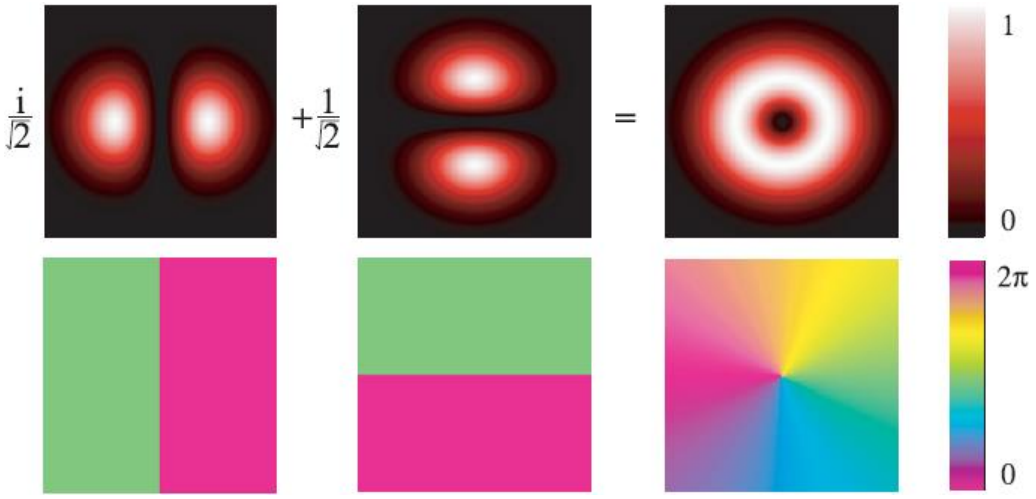

Figure I-7: Combination of two HG modes of HG_{01} and HG_{10} to produce a helically phased LG_{01} mode: normalized intensity plots (top) and corresponding phase profiles (bottom) [38]

I.2.3 Diffraction gratings

First of all, we can remind that an idealized diffraction grating is an optical component generally made up of a set of narrow parallel lines with a spacing of d, which must be wider than the wavelength of interest. It may be of the reflection or the transmission type. For a reflection grating, the above features are represented by the reflective strips and for a transmission one, by the slits. In the following part, only the case of the transmission grating will be presented, because the conclusions are similar in both cases.

When a diffraction grating is illuminated by a light beam, the slits will split or diffract the light into several beams travelling in different directions. The result is a regular alternation of constructive and destructive interferences, which creates multiple beams whose directions can be determined by the following relationship:

$$d(\sin\theta_i \pm \sin\theta_m) = m\lambda \tag{I-11}$$

where θ_i and θ_m are respectively the incidence and the diffraction angles of the light beam, λ the wavelength, d the spacing between two neighboring slits and m an integer called the diffraction order.

When the light is normally incident on the gratings ($\theta_i = 0$), the diffraction angle can be obtained by the following formula:

$$\theta_m = \arcsin(\pm m\frac{\lambda}{d}) \tag{I-12}$$

Thus, for a given frequency and incidence angle, there exists several diffracted waves propagating in different directions.

Another way to see a diffraction grating is to define it as the pattern that would be obtained by the interference between the incident and the diffracted beams. In this way, it is possible to record the interference pattern between the two beams and then to use it to generate one beam from the other. This is the technique called the “holography” proposed by D. Gabor [47]. The interference pattern is called a hologram.

In the case of a hologram for generating OAM beams, the reference beam is a Gaussian beam, and the interference pattern is characterized by ℓ-fold dislocation at its center (see Figure I-8). Due to their special shape, this type of hologram is often called a “forked diffraction grating” [48, 49]. The appropriate hologram can be generated by computer, or it can be formed by recording onto photographic film, the interference pattern between a plane wave and the beam one seeks to produce.

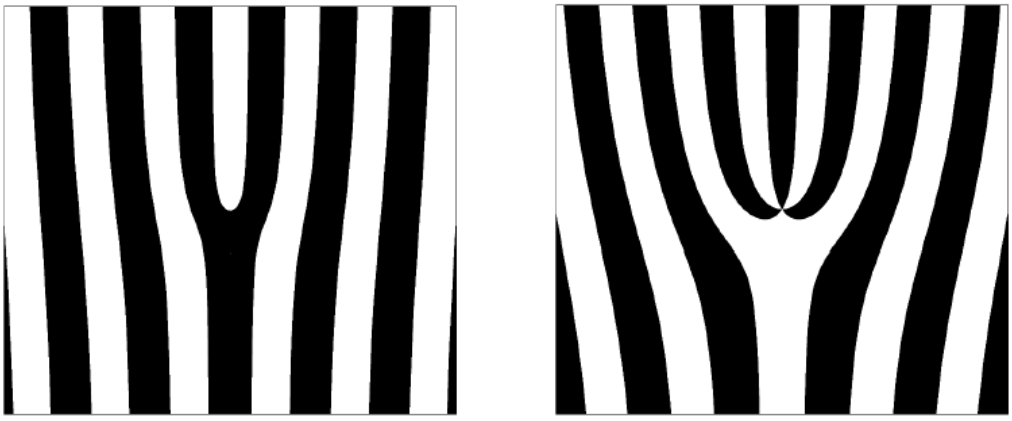

(a) (b)

Figure I-8: View of the holograms for different topological charges: (a) $\ell = 1$; (b) $\ell = 3$.

What makes the holographic approach particularly appealing is the commercial availability of spatial light modulators (SLMs) [18]. These pixelated liquid crystal devices can be programmed through the video interface of a computer to act as holograms and therefore, they have taken the place of the photographic film. Furthermore, numerically calculated holographic patterns can be displayed on an SLM. These devices produce reconfigurable, computer controlled holograms that allow a simple laser beam to be converted into an exotic beam with almost any desired phase and amplitude structure. And the beam pattern can be changed many times per second to meet experimental requirements.

As shown in Figure I-9, when the reference wave output of a conventional laser passes through a 3-fold dislocation hologram illuminated at normal incidence, three main beams are observed at the outputs [50]. Two of them are identical but propagate with opposite diffraction angles and topological charges of $\ell = \pm 3$. The third beam, not shown here, propagates in the extension of the reference wave and carries no OAM. The efficiency of this transformation is related to the level of sophistication in hologram design. For a binary hologram (see Figure I-8) which comprises only black and white areas with no grey scale, very little of the incident power ends up in the first order diffracted spot. This can be partly overcome by blazing the grating [49]. When mode purity is of particular importance, it is also possible to create rather more sophisticated holograms where the contrast of the pattern is varied as a function of radius such that the diffracted beam has the required radial profile [51].

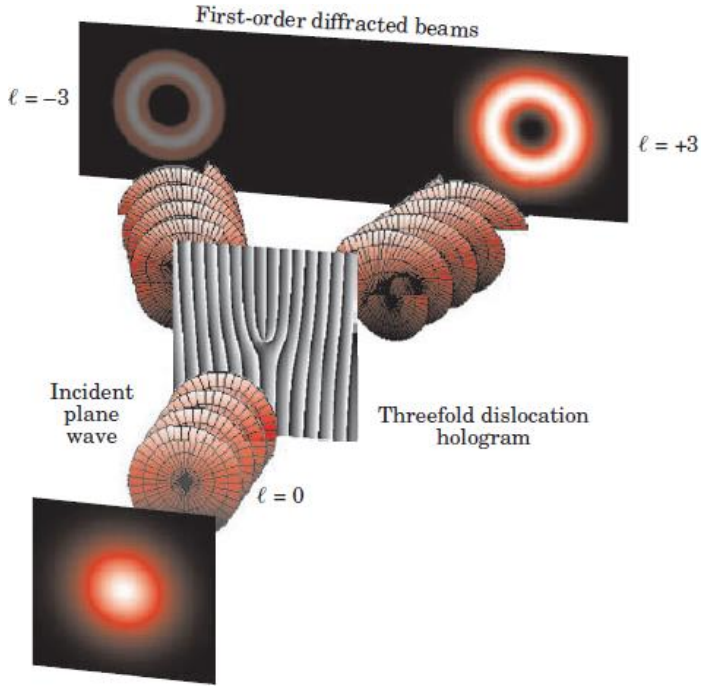

Figure I-9: A pair of helically phased waves with ℓ = ±3 transformed from a plane wave using a hologram [50]

I.3 Methods for generating OAM waves at radio frequencies

The first radio OAM simulations were performed by Thidé *et al*. in 2007 [10]. Since then, the study of EM waves carrying OAM in the radio frequency domain is growing. In addition to the application of such waves is still subject to intense debates [6, 10-13], there are also problems of generating these waves. In fact, even though the OAM is a naturally physical property in spite of the frequency, the methods available for generating OAM waves in the radio domain are not totally the same as that in optics due to the difference in the frequency scale.

Up to now, in radio frequency bands, two main families of antennas have been proposed to generate OAM waves: plane wave transformers and circular phased arrays. Both families will be presented in this section.

I.3.1 Plane wave transformers

In the first family, the OAM wave is generated by a transformation of a plane wave. Several antennas have been proposed and studied to realize this transformation.

I.3.1.1 Spiral phase plate

The first antenna presented here is brought from the optics. As presented in the last section, the Spiral Phase Plate can be used to generate optical beams carrying OAM. In the same manner, a SPP has been realized in the 30 GHz frequency band for generating radio OAM

waves [23]. Whereas in the optical field, a SPP is illuminated by a Gaussian beam that can be regarded as a plane wave, in the radio field a conventional horn antenna that is commercially available and suitable for the working frequency of the SPP is more often used as the incident wave source (see Figure I-10). The simulated results of this OAM horn antenna are presented in Figure I-11.

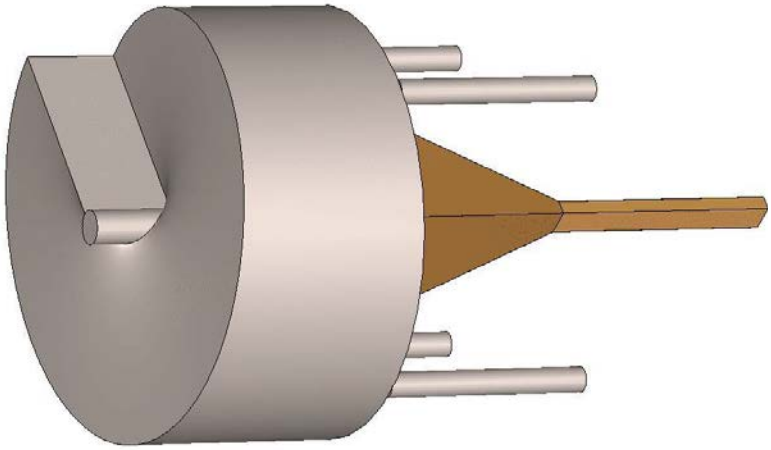

Figure I-10: Structure of the OAM horn antenna with spiral phase plate [23]

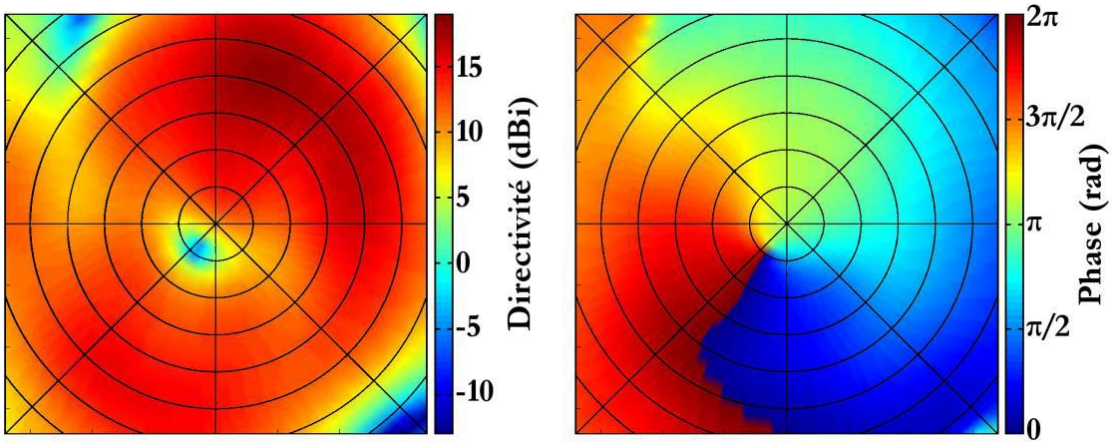

Figure I-11: Magnitude (left) and phase (right) patterns generated by the OAM horn antenna with the SPP at 30 GHz [23]

To improve the reflectivity of the SPP, an ultralow reflectivity SPP was proposed in [52]. Unlike the previous SPP which has a smooth and continuous surface, this SPP is composed of unit cells whose equivalent permittivity and thickness are designed to satisfy the impedance matching condition based on transmission line theory. Figure I-12 shows a unit cell of the SPP and the explosive view of the model including the SPP, connector and horn antenna. The reflectivity of the SPPs with impedance matching and without impedance matching is shown

in Figure I-13. It can be seen that the reflectivity of impedance matched SPP is much lower than that of no impedance-matched SPP around the designed frequency (59 GHz here).

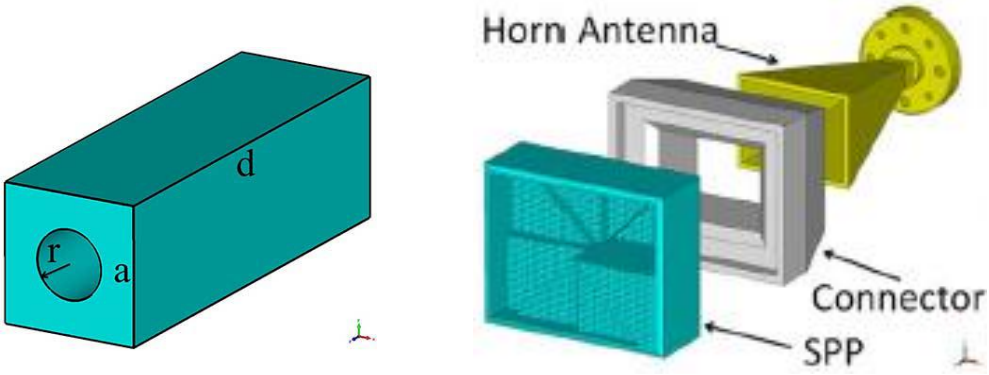

(a) (b)

Figure I-12: (a) Unit cell of the proposed SPP; (b) Explosive view of the model including the SPP, connector and horn antenna [52]

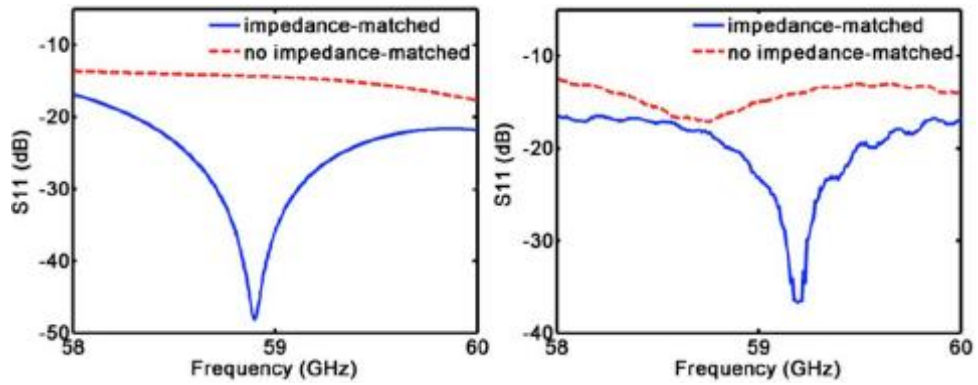

(a) (b)

Figure I-13: Reflectivity of the impedance-matched SPP and the no impedance-matched SPP: (a) the simulation results; (b) the measurement results [52]

I.3.1.2 Flat phase plate

Inspired by the technique of SPP, later a flat drilled phase plate was used to generate OAM waves (see Figure I-14) [24, 25]. It is similar to the SPP in the sense that again the phase difference of the propagated wave has a dependency with the roll angle φ. For a SPP, the phase difference depending on the roll angle φ is obtained by using a material with a constant refractive index and a varying thickness; for a flat drilled phase plate, it is reverse: the thickness is constant, but the refractive index varies with the roll angle φ. The effective permittivity ε_{eff}

of the dielectric (Teflon here) is controlled by the density of the drilled holes, and it can be calculated by:

$$\varepsilon_{eff} = \frac{\varepsilon_{mat}V_{mat}+\varepsilon_{air}V_{air}}{V_{tot}} \quad \text{(I-13)}$$

where V_{mat} and V_{air} are respectively the volumes of the dielectric and the air obtained by drilling, ε_{mat} and ε_{air} are their permittivities, and $V_{tot} = V_{mat}+V_{air}$.

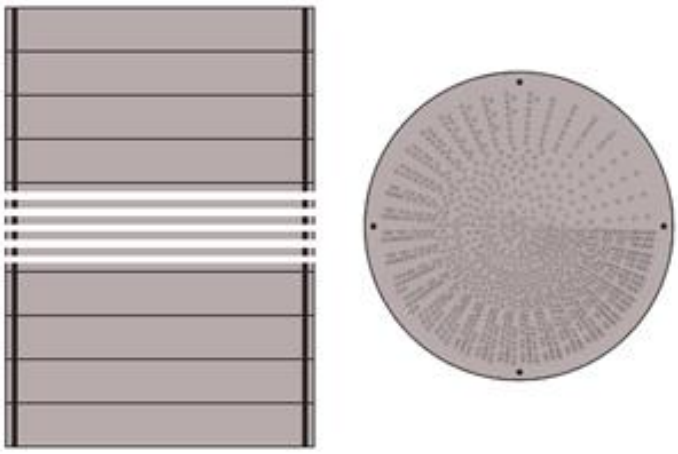

Figure I-14: Side view (left) and top view (right) of the flat drilled phase plate [25]

To ensure a good mechanical integrity, the phase plate must have as few holes as possible: the maximum ratio of the air can be selected as 33% [25], which corresponds to a minimum refractive index n_{min} of 1.35 (with a refractive index of 1.45 of Teflon). By carefully controlling the hole density at different roll angles, the refractive index can vary continuously with the roll angle between 1.35 and 1.45, as shown in Figure I-15. Consequently, the value of the refractive index is expressed as a function of the roll angle φ:

$$n(\varphi) = n_{mat} - \frac{\Delta n}{2\pi} \times \varphi \quad \text{(I-14)}$$

where n_{mat} is the refractive index of the dielectric and $\Delta n = n_{mat} - n_{min}$. To obtain a phase variation of $2\pi\ell$ in one turn, the thickness H of the flat phase plate is then:

$$H = \frac{l\lambda}{\Delta n} = \frac{l\lambda}{n_{mat}-n_{min}} \quad \text{(I-15)}$$

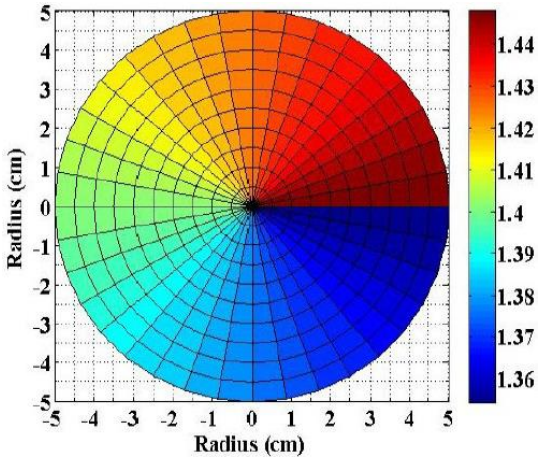

Figure I-15: Variation of the refractive index as a function of the roll angle [25]

The flat drilled phase plate is also placed after a conventional horn antenna for generating OAM waves. The simulation results are presented in Figure I-16. They are very close to those obtained for the SPP (see Figure I-11), but less regular.

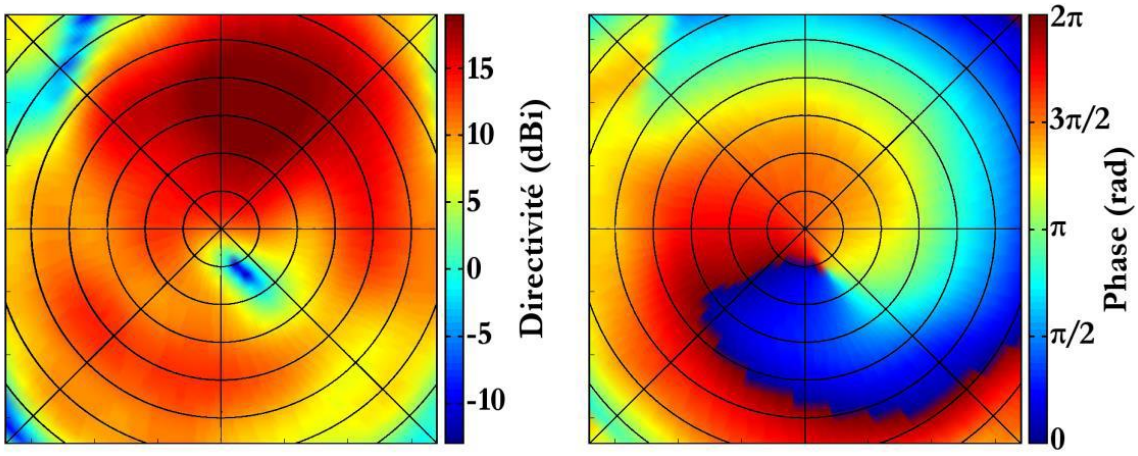

Figure I-16: Magnitude (left) and phase (right) patterns generated by the OAM horn antenna with the flat drilled phase plate [23]

This flat phase plate can only generate a single OAM mode, another one that can generate mixed OAM modes was presented in [53]. Unlike the previous flat phase plate which obtains a varying refractive index along the roll angle by controlling the hole density, this one achieves the same purpose by controlling the hole radius. The configuration of the OAM antenna is shown in Figure I-17. An open-end waveguide is used to provide an incident wave. The flat phase plate is a quasi-periodically structure, where each unit cell is made of 4 holes drilled in the substrate. By properly dividing the proposed structure into several small parts to implement individual OAM mode, OAM waves with arbitrary mixed modes can be generated. Figure I-18

shows the measured results of a single mode OAM antenna and Figure I-19, those of a two-mixed-mode antenna. For the first antenna, the transverse magnitude and phase patterns confirm the generation of an OAM wave with $\ell = 1$; for the second one, the magnitude pattern is a superposition of different OAM modes with $\ell = 2$ and $\ell = 4$, and it has a good agreement with the theoretical result in [10].

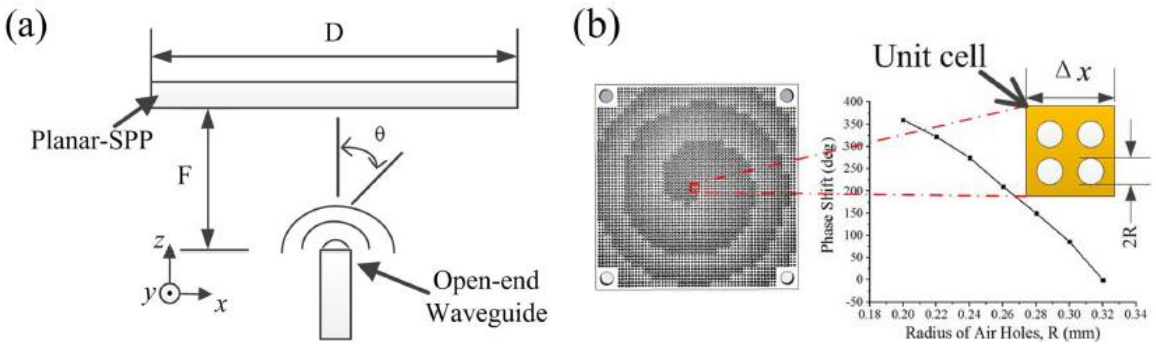

Figure I-17: (a) Side view of an open-end waveguide fed flat phase plate antenna for OAM wave generation; (b) View of a unit cell in this design and the phase shift versus hole radius [53]

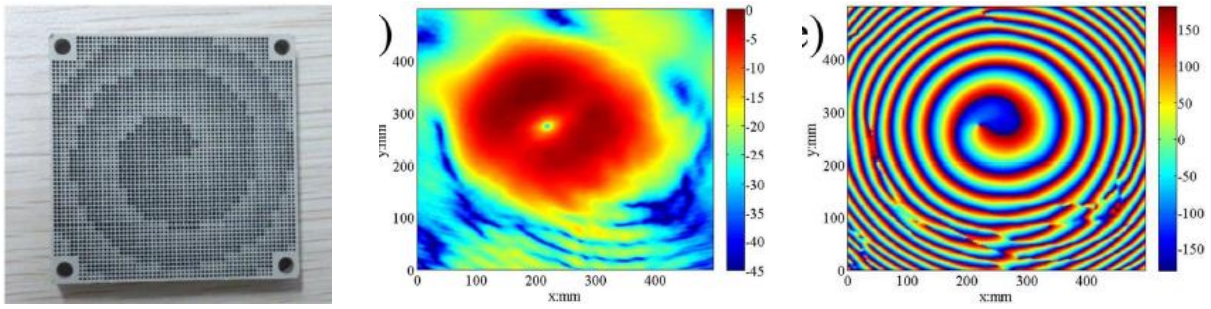

(a) (b) (c)

Figure I-18: (a) View of a single mode OAM antenna; (b) Measured transverse magnitude pattern; (c) Measured transverse phase pattern [53]

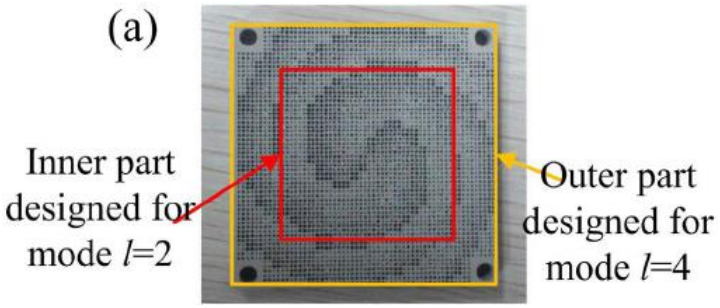

(a)

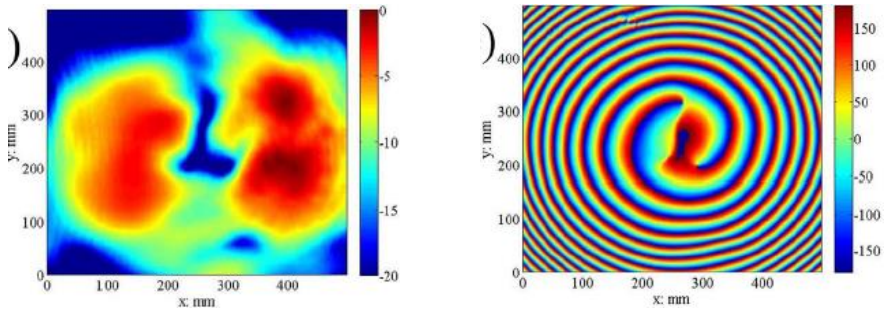

(b) (c)

Figure I-19: (a) View of a two-mixed-mode OAM antenna; (b) Measured transverse magnitude pattern; (c) Measured transverse phase pattern [53]

I.3.1.3 Diffraction grating

It was shown in the last section that a diffraction grating or a hologram is able to generate optical OAM beams. In the same manner, Mahmouli and Walker used a hologram working at a frequency of 60 GHz to generate radio OAM waves [54, 55].

Figure I-20 presents the geometry of the hologram and the corresponding intensity distribution of the far-field diffraction pattern. The hologram is realized by etching the copper on a printed circuit board. As expected, three output beams are observed in Figure I-20b. The middle peak amplitude corresponds to the Gaussian beam with no OAM characteristic and the other two beams on either side of the Gaussian beam have an intensity profile which may correspond to an OAM bearing wave. Unfortunately, it is difficult to conclude the presence or absence of the OAM wave, because no study of the phase was presented, which is essential when one wants to define a wave carrying OAM.

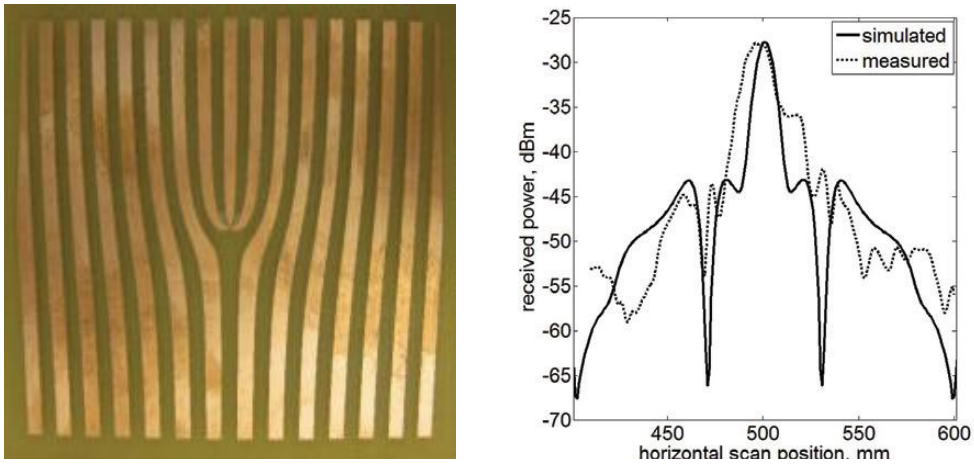

(a) (b)

Figure I-20: (a) Geometry of the hologram; (b) intensity distribution of the far-field diffraction pattern [54]

I.3.1.4 Reflector antennas

The generation of OAM waves with a reflecting system is based on a principle similar to that of the Spiral Phase Plate: the phase variation of the propagated wave has a dependency on the roll angle. In the case of the SPP, this variation is realized in the process of transmission, while in the case studied here, it is done during the reflection on a surface. Therefore, the appearances of these antennas are also close: they all have a height difference H_{max} along the roll angle of the reflector which is defined by:

$$H_{max} = \frac{1}{2} \times l \times \lambda \tag{1-16}$$

where λ is the wavelength at the working frequency, ℓ is the order of the OAM mode.

To our knowledge, only two different reflectors have been proposed to generate OAM waves. The first one is made from styrofoam blocks, covered with an electrically conductive and reflective surface [26]. To realize a total 2π phase shift in one turn, the spiral reflector is trimmed into a staircase-like structure with eight steps, where each one corresponds to a π/4 phase shift (see Figure I-21a). The measurements were performed at 2.4 GHz in a big anechoic chamber. The spatial maps (see Figure I-21b) of the magnitude and the phase of the electrical field show the existence of OAM spatial field distribution. Due to the discretization of the phase mask, the measured phase distribution is not good but remains visible.

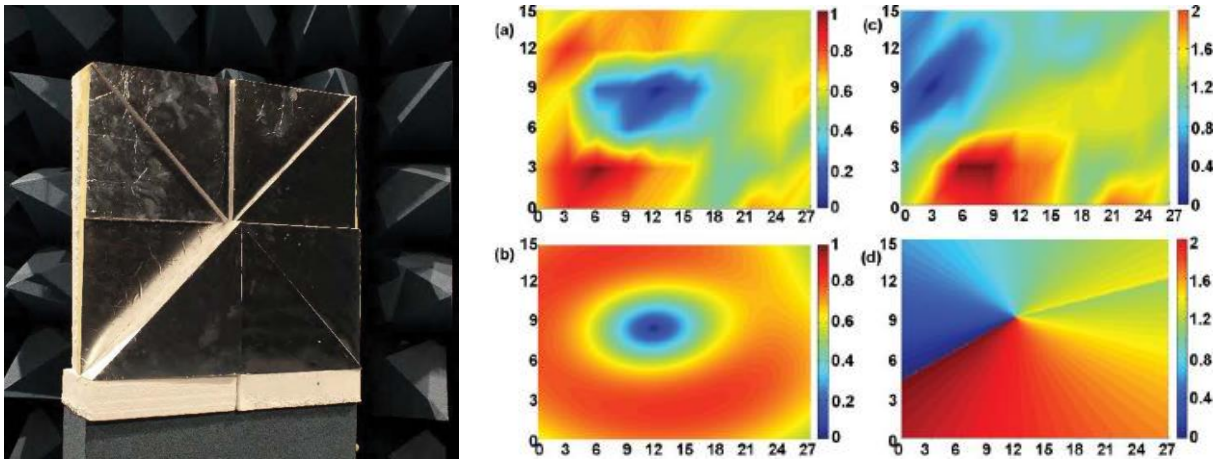

(a) (b)

Figure I-21: Generation of radio OAM waves with a spiral reflector: (a) view of the realized reflector; (b) measured (top) and simulated (bottom) results [26]

Following this experiment, a second one was done in the real environment [6]. The authors used an 80-cm twisted parabolic reflector dish, working in the 2.4 GHz frequency band, to induce a linear phase distribution along the roll angle. The elevations at different values of

roll angle are shown in Table. 1. Figure I-22b shows the intensity map of the radio beam vortex at 40 meters in open space in the region harboring the singularity. The intensity distribution in this region presents some fluctuations caused by environmental interference effects. Although they do not show, the authors state that the phase pattern confirms the expected vortex.

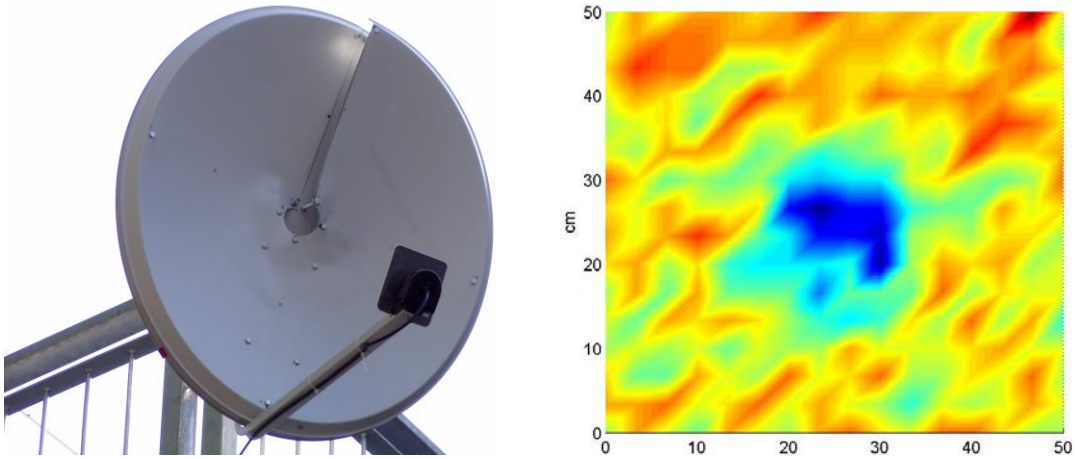

Figure I-22: (a) View of the twisted parabolic antenna; (b) intensity map in the far field [6]

Table I–1: Elevations for given values of the roll angle for deforming the parabolic antenna [6]

Roll angle	Elevation (in units of λ)	Elevation (cm)
0 = 2π	1/2	6.25
π/2	3/8	4.69
π	1/4	3.12
3/2 π	1/8	1.56

I.3.2 Circular phased arrays

The proposal to generate waves bearing OAM in the radio field was made for the first time by using a circular phased antenna array [10]. It is generally composed of *N* identical short dipoles (see Figure I-23), where each one is fed by the same signal but with an incremental phase shift compared to its neighbor. To realize a $2\pi\ell$ phase shift in one turn, the phase shift $\delta\phi$ between two successive dipoles is expressed by [5]:

$$\delta\phi = \frac{2\pi l}{N} \tag{1-17}$$

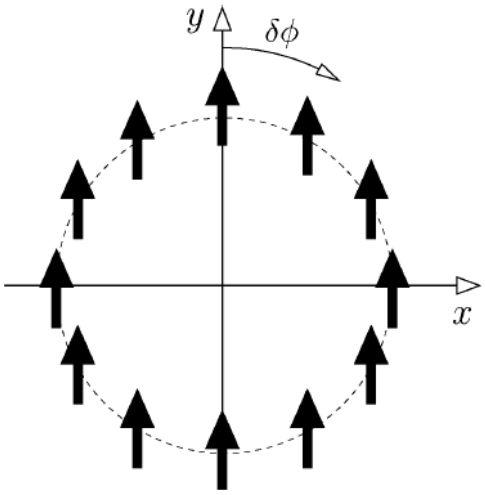

Figure I-23: Configuration of a circular antenna array (N = 12, dipoles) for generating waves bearing OAM. The phase shift δϕ between two neighboring antennas is defined in (I-17) [5].

The number of the array elements N has an additional influence on the OAM antenna: it determines the largest OAM mode l_{max} that can be generated [5], where $-N/2 < \ell_{max} < N/2$.

This method has two main advantages. The first one is that each of the antennas making up the system can be controlled independently of the others; and as a result, the second is that the phase of the generated wave can be well known and controlled. Its disadvantage is the increase of the system complexity.

Following this, several other studies showing the variations of this method have been published. The first proposal is to use a circular TSA (Time-Switched Array) to generate OAM waves at lower cost [27]. The elements of the array are excited with unit amplitude and uniform phase at a fundamental working frequency, but are energized sequentially such that each element is only switched on for a time period. Figure I-24 shows the far-field amplitude and phase patterns of the circular TSA for different OAM modes. It is observed that the amplitude pattern has a null at the center and the phase pattern has a linear variation along the roll angle with a $2\pi\ell$ phase shift in one turn. Moreover, the null size increases with the number of the OAM mode.

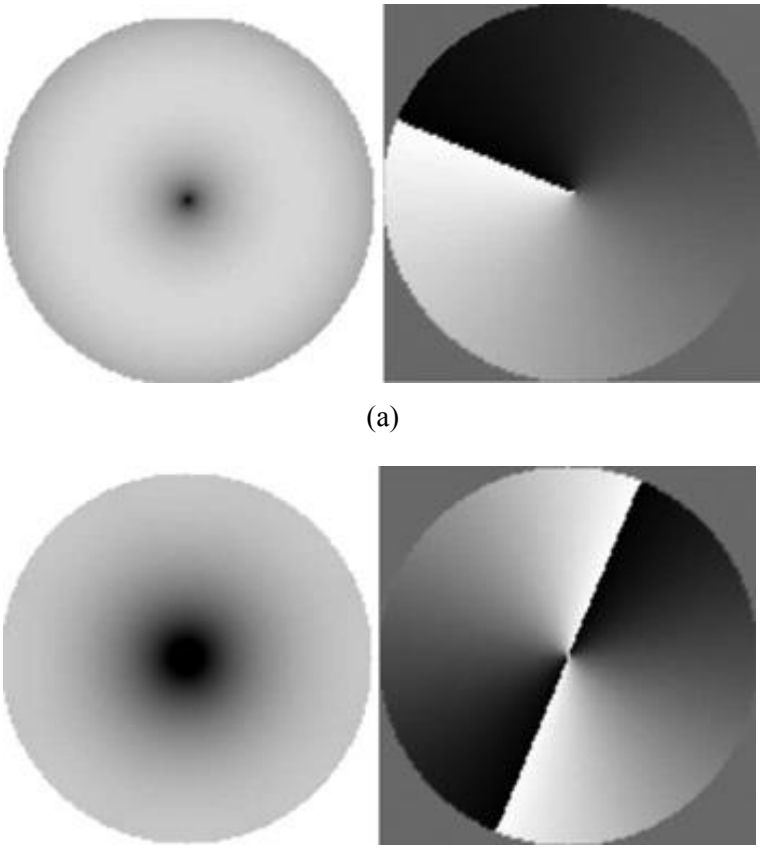

(a)

(b)

Figure I-24: Far-field amplitude (left) and phase (right) patterns generated by a circular TSA for different OAM modes: (a) $\ell = 1$; (b) $\ell = 2$ [27]

Later, in another study the same group presented the design of a circular phased array of 8 patch antennas [28]. Again, all the patch antennas are fed using the same signal but with an incremental phase shift between each patch. Besides the ideal model, the authors also give the practical design [29]. As shown in Figure I-25, for creating an OAM mode of $\ell = \pm 1$, a microstrip corporate feeding network was designed to achieve the required 45° phase difference between two neighboring antennas. Figure I-26 shows the measured phase pattern. An expected rotational phase distribution with 2π phase shift in one turn is observed.

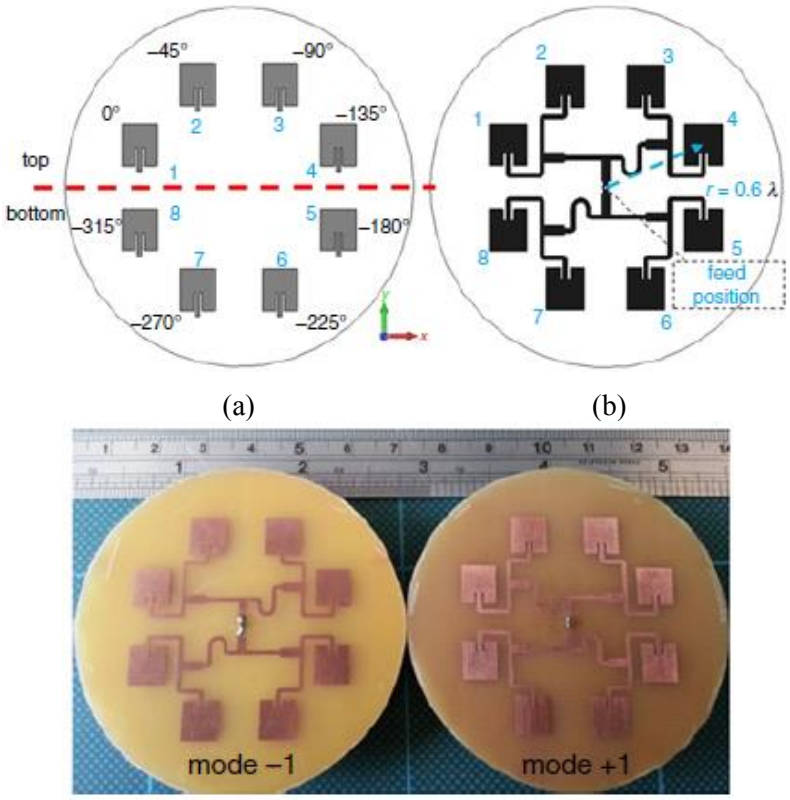

Figure I-25: Geometry of OAM circular phased array: (a) ideal model; (b) practical design; (c) prototypes [29]

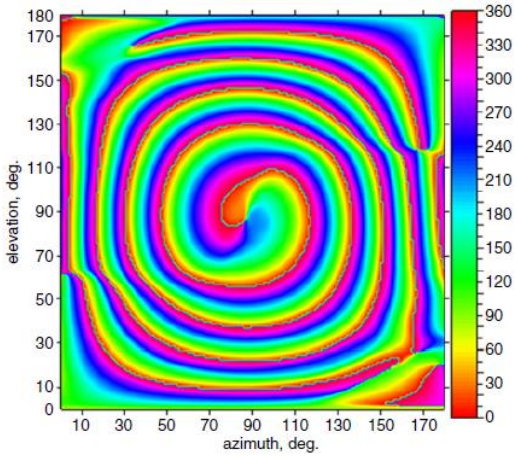

Figure I-26: Measured far-field phase pattern with an OAM mode of $\ell = 1$[29]

More recently, a circular horn antenna array (see Figure I-29) has been proposed for similar results [30]. This antenna uses the same principle and is able to generate radio OAM waves with different polarizations (linear polarization, left-hand circular polarization and right-hand circular polarization) by exciting different ports. The simulated field vector and the corresponding phase pattern of the horn antenna array for linear polarization are presented in

Figure I-30. It can be seen that the field intensity is minimum at the center and phase variation in one turn is equal to 2π. This confirms the generation of an OAM bearing wave with $\ell = 1$.

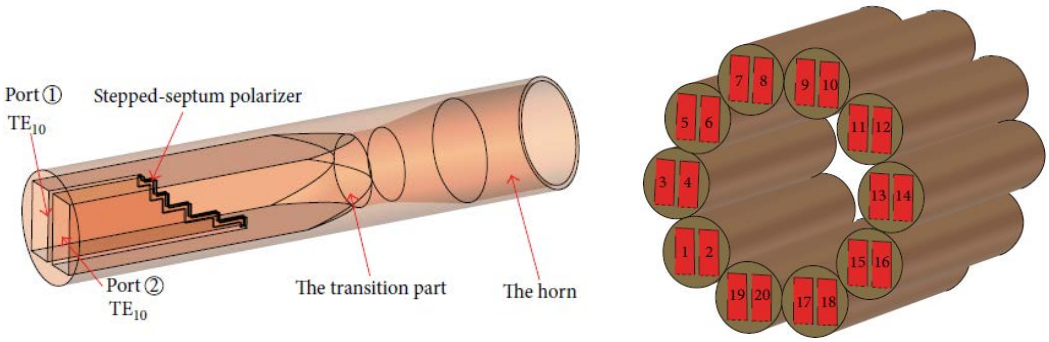

Figure I-29: Configuration of single horn antenna (left) and geometry of the horn antenna array (right) [30]

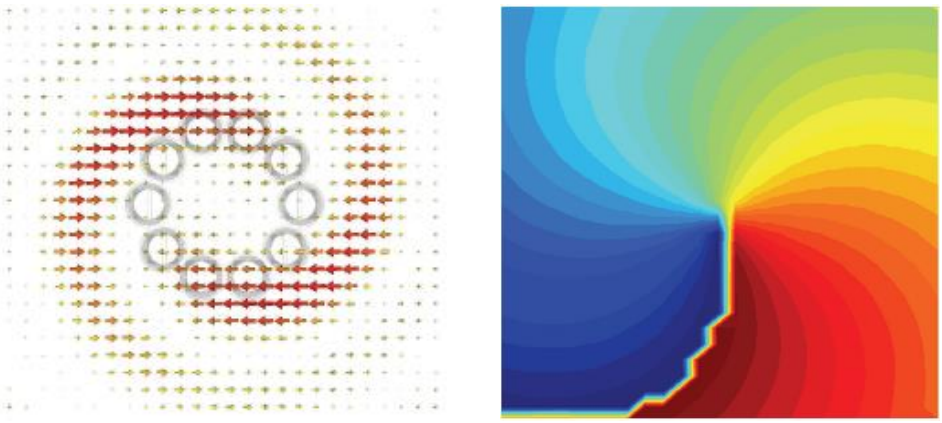

Figure I-30: Field vector (left) and the corresponding phase pattern (right) generated by the horn antenna array for linear polarization with $\ell = 1$ [30]

I.4 Conclusions

In this chapter we introduced the characteristics of the EM waves bearing OAM and reviewed the typical methods for generating such waves.

Different from a usual plane wave, the OAM waves have a helical phase front which makes it a potential candidate for radio communications [5-9] and radar applications [15-17]. Thus, it is necessary to investigate the methods for generating these waves.

In optical field, three main techniques were used to generate OAM beams: spiral phase plate, Laguerre-Gaussian mode and diffraction grating. In radio field, two main families of antennas were proposed to generate OAM waves: plane wave transformers (spiral phase plate, flat phase plat, diffraction grating and spiral reflector) and circular phased arrays.

Chapter II

Generation of Radio OAM Waves with Circular Phase Shifter and Array of Patch Antennas

II.1 Introduction

In the previous chapter, we mentioned that the circular phased antenna array is a common way to generate OAM waves in the radio frequency band. However, apart [29], the existing structures are remained mainly at simulation level.

In this chapter we present a circular phased array using an original combination of a phase shifter and a power divider to generate a wave bearing an OAM mode $\ell = 1$. Besides the design procedure and the simulation data, the full experimental characteristics of the antenna are given. This OAM-wave generator works at a frequency of 2.5 GHz. It uses four patches which are fed by a single and original transmission line. The structure is simple, compact and easy to realize. It can be used in many domains like radio communications and radar applications.

This chapter is organized as follows. Firstly, we give a brief introduction of the structure of a single patch antenna and a patch antenna array; then we investigate the influences of the array parameters on the OAM antenna performances, which is necessary for the design of a practical OAM antenna; finally, we design, realize and characterize this novel OAM antenna.

II.2 Patch antenna structure

II.2.1 Single patch antenna

A typical patch antenna is composed of a very thin metallic strip (patch), a ground plane and a substrate that separates them. The radiating patch is usually etched on the substrate by chemical method, and it may be square, rectangular, circular, elliptical or any other geometry. There are many configurations that can be used to feed the patch antennas. The four most popular are the microstrip line, coaxial probe, aperture coupling and proximity coupling.

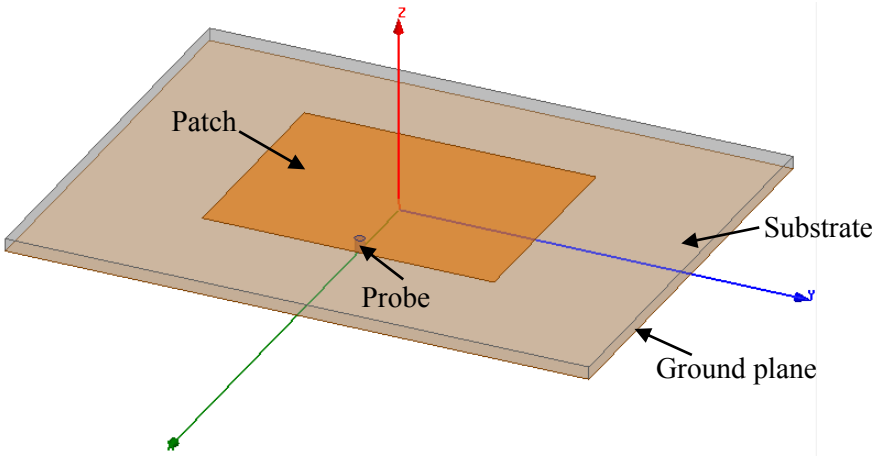

Figure II-1: 3D model of a single patch antenna

In our design, we use a rectangular patch antenna that is manufactured on a FR4 substrate and probe fed. The substrate has a thickness of 1.6 mm and a relative permittivity of 4.4. The 3D model of a single patch antenna is shown in Figure II-1. The equations for calculating the width W and the approximate length L of a patch antenna can be easily found in an antenna handbook, and they are expressed as following [56]:

$$W = \frac{c}{2f_r}\sqrt{\frac{2}{\varepsilon_r+1}} \tag{II-1}$$

$$L \approx \frac{c}{2f_r\sqrt{\varepsilon_r}} \tag{II-2}$$

where c is the speed of light in free space, f_r the resonant frequency of the patch antenna, and ε_r the relative permittivity of the substrate. Thus, when the patch antenna resonates at 2.5 GHz, the calculated width and length are respectively 36.5 and 28.6 mm. However, since some of the waves radiated by the patch travels in the substrate, some in the air, ε_r needs to be replaced by an effective dielectric constant ε_{reff}. Besides, due to the fringing effect, the patch looks greater than its actual dimension with an extension in length on each end by a distance of ΔL. Consequently, equation (II-2) is modified as following:

$$L = \frac{c}{2f_r\sqrt{\varepsilon_{reff}}} - 2\Delta L \tag{II-3}$$

where

$$\varepsilon_{reff} = \frac{\varepsilon_r+1}{2} + \frac{\varepsilon_r-1}{2}\left(1+12\frac{h}{W}\right)^{-\frac{1}{2}} \tag{II-4}$$

$$\Delta L = 0.412 \times \frac{(\varepsilon_{reff}+0.3)\left(\frac{W}{h}+0.264\right)}{(\varepsilon_{reff}-0.258)\left(\frac{W}{h}+0.8\right)} \times h \tag{II-5}$$

where h is the thickness of the substrate.

The recalculated length of the patch antenna using the new equation is equal to 28.2mm, which is the initial value used for simulation. According to the simulations, to resonate at 2.5 GHz, the length of single patch antenna is 27.4 mm. Moreover, the input impedance of the patch antenna has a dependency with the position of the feeding point. To realize a 100 Ω impedance matching, the position of the probe is optimized at 3.7 mm from the bottom side of the patch antenna. Figure II-2 presents the simulated reflection coefficient of a single patch antenna and Figure II-3, its 3D radiation pattern. We can see that it resonates at 2.5 GHz and its magnitude pattern maximum is in the boresight direction.

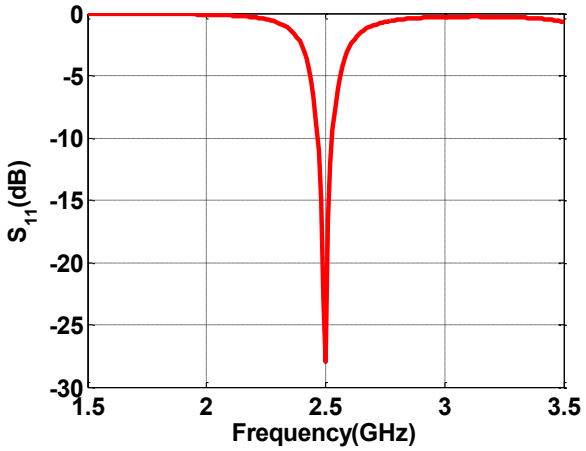

Figure II-2: Simulated reflection coefficient of a single patch antenna

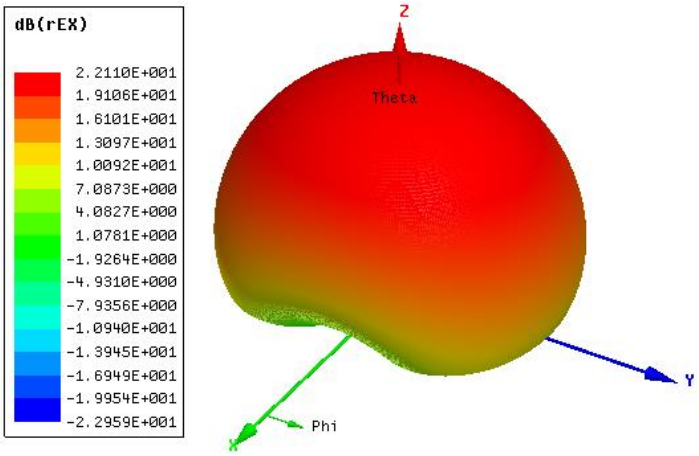

Figure II-3 Simulated 3D radiation pattern of a single patch antenna

II.2.2 Patch antenna array

The patch antenna array consists of N identical radiating elements that are located on a circle, as shown in Figure II-4. Here $N = 4$. The array elements are still manufactured on a FR4 substrate with a thickness of 1.6 mm and a relative permittivity of 4.4 and probe fed. The array radius is set as $0.5\times\lambda$ to obtain a weak mutual coupling between the array elements. Figure II-5 shows the simulated reflection and transmission coefficients of the circular patch array. It can be seen that the mutual coupling is below -30 dB and the resonant frequency of each element is shifted up by 19 MHz. To maintain the resonant frequency at 2.5 GHz, the patch length needs to be increased to 27.6 mm.

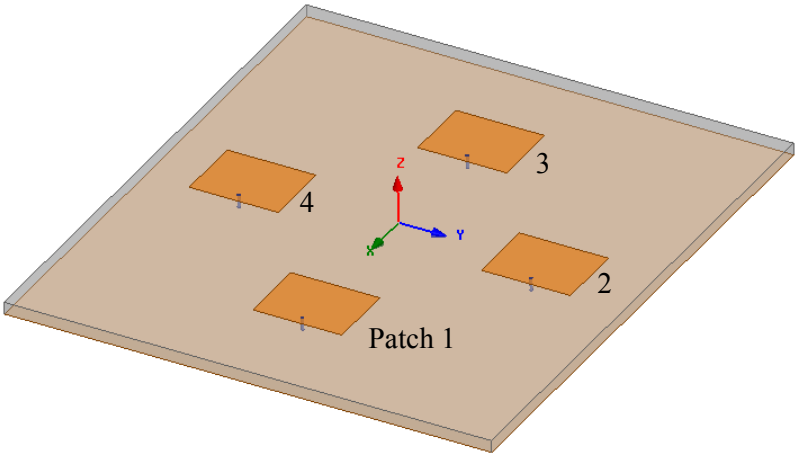

Figure II-4: 3D model of a 4-patch-antenna array

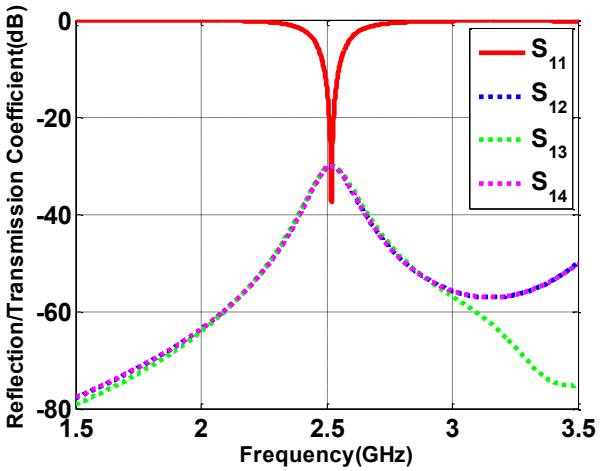

Figure II-5: Simulated reflection and transmission coefficients of the circular patch array

II.3 Parametric study of the circular phased patch array

In Thidé's work [10], the circular phased array for generating OAM waves is composed of *N* short dipoles, where each one is fed using the same signal but with an incremental phase shift compared to its neighbor. However, this antenna is only at simulation level. Here we intend to use patch antennas for the purpose of realization. Compared to the dipoles, the patches have two major advantages: 1) the radiation of the dipole can be considered as omnidirectional, i.e. it radiates in both the front and back directions in the plane perpendicular to the dipole. With the patch, the back radiation is considerably decreased and therefore, the radiated power is doubled in the forward direction; 2) the dipole needs a symmetric power supply, typically with 2 parallel wires. However, the patch can be directly supplied by a coaxial cable and therefore, needs no "balun" which further complicates the antenna realization.

In this part we make a detailed parametric study of the ideal phased patch array, which is the first step to design a practical OAM antenna.

II.3.1 Number of array elements

We have firstly varied the number of the array elements to study its influences on the quality of the generated OAM wave at 2.5 GHz. The array radius is kept at 60 mm (0.5×λ). To create an OAM mode $\ell = 1$ with N patch antennas, the phase step between each element should be equal to $2\pi\ell/N = 2\pi/N = 360°/N$. Thus, when N is equal to 4, 6 or 8, the corresponding phase steps between each array element are respectively 90°, 60° and 45°, as shown in Figure II-6.

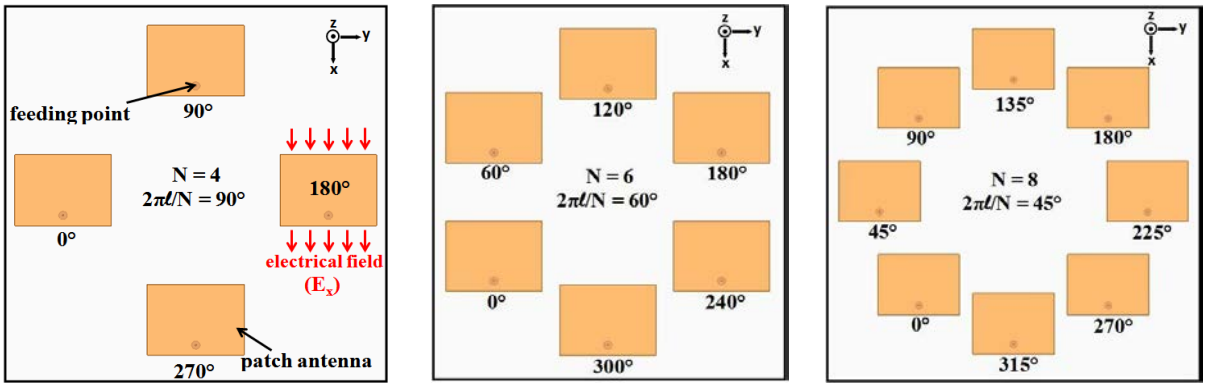

(a) (b) (c)

Figure II-6: Geometry of the phased patch array with different numbers of array elements: (a) N = 4; (b) N = 6; (c) N = 8

Figure II-7 presents the two-dimensional (2D) transverse phase and magnitude patterns of the E_x component (see Figure II-6(a)) of the generated wave with different values of N. The observation window is a circular area with a radius of 300 mm, lying 60 mm above the patch antenna array. As shown, the phase pattern has a 2π variation in one turn and the magnitude pattern has a null at the center. This confirms the generation of an OAM wave with $\ell = 1$. In addition, as N increases, the quality of the generated wave becomes better, but the array becomes larger and more complex to realize. Figure II-8 shows the 3D radiation patterns (in linear value) of the circular phased patch array. We can observe that the radiation pattern is more uniform with a larger N.

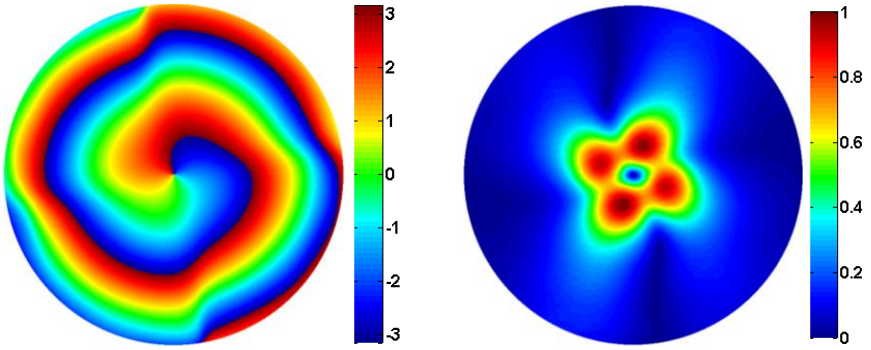

(a)

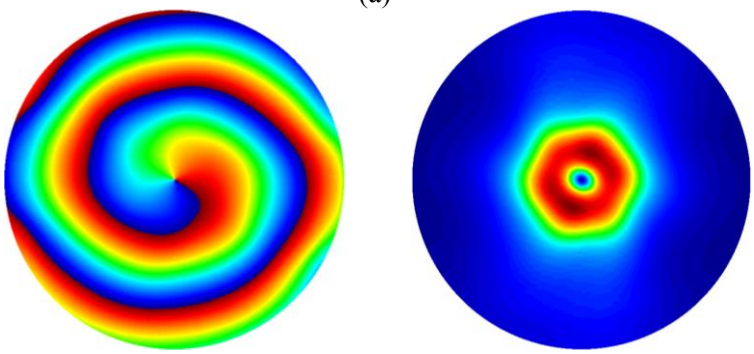

(b)

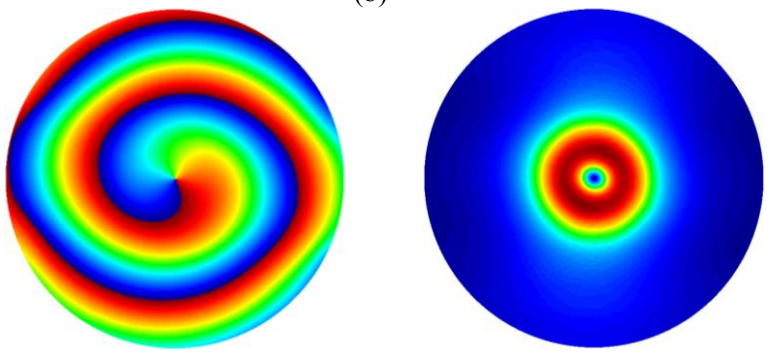

(c)

Figure II-7: 2D phase (left) and magnitude (right) patterns of E_x component for OAM mode $\ell = 1$ with different numbers of array elements at 2.5 GHz: (a) N = 4; (b) N = 6; (c) N = 8.

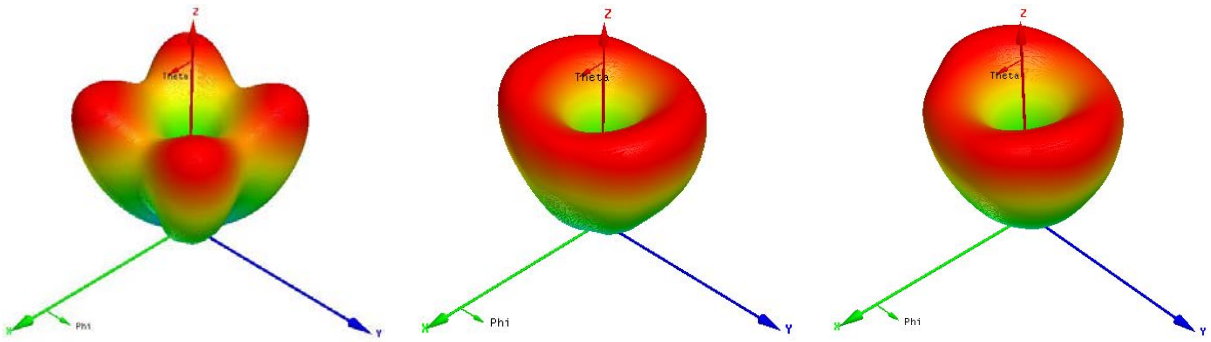

(a) (b) (c)

Figure II-8: 3D radiation patterns for OAM mode $\ell = 1$ with different numbers of array elements at 2.5 GHz: (a) N = 4; (b) N = 6; (c) N = 8.

According to [5], we can know that to create an OAM wave with a circular phased array of N antennas, the theoretically largest OAM mode ℓ_{max} that can be generated is predicted by the following equation: $-N/2 < \ell_{max} < N/2$. Therefore, we use $N = 8$ patch antennas (see Figure II-6(c)) to generate different OAM modes at 2.5 GHz. When the elements are all in phase, no OAM wave is generated (i.e. $\ell = 0$); when they are fed using the same signal but with an incremental phase shift of $2\pi\ell/8$ between each element, the corresponding OAM mode is produced.

Figure II-9 presents the 2D magnitude and phase patterns of E_x component of the generated wave for different OAM modes of $\ell = 0, 1, 2, 3$. The observation window is still a circular area with a radius of 300 mm, lying 60 mm above the patch antenna array. We can note that for $\ell = 0$, the phase and magnitude patterns correspond to a plane wave; for $\ell = 1, 2, 3$, the phase pattern has a linear variation along the roll angle with a $2\pi\ell$ phase shift in one turn and the magnitude pattern has a null at the center. This shows indeed that an OAM bearing wave is generated. Moreover, as ℓ increases, the null size becomes larger and the generated OAM wave becomes less uniform and more disperse. The 3D radiation patterns (in linear value) are shown in Figure II-10. We can observe the characteristics similar to those of the E-field magnitude pattern.

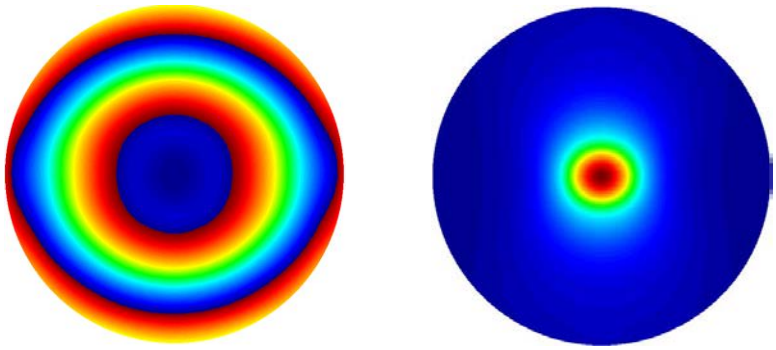

(a)

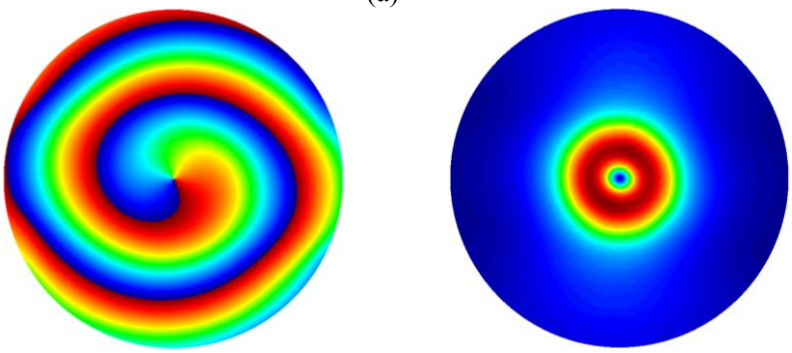

(b)

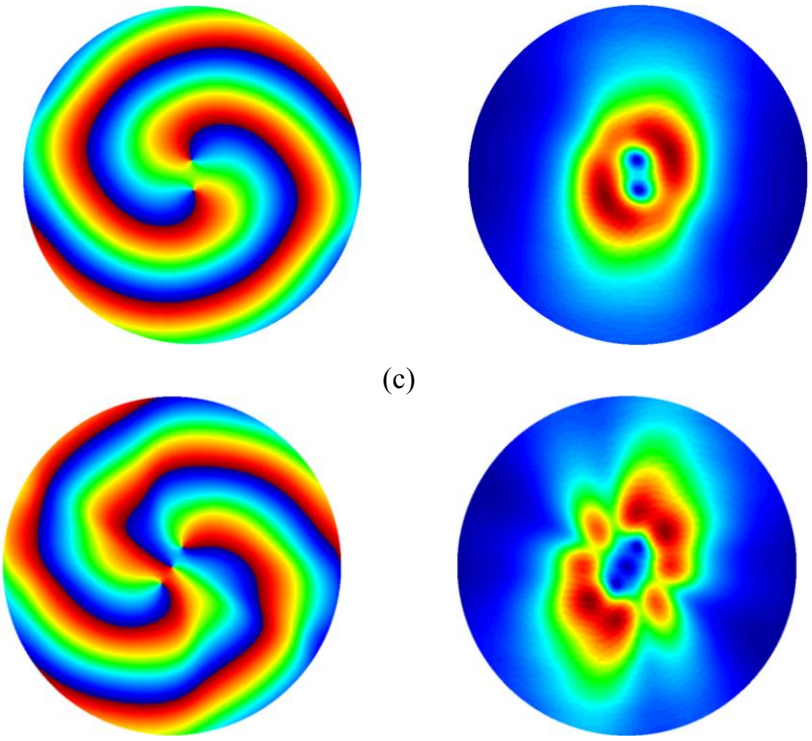

(c)

(d)

Figure II-9: 2D phase (left) and magnitude (right) patterns of E_x component for different OAM modes with N = 8 at 2.5GHz: (a) $\ell = 0$; (b) $\ell = 1$; (c) $\ell = 2$; (d) $\ell = 3$.

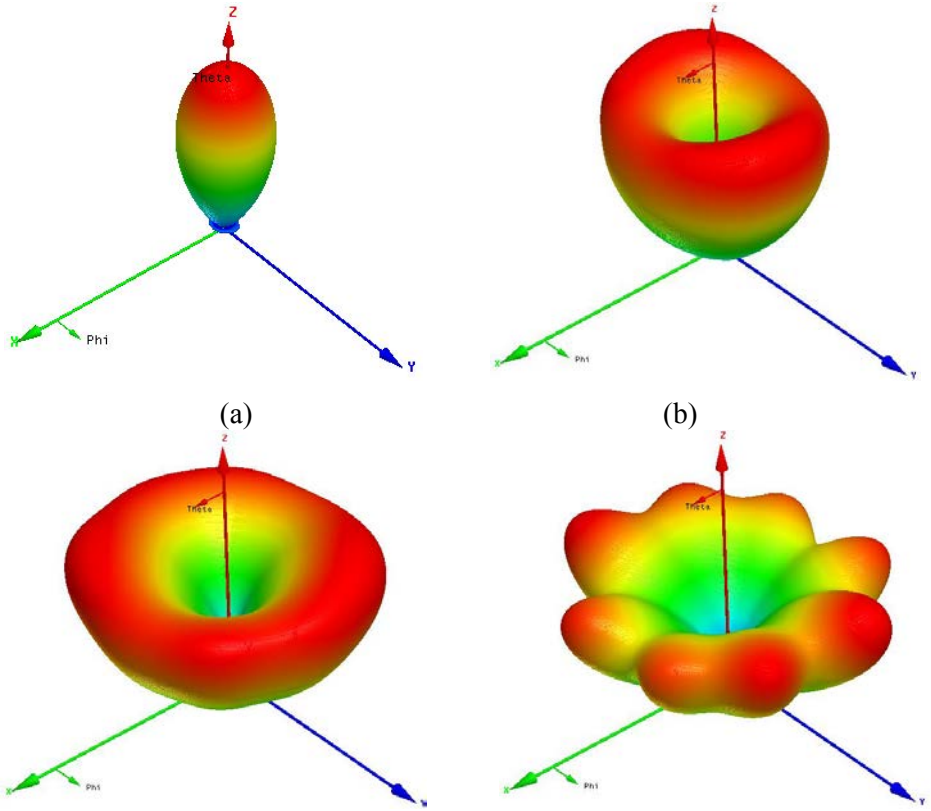

(a) (b)

(c) (d)

Figure II-10: 3D radiation patterns for different OAM modes with N = 8 at 2.5 GHz: (a) $\ell = 0$; (b) $\ell = 1$; (c) $\ell = 2$; (d) $\ell = 3$.

II.3.2 Array radius

The array radius R is another important parameter of the circular phased array. To study its influences on the properties of the generated OAM wave, we use an array of 4 patch antennas (see Figure II-6(a)) to generate an OAM mode of $\ell = 1$ at 2.5 GHz. Figure II-11 presents the 3D radiation patterns and the corresponding 2D E-plane radiation patterns with different array radiuses of $0.4\times\lambda$, $0.7\times\lambda$ and λ. It can be observed that the OAM waves become more directive as the array radius increases, but naturally some side lobes appear and the antenna geometry becomes larger. When the array radius keeps increasing, the side lobe level becomes closer to the main lobe, which means a strong loss of energy.

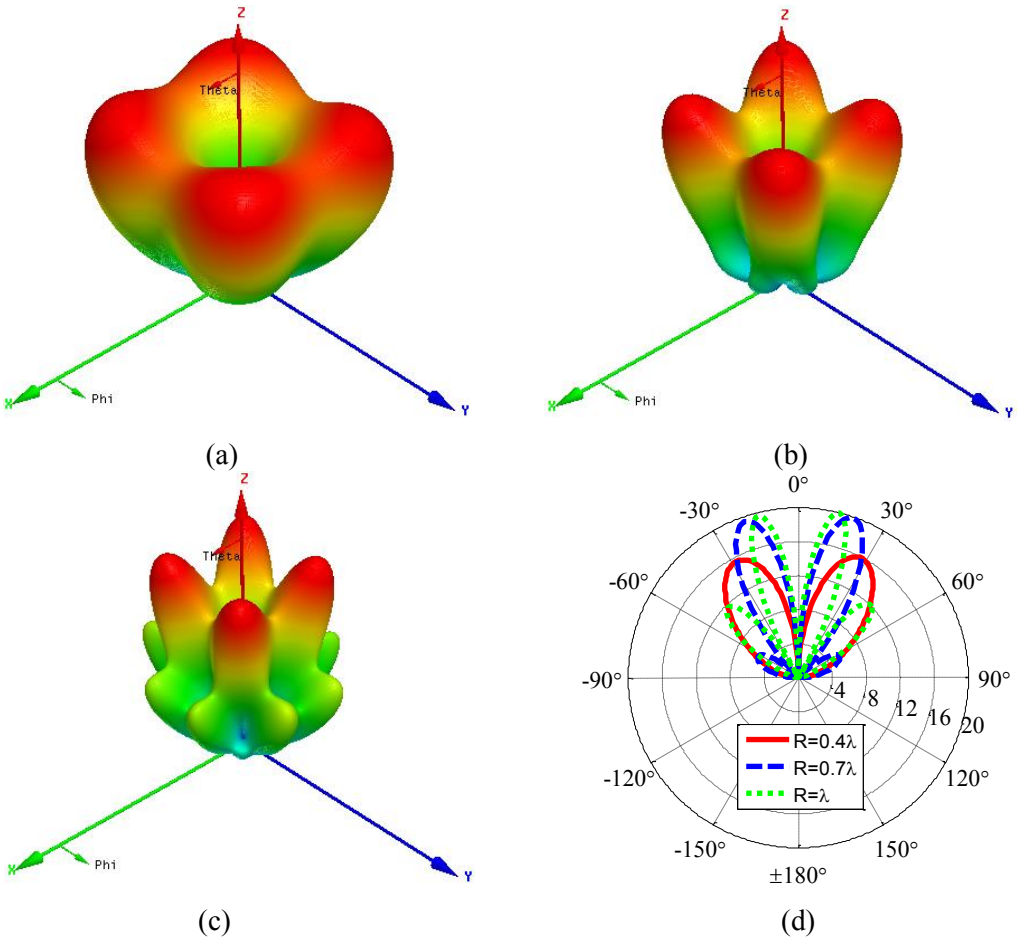

Figure II-11: 3D and 2D radiation patterns for OAM mode $\ell = 1$ with different array radiuses at 2.5 GHz: (a) $R = 0.4\times\lambda$; (b) $R = 0.7\times\lambda$; (c) $R = \lambda$; (d) E-plane radiation pattern.

II.4 OAM antenna design

According to the above analysis, it can be concluded that $N = 4$ is the smallest number of array elements for generating an OAM wave with a quite good quality. In this case, the array is

smaller and easier to realize. Therefore, we developed a new antenna using four patches and an original and simple phase shifter-power divider to generate an OAM wave with $\ell = 1$. The full design procedure of this "OAM antenna" will be presented in this part.

II.4.1 Design of phase shifter-power divider

For creating an OAM mode $\ell = 1$ with $N = 4$ antennas, the phase step between each element should be $2\pi\ell/N = \pi/2$ radians = 90°. To this purpose, an original circular phase shifter-power divider is designed which supplies the required 90° phase difference between two neighboring antennas, as shown in Figure II-12. The combined phase shifter and power divider is manufactured on a FR4 substrate with a thickness of 1.6 mm and a relative permittivity of 4.4. It works at 2.5 GHz and has 5 ports: port1 is the input and is matched to 50 Ω, while the others are used as outputs to feed the patch antennas located on a circle with a radius of 50 mm. The impedance of each part of the microstrip arcs is marked in Figure II-12. HFSS software is used to optimize the length and the width of the arcs to ensure the antenna matching, a uniform amplitude at the output ports and a 90° phase shift between two successive outputs.

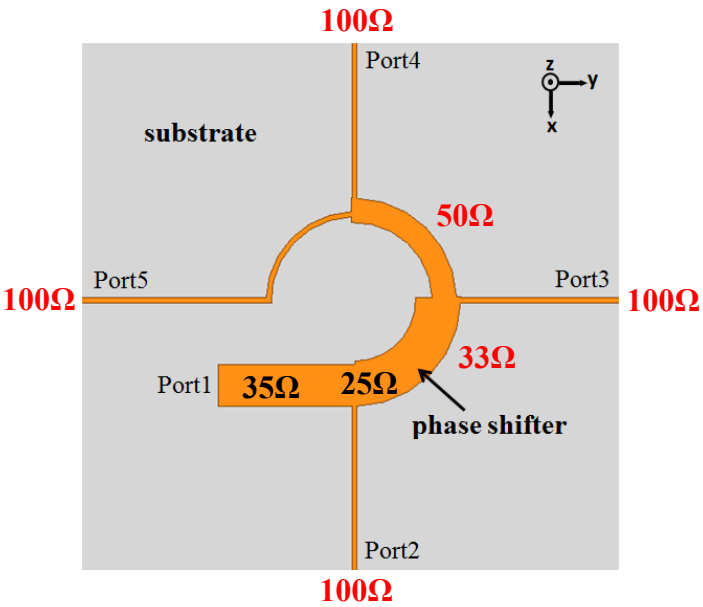

Figure II-12: Geometry of the phase shifter-power divider

The simulated results of the phase shifter-power divider are shown in Figure II-13. We can observe that at 2.5 GHz (vertical black line), the phase shifts between two neighboring ports are around 90° (max. error = ±2°) and the amplitudes of all the ports are nearly the same (max. error = ±0.3dB). Thus, the phase shifter-power divider has quite a good agreement with the required specifications.

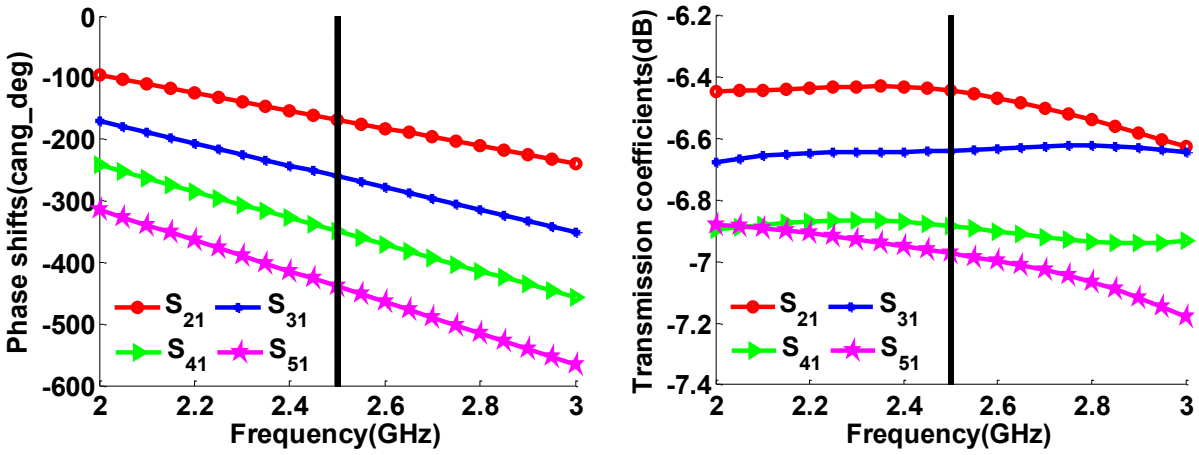

Figure II-13: Simulated parameters of the phase shifter-power divider: phase shifts (left) and transmission coefficients (right). At 2.5 GHz, the phase shifts of S_{21}, S_{31}, S_{41}, S_{51} are -168°, -261°, -350°, -439°, respectively; and the corresponding amplitudes are -6.4 dB, -6.6 dB, -6.9 dB, -7 dB.

Finally, it can be remarked that using a mirror effect, the phase shifter can be used to feed an antenna bearing an OAM mode $\ell = +1$ or -1.

II.4.2 Design of OAM antenna

II.4.2.1 Simulation model

The practical design of the OAM antenna is shown in Figure II-14. It consists of a circular phase shifter-power divider and an array of patch antennas which are both manufactured on FR4 substrates with a thickness of 1.6 mm and relative permittivity of 4.4. All the patch antennas are connected with the phase shifter-power divider through probes and fed by a 50 Ω coaxial cable from the back side of the substrate. The length and width of single patch antenna are 27.6 mm and 36.5 mm, respectively. To satisfy the impedance matching, the position of the feeding point is optimized at 5.2 mm from the bottom side of the patch antenna.

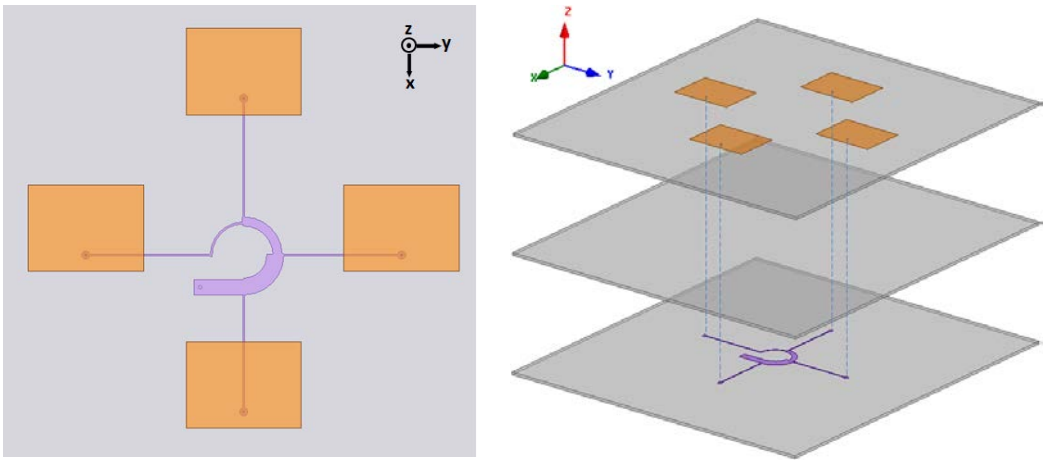

(a) (b)

Figure II-14: Configuration of the OAM antenna: (a) Top view; (b) 3D view

The 2D magnitude and phase patterns of the E_x component (see Figure II-6(a)) of the generated wave, observed on a plane perpendicular to the direction of propagation, are plotted in Figure II-15. The observation window is a circular area with a radius of 100 mm, lying 60 mm above the patch antenna array. It can be seen that the magnitude at the center is much smaller than the surroundings and the phase rotates around the center with a 2π phase shift in one turn. This shows indeed that both the amplitude and the phase correspond to an OAM bearing wave with $\ell = 1$. Figure II-16 shows the 3D radiation and phase patterns of the OAM antenna for the main polarization E_x. The 3D polar (spherical) radiation pattern depicts the central hole that is characteristic of OAM waves. The spiral form of the phase pattern, plotted in polar coordinates, corresponds to the linear variation of the phase versus the roll angle (φ, in Figure II-16).

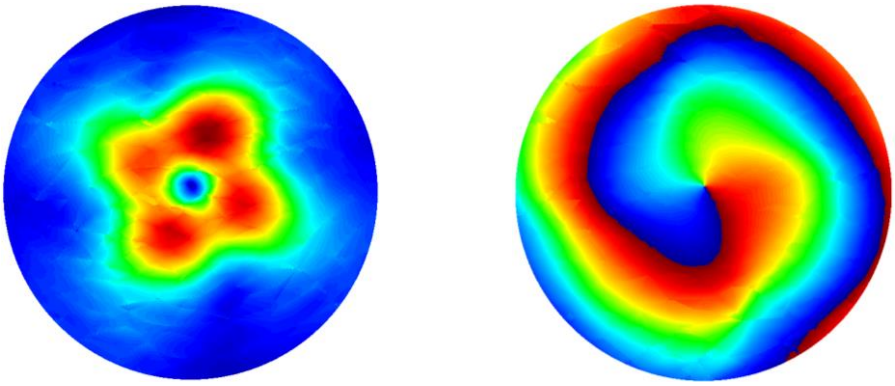

Figure II-15: 2D magnitude (left) and phase (right) patterns of E_x component for the OAM antenna at 2.5 GHz

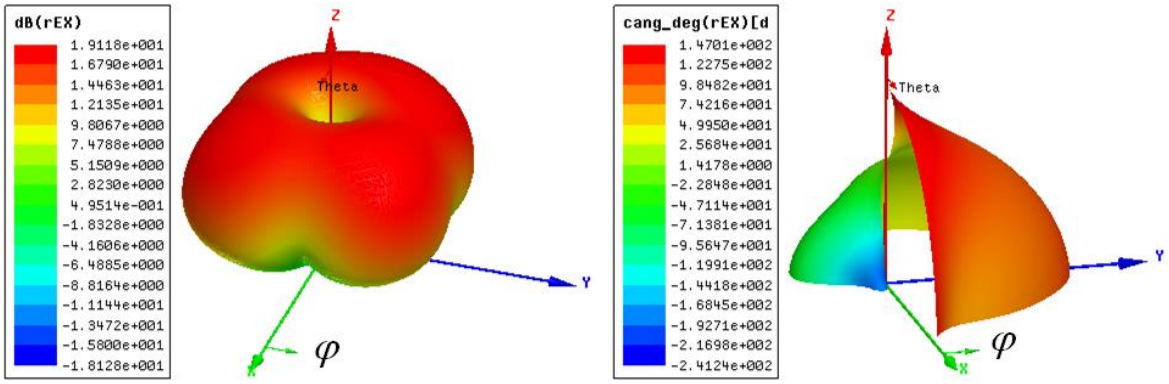

(a) (b)

Figure II-16: 3D radiation and phase patterns of the OAM antenna at 2.5 GHz: (a) Amplitude; (b) Phase.

II.4.2.2 Realized prototype

The prototypes of the phase shifter-power divider and the OAM antenna realized for the validation of the simulation results are presented in Figure II-17. The measurements are performed in an anechoic chamber. A vector network analyzer (VNA) generates a frequency ramp from 2.44 to 2.62 GHz with a 20 MHz frequency step.

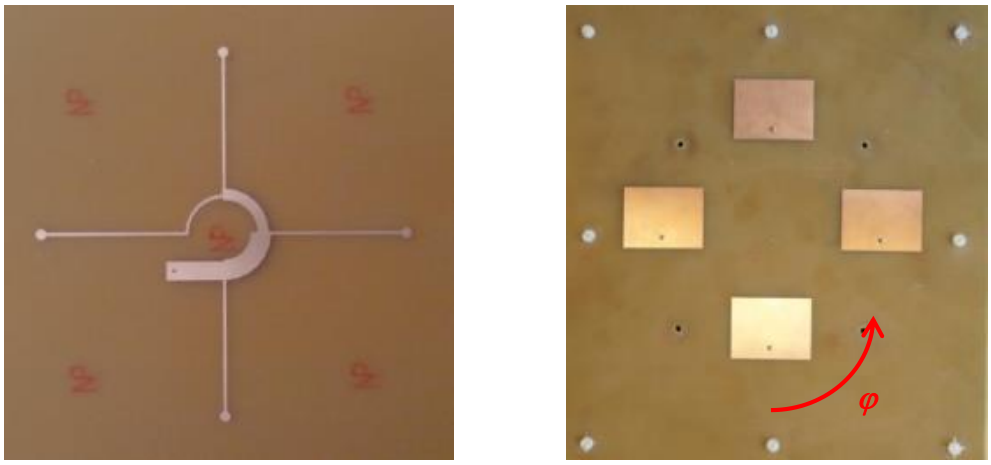

Figure II-17: View of the realized phase shifter-power divider (left) and the OAM antenna (right)

The measurement setup is presnted in Figure II-18. The OAM antenna is characterized on the Rx side and the transmitting horn antenna is located at the other end of the chamber. Measurements have been made using a VNA. To realize the measurements in all the space directions, the OAM antenna rotates around its own axis (roll angle φ, see Figure II-17) for a whole turn with a step of 1°. On the other hand, for each value of the roll angle, the antenna support also rotates around its own axis (spherical angle θ, see Figure II-18) from -100° to 100° ($\theta = 0°$, when the OAM antenna faces to the transmitting antenna) with a step of 1°. The OAM antenna is characterized for both horizontal and vertical polarizations. From these measurements, the field of the main polarization E_x is determined using this express:

$$E_x = E_V \cos\varphi + E_H \cos\theta \sin\varphi \qquad \text{(II-6)}$$

where E_H and E_V are respectively the E-fields of the horizontal and vertical polarizations.

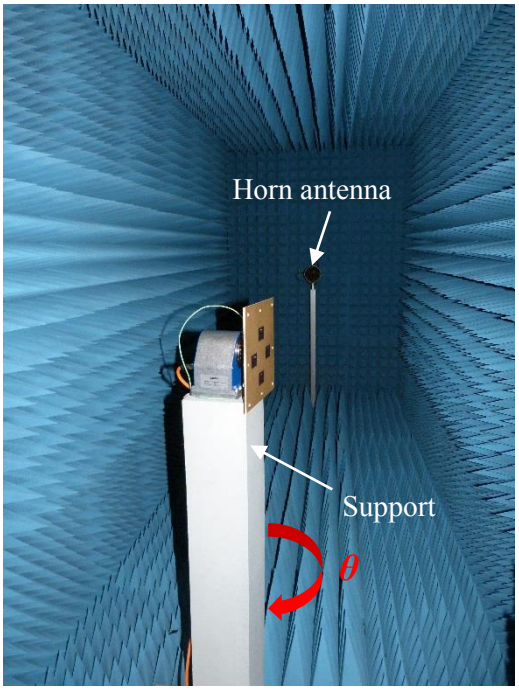

Figure II-18: View of the measurement setup

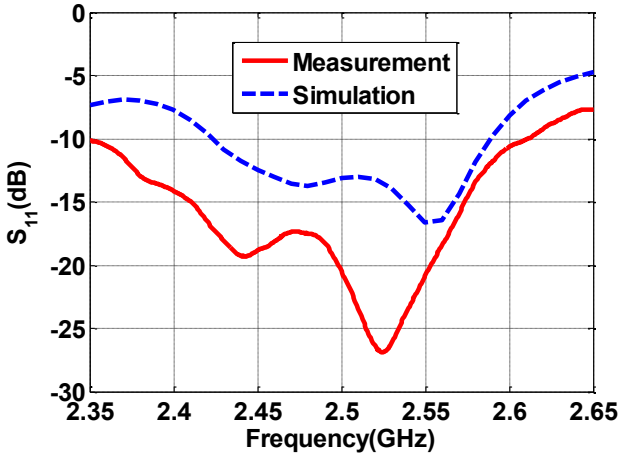

Figure II-19: Simulated and measured return losses of the OAM antenna

As depicted in Figure II-19, the OAM antenna is well matched around 2.5 GHz. Simulated and measured return-loss curves have the same form. The 2D radiation patterns (Figure II-20a) correspond to the xOz ($\varphi = 0°$) and yOz ($\varphi = 90°$) cuts of the 3D plot of Figure II-16a. The agreement between measured and simulated results is very good. The phase patterns are shown in Figure II-20b. We compare the results for three values of the spherical angle (aperture) θ: 10°, 30° and 50°. The spiral form of the phase variation versus roll angle φ is due to the polar representation of the linear phase variation ($\alpha = \varphi$). Both the simulated and measured results have a phase variation of 360° in one turn corresponding to an $\ell = 1$ OAM mode. Discrepancy

between theoretical and experimental results is very weak for small θ angle, but increases with θ. Consequently, the ideal OAM behavior is respected in the vicinity of the vortex and the agreement remains still good until $\theta = 30°$, where the beam amplitude is maximum.

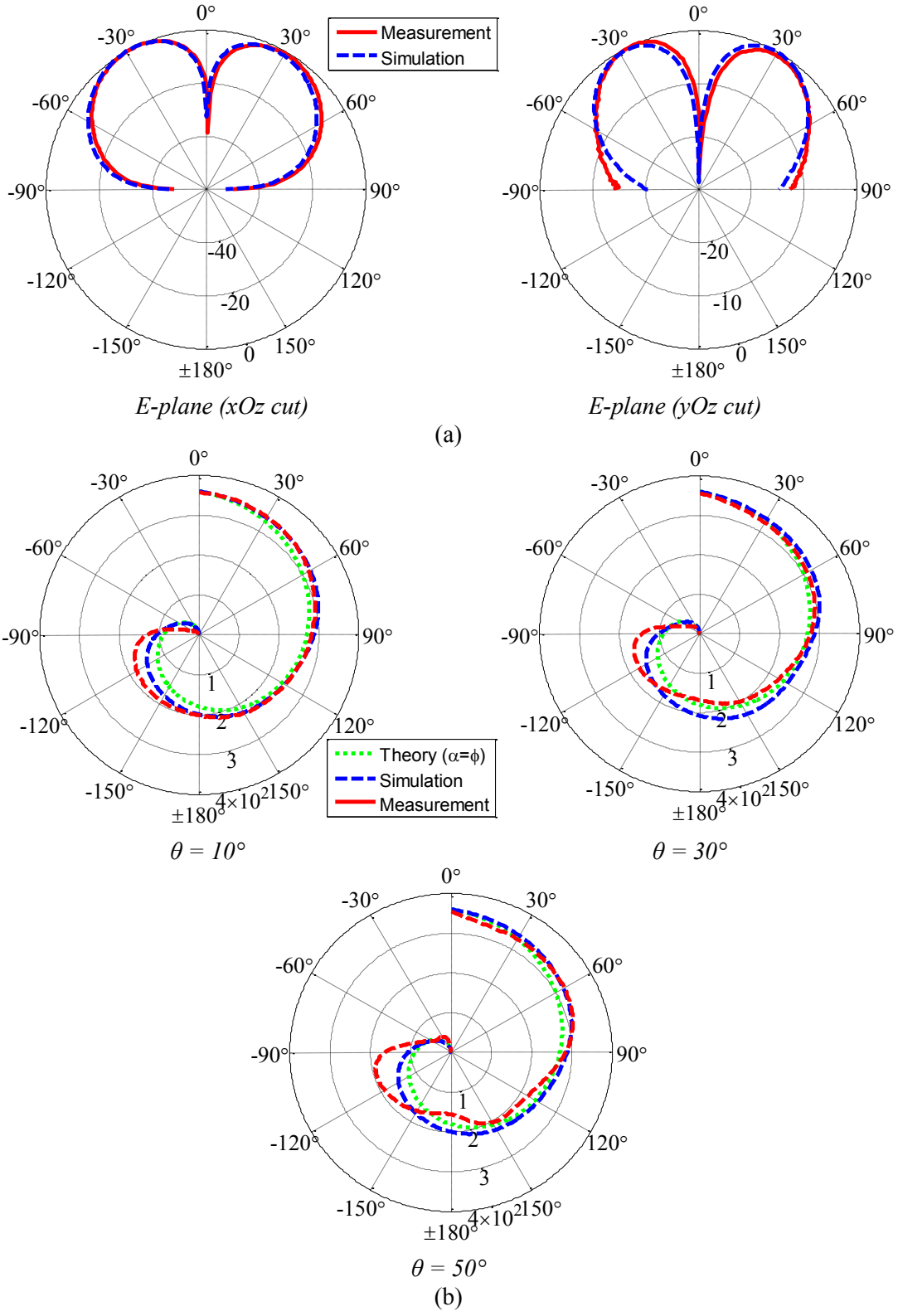

Figure II-20: Simulated and measured 2D radiation and phase patterns of the OAM antenna at 2.5GHz: (a) Normalized magnitude patterns; (b) Normalized phase patterns (in degree).

II.5 Conclusions

In this chapter we developed an antenna using four patches and an original and simple phase shifter-power divider to generate an $\ell = 1$ OAM wave at 2.5 GHz.

We firstly investigated the influences of the array parameters (number of array elements (N) and array radius (R)) on the performance of an ideal phased patch array and made the following conclusions: i) as N increases, the OAM modes become purer and of better quality, but the array becomes larger and more complex to realize; ii) $N = 4$ the smallest number of array elements that can produce the mode $\ell = 1$ with quite good quality; iii) as R increases, the OAM beam becomes more directive, but naturally some side lobes appear and the antenna geometry becomes larger.

Then, we presented the design of a practical OAM antenna which is based on a circular phase shifter-power divider and an array of 4 patches. The array radius was set at 50 mm. Appropriate weights (phase and amplitude) were obtained for the array elements. Both the 3D radiation & phase patterns and the 2D magnitude & phase patterns of the electrical field confirm the generation of an OAM bearing wave.

Finally, a prototype was realized and characterized. Good agreement is obtained between theoretical results, simulation data and measurements.

Chapter III

Design of a Directive OAM Antenna by Using Fabry-Perot Cavity

III.1 Introduction

In the previous chapter, we developed a novel antenna to generate an $\ell = 1$ OAM wave at 2.5 GHz. This OAM-wave generator is based on a 4-element circular phased array of patch antennas. It is simple, compact and easy to realize, but its directivity is relatively low. To overcome this drawback, in this chapter, we embed this OAM antenna inside a Fabry-Perot (FP) cavity to enhance its directivity. The FP cavity is composed of a ground plane, an air cavity and a partially reflecting surface (PRS).

This chapter is organized as follows. First of all, we simply analyze the model of a FP cavity and study its influences on the directivity of an antenna; then the developed OAM antenna in Chapter II is embedded inside two different FP cavities and each FP cavity is optimized for obtaining a maximum directivity of the OAM antenna; finally, a prototype is realized and characterized.

III.2 Fabry-Perot cavity

A Fabry-Perot (FP) cavity is highly frequency selective and is originally used as frequency filters in optics. In antenna applications, it is often employed as space filter to improve the antenna performances such as directivity [57-59].

III.2.1 Structure of the FP cavity

The structure of the FP cavity is shown in Figure III-1. It is generally composed of a ground plane which eliminates the back radiation, a primary source and a partially reflecting surface (PRS). The ground plane and the PRS are separated by the cavity thickness *D*. This cavity is also defined by its lateral dimension *L*. Different methods have been employed to model a FP antenna. The first approach is based on the theory of transmission lines [60], the second utilizes the dispersion diagram of a metamaterial [61], the third takes advantage of the theory of the leakage waves [62, 63], and the last utilizes the method of the Fabry-Perot interferometer which is one of the most used for extracting the antenna parameters of the FP antennas [64-67].

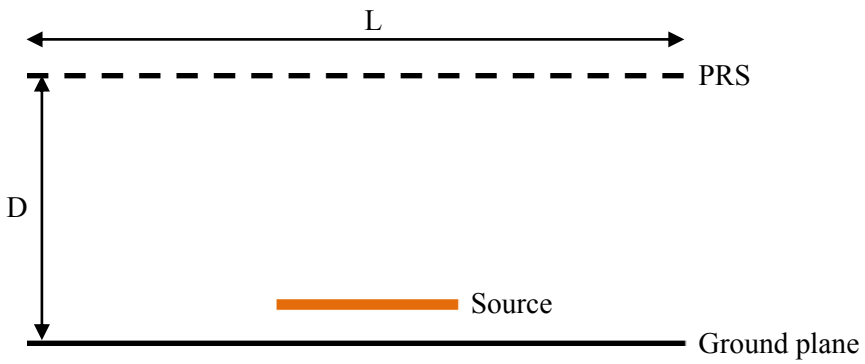

Figure III-1: Structure of the FP cavity (PRS: Partially Reflecting Surface)

III.2.2 Analysis model of the FP cavity

The analysis method based on the FP interferometer has been detailed in many papers and PhD theses. To summarize, consider the 2D FP structure consisting of a PRS and a ground plane with infinite lengths. The PRS is characterized by its reflection and transmission coefficients (r and t) and the ground plane by its reflection coefficient (r_g). Because the FP cavity has cylindrical symmetry around the z axis and has no dependencies on the azimuth coordinate φ, the φ variations are already included in these coefficients.

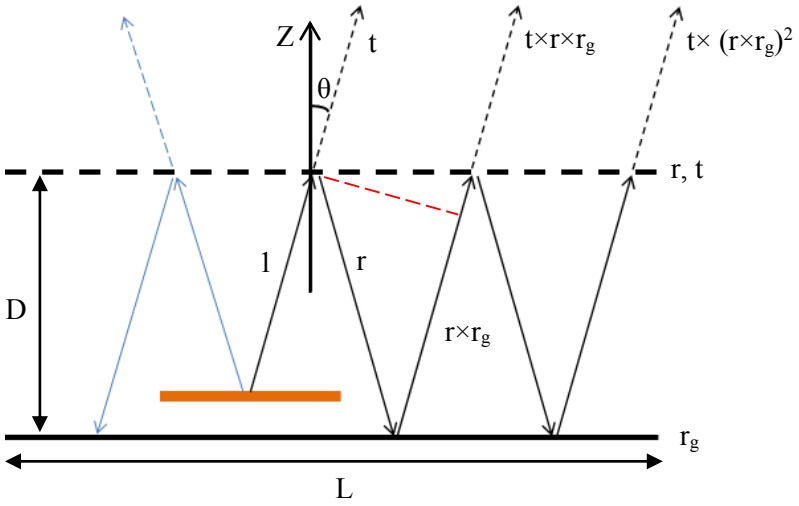

Figure III-2: Principle of the FP cavity

The PRS and the ground plane create multiple reflections within the cavity, as shown in Figure III-2. When the internal wave rays emitted by the primary source arrive at the upper PRS, they are partially reflected back to the cavity and partially transmitted out. Then, when the reflected rays arrive at the bottom ground plane, they are reflected again towards the cavity. If the amplitude of the first ray sent from the primary source is supposed to be "1", the amplitude

of the first transmitted wave is "1×t". In the same manner, the second transmitted ray has an amplitude of "t×r×r_g", because it is first reflected on the PRS, then on the ground plane and finally transmitted from PRS. The phase lag of the second ray compared to the first one is $\left(\frac{D}{cos\,\theta}+\frac{D}{\cos\theta}\times\cos 2\theta\right)\times k = 2kD\cos\theta$, where k is the propagation constant inside the cavity and θ the incidence angle between -90° and 90°. The amplitude of the nth transmitted ray is "t×(r×r_g)$^{n-1}$" and the phase lag compared to the first one is 2×(n-1)×k×D×cos(θ). The total external field of the FP cavity can be determined by the sum of all the transmitted fields, and therefore, the transmission coefficient of the FP structure is given by:

$$T_{FP} = t\left[1+\left(r\cdot r_g\right)e^{-j2kD\cos\theta}+\cdots+\left(r\cdot r_g\right)^n\left(e^{-j2kD\cos\theta}\right)^n+\cdots\right] \quad \text{(III-1)}$$

The resultant series constitute in fact a geometric series whose expression has the following simple and compact form:

$$T_{FP} = \frac{t}{1-r\cdot r_g.e^{-j2kDcos\theta}} \quad \text{(III-2)}$$

When the ground plane is a perfect electric conductor (PEC) (r_g = -1) and the phase of the PRS reflection coefficient is α, the cavity transmission coefficient can be expressed as:

$$T_{FP} = \frac{t}{1+|r|\cdot e^{j(\alpha-2kDcos\theta)}} \quad \text{(III-3)}$$

On the other hand, the cavity resonance is defined as the case where all the transmitted rays are in phase and make a constructive interference. In this case, the radiation pattern is maximum in the θ direction. According to (III-3), T_{FP} is maximum as a function of θ if its denominator is minimum. This happens if the term $|r|\cdot e^{j(\alpha-2kDcos\theta)}$ is a negative real number:

$$1+|r|\cdot e^{j(\alpha-2kDcos\theta)} = 1-|r|, \qquad \alpha-2kDcos\theta = (2n+1)\pi$$

$$D = \frac{c}{4\pi f_0\cos\theta}[\alpha+(2n+1)\pi], \quad \text{n = 0, 1, 2, 3……} \quad \text{(III-4)}$$

where c is the speed of the light inside the cavity (free space), f_0, the working frequency, n, an integer corresponding to the cavity mode number. In our study, n is set to 0 to use the first cavity mode.

The antenna directivity depends highly on α and | r |. The higher is | r |, the smaller is the denominator and the higher is the T_{FP} maximum. Moreover, | r | is highly dependent on the PRS chosen to form the cavity. In the next sections we embed the OAM antenna inside the FP cavity with the PRS made of metallic strips or tubes to enhance its directivity.

III.2.3 Influences of the dimension of the FP cavity

The cavity must have a finite dimensions to be easily realizable. Various studies have shown the influences of the lateral dimension (L) of the cavity on the antenna directivity. The

directivity increases with the lateral dimension of the cavity. However, it does not increase infinitely with the cavity surface. This means that from a certain dimension, the electric field is totally radiated and increasing the surface does not improve anymore the directivity. For small dimensions, the directivity of the FP antenna decreases significantly since part of the energy is diffracted at the edges of the cavity, which results in the occurrence of the side lobes. To limit this loss of energy, metallic walls can be added to close the cavity. We can see from Figure III-3 that it is possible to obtain a directivity higher than 18 dB for L > 5×λ without metallic walls and for L > 3×λ with metallic walls with a reflectivity of 0.96 of the PRS [68].

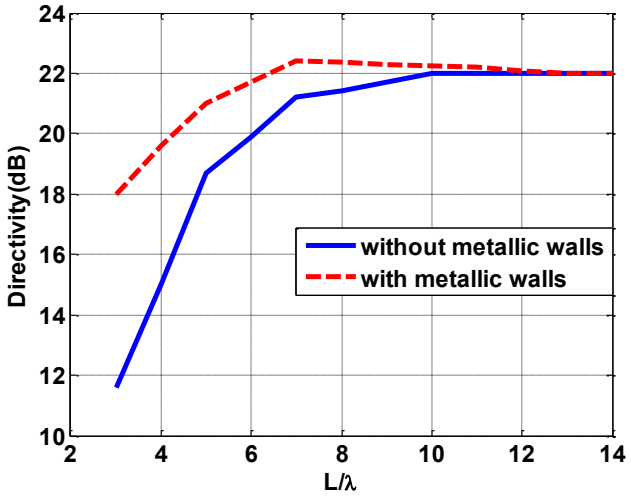

Figure III-3: Influences of the lateral dimension of the cavity on the directivity [68]

The study carried out on this problem [68] has highlighted the influences of the small lateral dimension on the resonance condition. In fact, when the lateral dimension decreases, the resonance frequency increases. Thus, we should use the following resonance conditions:

For a cuboid cavity with a square PRS, $f = \frac{c}{2}\sqrt{2 \times \left(\frac{1}{L}\right)^2 + \left(\frac{1}{D}\right)^2}$ (III-5)

where L and D are respectively the lateral dimension and the height of the cavity.

For a cylindrical cavity, $f = \frac{c}{2}\sqrt{\left(\frac{1}{r}\right)^2 + \left(\frac{1}{D}\right)^2}$ (III-6)

where r is the radius of the cavity.

Therefore, in the following study it is necessary to adjust the cavity thickness to be close to the resonance condition to maximize the directivity.

III.3 Design of the FP OAM antenna with the PRS made of metallic strips

III.3.1 Characterization of the PRS

In this part, we use a PRS made of a set of periodic metallic strips. The geometry of the PRS is shown in Figure III-4a. The strips have a width of *a* and a period of *b*, and are printed on a FR4 substrate with a thickness of 1.6 mm and a relative permittivity of 4.4. The reflection and transmission coefficients of the PRS depend on two parameters: width and period of the strips. To study the relationship between them, we simulate a unit cell of the PRS alone, as shown in Figure III-4b. The side length of the square FR4 substrate is identical to the period of the strips and a Floquet port is used to simulate an infinite PRS and to allow sending a plane wave with any desired incidence angle.

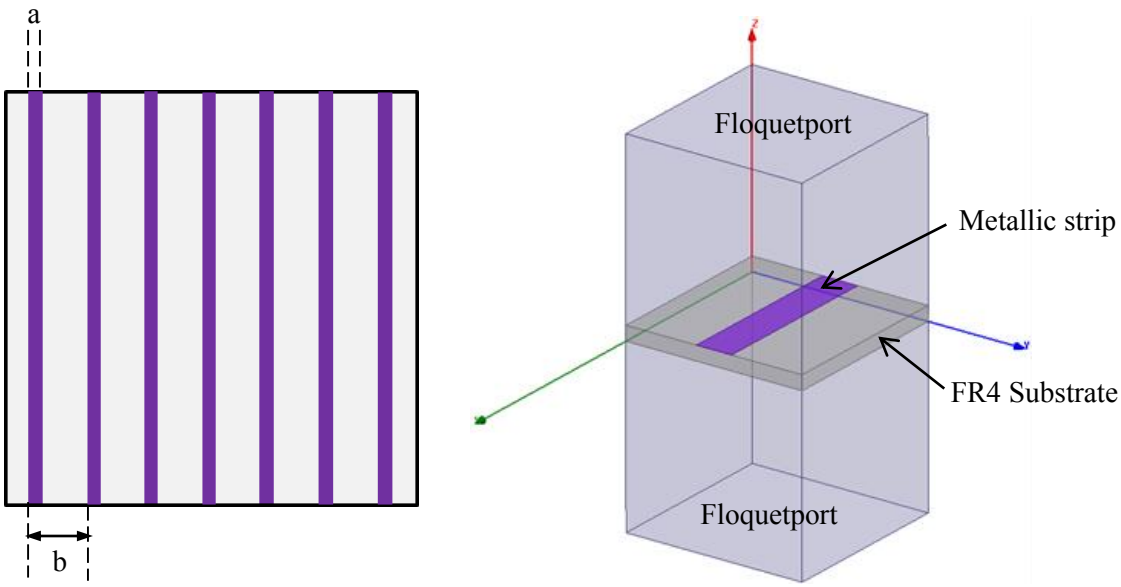

Figure III-4: (a) Geometry of the PRS made of metallic strips; (b) a unit cell of the PRS

We define the parameter τ as the filling ratio between the width and the period of the strips, i.e. $\tau = \frac{a}{b}$. The variations of the magnitude and phase of the PRS reflection coefficient depending on the normalized period (b/λ) are shown in Figure III-5 for different filling ratios at 2.5 GHz. It can be observed that for a constant filling ratio τ, as the ratio b/λ increases, the magnitude of the reflection coefficient tends to 0 (maximum transmission) and vice versa, when b/λ decreases, the magnitude tends to 1 (no transmission) and the corresponding phase tends to π. For a constant b/λ, the higher is the filling ratio, the greater is the magnitude of the reflection coefficient and the closer to π is the phase.

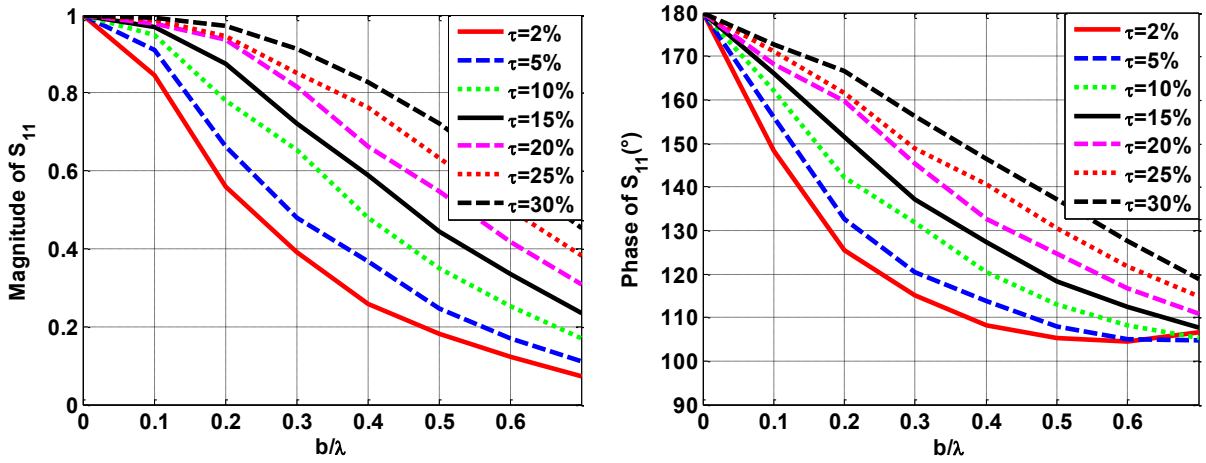

(a) (b)

Figure III-5: Reflection coefficient (S_{11}) of the PRS versus the normalized period for different filling ratios (b/λ) at 2.5 GHz: (a) Magnitude; (b) Phase.

The bandwidth is a critical parameter of the FP cavity because it depends heavily on the reflectivity of the PRS. Normally the higher is the reflectivity, the narrower is the bandwidth. Various studies have addressed this problem [69, 70]. To obtain a maximum bandwidth, the variation of the phase versus the frequency should be slowest.

In summary, to obtain a maximum directivity of a FP cavity, it is appropriate to impose a strong reflectivity at the PRS; to obtain a possibly maximum bandwidth, a slow variation of the phase of the PRS refection coefficient versus the frequency is necessary. Due to this fact, a PRS made of metallic strips with a filling ratio (b/λ) larger than 20% should satisfy these conditions [70].

III.3.2 Influences of the array radius on the directivity of the phased patch array

In the previous chapter, we have already made a detailed study on the circular phased patch array. Here we briefly show the influences of the array radius on the antenna directivity. The configuration of the OAM antenna is shown in Figure III-6. The patch array is manufactured on a FR4 substrate with a thickness of 1.6 mm and a relative permittivity of 4.4 and works at 2.5 GHz. All the patch antennas are probe fed using the same signal but with an incremental phase shift between each patch. For creating an OAM mode $\ell = 1$ with N = 4 antennas, the phase step between two neighboring elements should be $2\pi\ell/N = \pi/2$ rad = 90°.

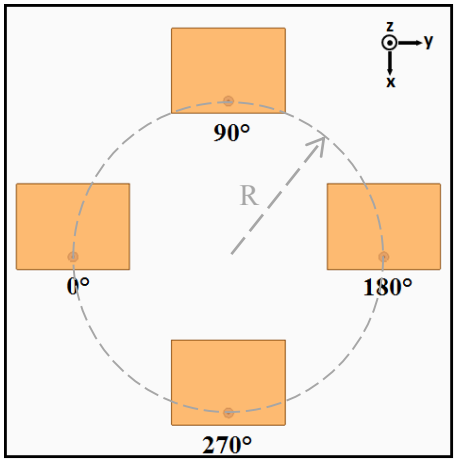

Figure III-6: Configuration of the 4-element circular phased patch array

Figure III-7 presents the E-plane radiation patterns with different array radiuses R = 50, 80 and 110 mm. It can be observed that the OAM waves become more directive as the array radius increases, but naturally some side lobes appear. When the array radius keeps increasing, the side lobe becomes even comparable with the main lobe, which means a strong loss of energy.

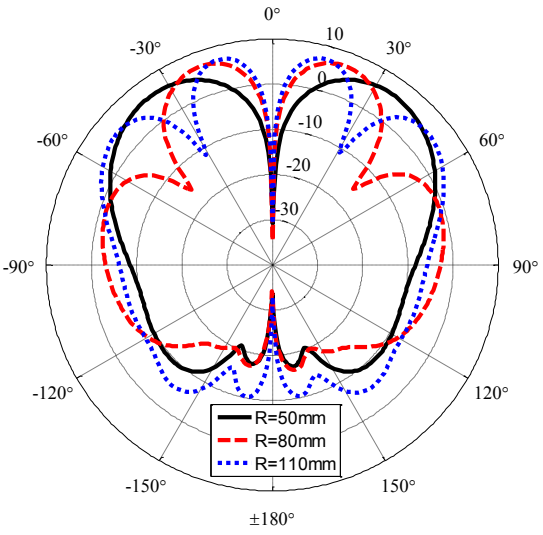

Figure III-7: E-plane radiation patterns with different array radiuses R at the frequency of 2.5 GHz

III.3.3 Optimization of the FP cavity associated with the phased patch array

It has been demonstrated that the FP cavity is able to enhance the directivity of an antenna [57-59]. Along this way, we would like to embed the above OAM antenna inside the FP cavity to enhance its directivity of the main lobe, as shown in Figure III-8. Because the OAM waves generated by the patch array are more directive with a bigger array radius, here we choose an array radius of 110 mm.

To obtain a best directivity of the OAM antenna, the width and period of the metallic strips, the cavity thickness, as well as the lateral dimension of the cavity will all be optimized.

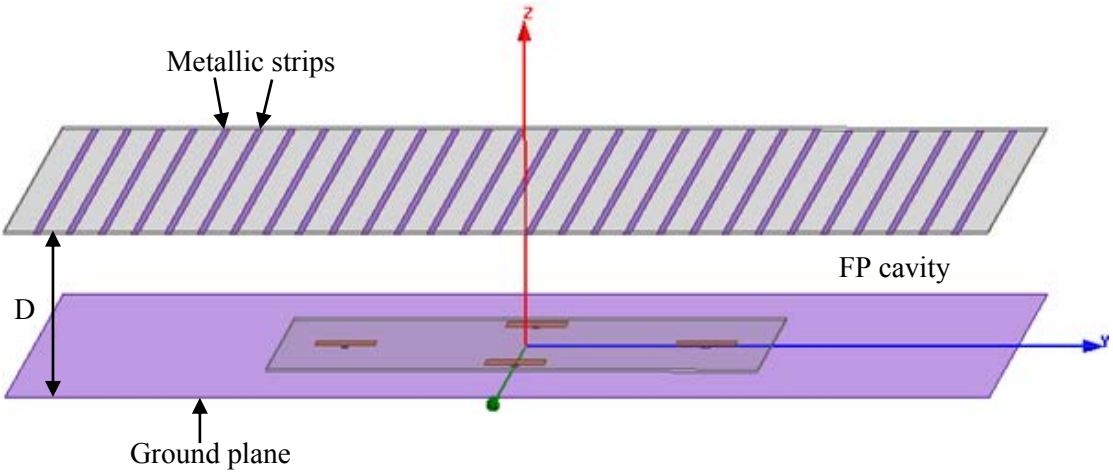

Figure III-8: Configuration of the OAM antenna inside the FP cavity

III.3.3.1 Optimization of the width and period of the strips

The optimization is divided into three steps. The first step is to optimize the width and period of the metallic strips, where the cavity aperture has a constant and big enough dimension of $5\lambda \times 5\lambda$.

The aim of this optimization is to obtain a maximum directivity of the OAM antenna by choosing a best reflectivity of the PRS. To simplify the process, we maintain the period (*b*) of the strips at 20 mm and vary the width (*a*) of the strips from 1 to 6 mm with a period of 1 mm. We simulate again a unit cell of the PRS, the resulting magnitudes and phases of the PRS reflection coefficient are shown in Table III-1. As expected, the magnitude (| r |) and phase (α) both increase with the width of the strips.

Table III–1: Magnitudes and phases of the PRS reflection coefficient and the corresponding cavity thickness for different widths of the metallic strips (period of strips: 20 mm)

Width (a) of metallic strips (mm)	Magnitude of S_{11} of PRS	Phase of S_{11} of PRS (in unit of π)	Cavity thickness (mm)
1	0.75	0.77	55
2	0.88	0.84	57.1
3	0.92	0.88	58.4
4	0.94	0.89	58.7
5	0.97	0.92	59.6
6	0.98	0.94	60.3

In addition, according to (III-4), the cavity thickness depends on the working frequency, the phase of the reflection coefficient of the PRS and the incidence angle of the wave rays. Consequently, the cavity thickness will also vary with the width of the strips. Besides, from Figure III-6 we can see that when the array radius is 110 mm, the angle value corresponds to the maximum directivity is at ±15° for the main lobe, which means the value of the incidence angle here is 15°. Thus, the initial thickness of the cavity (D) is equal to $\frac{\lambda}{4\pi\times\cos(15°)} \times (\alpha + \pi)$ for the cavity mode n = 0, where λ is the wavelength. For example, choosing a = 1 mm, the corresponding | r | and α are respectively 0.75 and 0.77π, and the calculated cavity thickness is 55 mm with λ = 120 mm. The whole results are also shown in Table III-1.We can see that the cavity thickness increases with the width of the metallic strips as well.

The variation of the E-plane maximum directivity of the OAM antenna as a function of the width of the strips is shown in Figure III-9. We can observe that the OAM antenna achieves a maximum directivity of 15.6 dB with a width of 4 mm (τ = 20% for a period of 20 mm). Usually, the directivity of the FP cavity should increase with the magnitude of the reflection coefficient of the PRS. However, in our case it is noted that the behavior is not as expected.

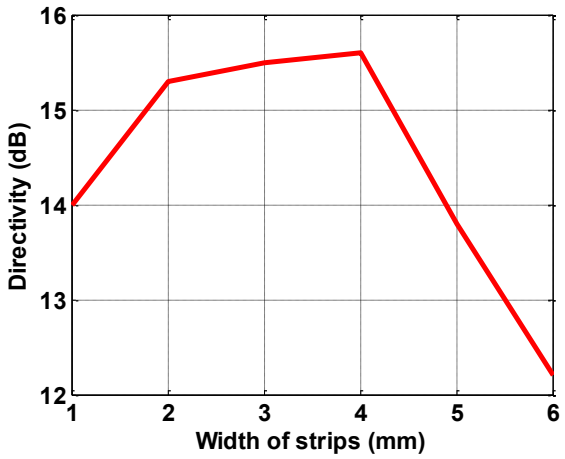

Figure III-9: Maximum directivity of the OAM antenna versus the width of the metallic strips at the frequency of 2.5 GHz (period of strips: 20 mm)

In addition, we make a comparison of the E-plane radiation patterns in Figure III-10. It can be seen that when the magnitude of the reflection coefficient of the PRS becomes big (corresponding a = 4 and 6 mm), many side lobes appear. Moreover, the side lobe level increases with the magnitude of the reflection coefficient of the PRS. This behavior may be used to explain why the directivity of the OAM antenna does not keep increasing with the

magnitude of the reflection coefficient of the PRS. Besides, due to this fact, an appropriate width of the strips is necessary to reduce the side lobe level.

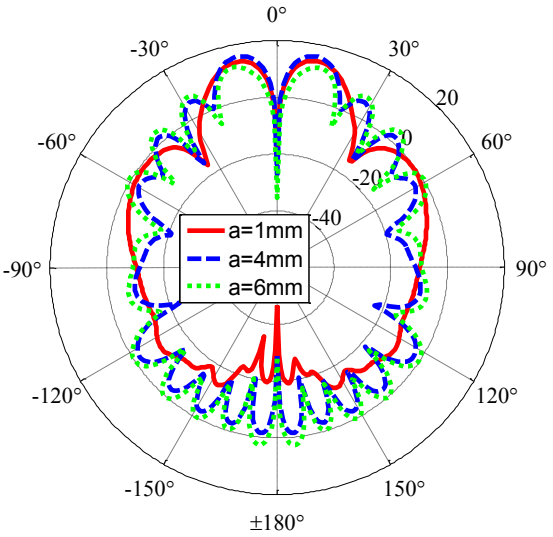

Figure III-10: E-plane radiation patterns with different widths of strips at the frequency of 2.5 GHz (period of strips: 20 mm)

In summary, to obtain a maximum directivity of the FP OAM antenna, it is suitable to impose a strong reflectivity at the PRS; on the other hand, to obtain a lower side lobe level, the reflectivity should not be too high. Based on these two points, the strips with a width of 4 mm and a period of 20 mm will be utilized.

III.3.3.2 Optimization of the cavity thickness

The second step is to optimize the thickness of the FP cavity. During this step, we maintain the width and period of the strips at 4 and 20 mm and still employ a cavity aperture with a dimension of $5\lambda \times 5\lambda$.

When the phased patch array is embedded inside the FP cavity, the angle value corresponding to the maximum directivity is at ±11° instead of ±15°, so the previously calculated cavity thickness may not be sufficiently precise. Due to this fact, we have varied the cavity thickness (D) a little to further optimize the antenna directivity, the results are shown in Table III-2. We can observe that the E-plane maximum directivity of the OAM antenna changes slightly with the cavity thickness, while the angle value corresponding to the maximum directivity maintains at 11°; the OAM antenna achieves a best directivity of 16.2 dB with a cavity thickness of 58 mm, which is the final value we have used.

Table III–2: Maximum directivity value and position of the OAM antenna for different cavity thicknesses (width of strips: 4 mm, period of strips: 20 mm)

Cavity thickness (mm)	Max directivity (dB)	Position (°)
59	15	11
58.7 (calculated value)	15.6	11
58.5	15.9	11
58	16.2	11
57.5	16	11

To better show the influences of the cavity thickness on the antenna directivity, Figure III-11 presents the E-plane radiation patterns with the calculated and optimized cavity thicknesses. We can observe that as presented above, the OAM antenna achieves a higher directivity with the optimized cavity thickness. Moreover, the side lobe level is significantly decreased at the same time, which is another advantage of this thickness.

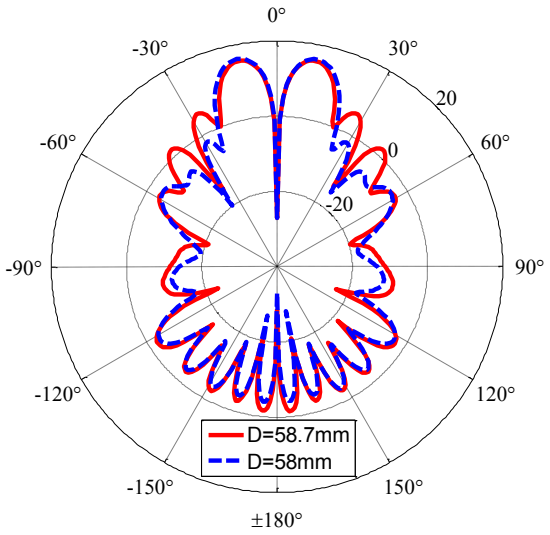

Figure III-11: E-plane radiation patterns with the calculated and optimized cavity thicknesses at the frequency of 2.5 GHz (width of strips: 4 mm, period of strips: 20 mm)

III.3.3.3 Optimization of the dimension of the cavity aperture

Finally, we optimize the dimension of the cavity aperture. The cavity thickness is kept at 58 mm and the width and period of the strips at respectively 4 and 20 mm.

We choose several dimensions of the cavity aperture. The resulting E-plane maximum directivity of the OAM antenna are shown in Table III-3. It can be seen that the antenna directivity generally increases with the dimension of the cavity aperture. On the other hand, the angle value corresponding to the maximum directivity decreases with the cavity aperture, which

means the OAM waves become more directive. This indicates that to obtain a higher directivity, it is appropriate to increase the dimension of the cavity aperture. However, the directivity does not increase infinitely as it approaches the limit of operation and a big dimension will make the cavity very difficult to realize in practice, a trade-off between the antenna directivity and the dimension of the cavity aperture is therefore necessary. Finally, we choose the cavity aperture with a dimension of 600 mm × 600 mm for obtaining an antenna directivity of 16.2 dB for the angle of 11°.

Table III–3: Maximum directivity value and position of the OAM antenna for different dimensions of the cavity aperture (width of strips: 4 mm, period of strips: 20 mm, cavity thickness: 58 mm)

Dimension of cavity aperture (mm×mm)	**Max directivity (dB)**	**Position (°)**
360 × 360	13.9	15
480 × 480	14.3	14
600 × 600	16.2	11
720 × 720	17	10

III.3.3.4 Performance of the optimized OAM antenna

According to the above optimization results, to obtain a maximum directivity of the OAM antenna at 2.5 GHz, a good condition is:

- Period of strips: 20 mm
- Width of strips: 4 mm
- Cavity thickness: 58 mm
- Cavity aperture: 600 mm × 600 mm

Figure III-12 presents the 3D radiation patterns of the patch antenna array (array radius equals to 110 mm) with and without FP cavity. We can observe a null in the center which is one of the characteristics of the OAM waves. In addition, with the use of the FP cavity, the antenna directivity is enhanced and the side lobes are significantly suppressed at the same time.

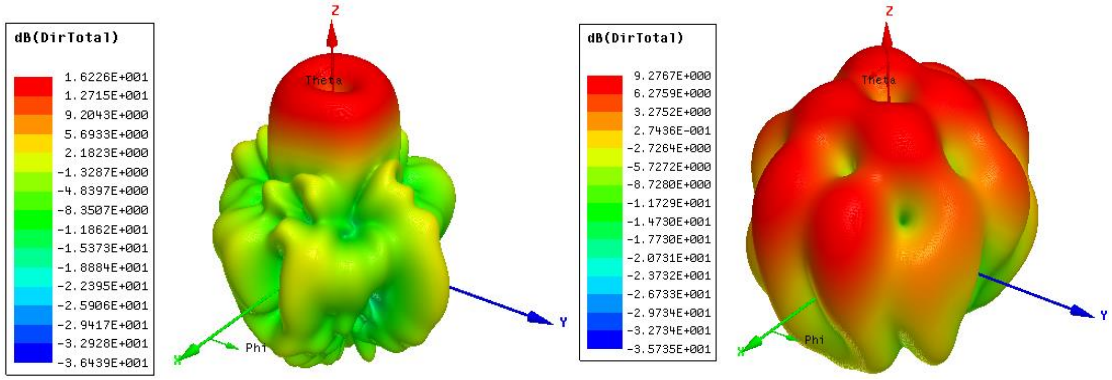

(a) (b)

Figure III-12: 3D radiation patterns of the OAM antenna (array radius equals to 110mm): (a) with FP cavity; (b) without FP cavity (width of strips: 4 mm, period of strips: 20 mm, cavity thickness: 58 mm, cavity aperture: 600 mm × 600 mm)

To give a better view of the influence of the FP cavity on the OAM antenna directivity, we make a comparison of the E-plane radiation patterns in Figure III-13. It can be seen that with the use of the FP cavity, the antenna directivity increases in E-plane, from 7 to 16.2 dB. The maximum directivity is obtained for an angle of 11°.

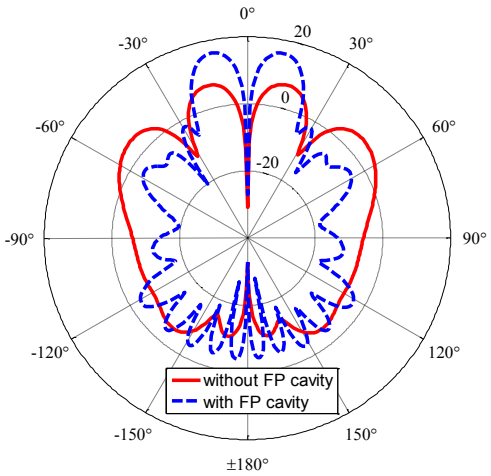

Figure III-13: Comparison of E-plane radiation patterns of the OAM antenna with and without FP cavity (array radius equals to 110mm) (width of strips: 4 mm, period of strips: 20 mm, cavity thickness: 58 mm, cavity aperture: 600 mm × 600 mm)

III.3.4 Design of the phase shifter-power divider

As what is done in the previous chapter, here we re-design the circular phase shifter-power divider with a larger array radius of 110 mm to supply the required 90° phase difference between two neighboring antennas. The combined phase shifter and power divider is manufactured on a FR4 substrate with a thickness of 1.6 mm and relative permittivity of 4.4. It

works at 2.5 GHz and has 5 ports: port1 is the input and is matched to 50 Ω, while the others are used as outputs to feed the patch antennas located on a circle. The impedance of each part of the microstrip arcs is marked in Figure III-14. HFSS software is used to optimize the length and the width of the arcs to ensure the antenna matching, a uniform amplitude at the output ports and a 90° phase shift between two successive outputs.

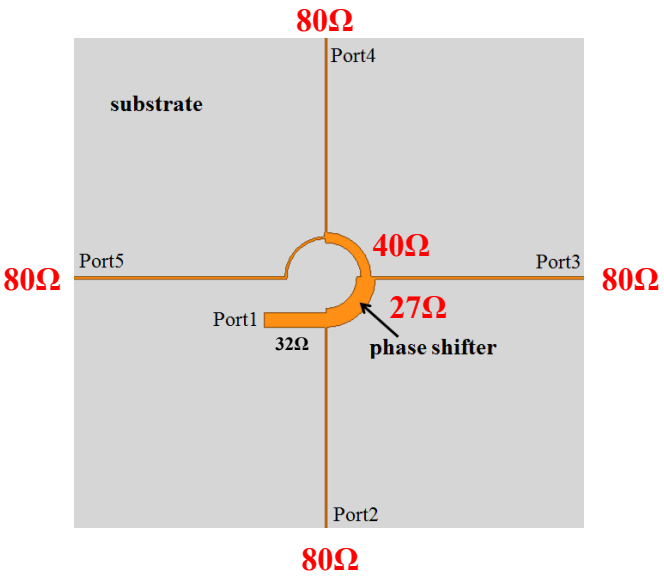

Figure III-14: Geometry of the phase shifter-power divider, feeding the four patches

The simulated results of the phase shifter-power divider are shown in Figure III-15. We can observe that at 2.5 GHz (vertical black line), the phase shifts between two neighboring ports are around 90° (max. error = ±1°) and the amplitudes of all the ports are nearly the same (max. error = ±0.6dB). Thus, the phase shifter-power divider has quite a good agreement with the required specifications.

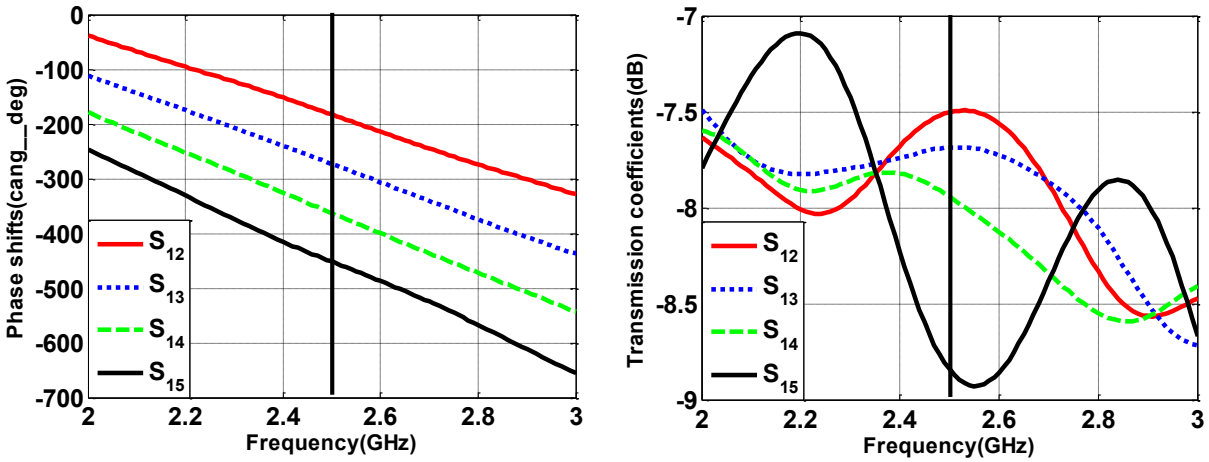

Figure III-15: Simulated parameters of the phase shifter-power divider: phase shifts (left) and transmission coefficients (right). At 2.5 GHz, the phase shifts of S_{21}, S_{31}, S_{41}, S_{51} are -182°, -273°, -363°, -452°, respectively; and the corresponding amplitudes are -7.5 dB, -7.7 dB, -7.9 dB, -8.8 dB.

III.3.5 Characterization of the FP OAM antenna with the phase shifter-power divider

The configuration of the FP OAM antenna with the phase shifter-power divider is shown in Figure III-16. The OAM antenna contains 3 FR4 substrates which all have a dimension of 300 mm × 300 mm × 1.6 mm and a relative permittivity of 4.4. The phase shifter-power divider is manufactured on the bottom substrate and the patch array on the top one. The big ground plane is between the middle and the top substrates. All the patch antennas are connected with the phase shifter-power divider through probes and fed by a 50 Ω coaxial cable from the back side of the bottom substrate. To obtain a good radiation pattern and satisfy the impedance matching, the length and width of single patch antenna are optimized at respectively 26.6 mm and 36.5 mm and the position of the feeding point is 5 mm from the bottom side of the patch antenna.

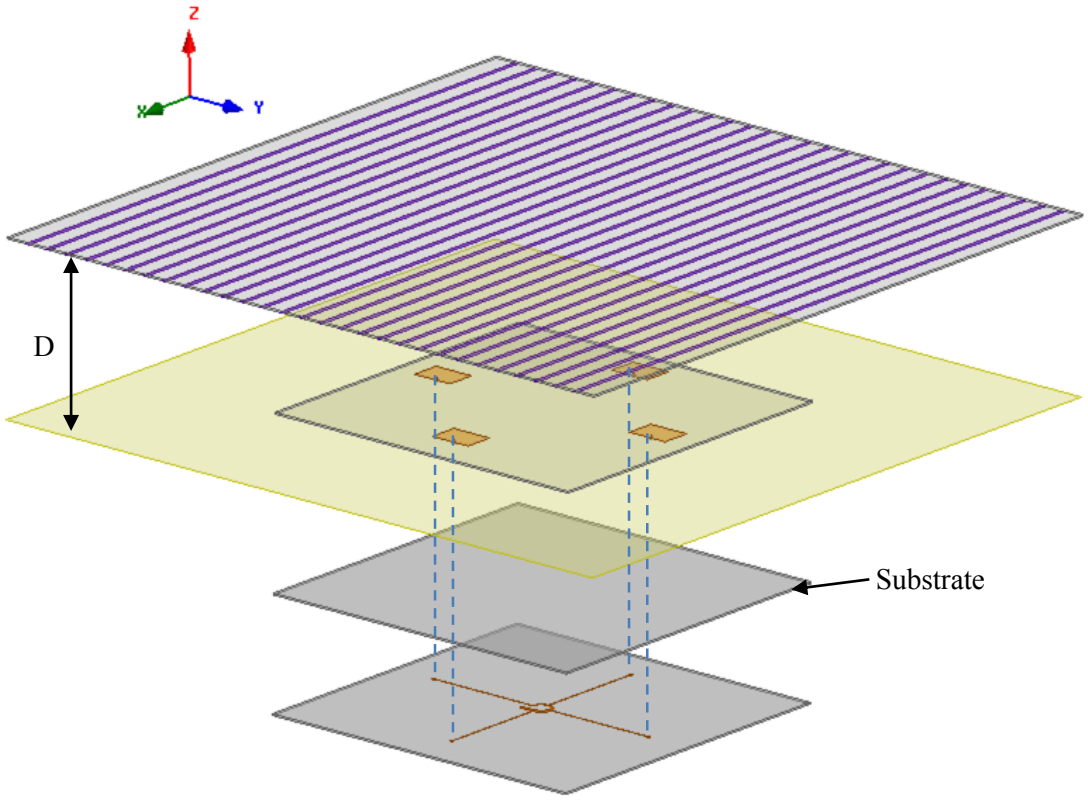

Figure III-16: Configuration of the FP OAM antenna with phase shifter-power divider

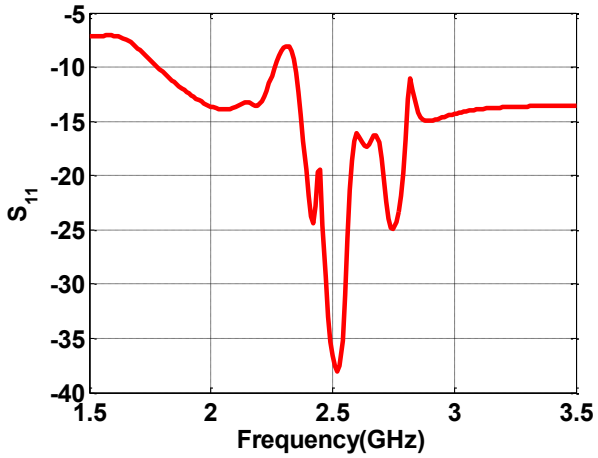

Figure III-17: Reflection coefficient of the FP OAM antenna with phase shifter-power divider

As depicted in Figure III-17, the practical FP OAM antenna is well matched around 2.5 GHz. Figure III -18 presents the 3D radiation pattern and the 2D radiation and phase patterns at 2.5 GHz. The 3D radiation pattern has a central hole that is characteristic of an OAM wave. Compared to the ideal FP OAM antenna, the maximum directivity decreases slightly by 0.2 dB. The 2D radiation patterns correspond to the xOz and yOz cuts of the 3D plot. It can be seen that the E and H planes both obtain a maximum directivity at the angle of 11°. Besides, the side lobe level of H-plane is higher than E-plane. We present the phase patterns (Figure III-18c) for three values of the spherical angle (aperture) θ: 5°, 15° and 25°. The spiral form of the phase variation versus the roll angle φ is due to the polar representation of the linear phase variation. We can observe that the phase variation in one turn is 2π and the quality of the phase pattern is good at small values of θ angle, but degrades as θ increases.

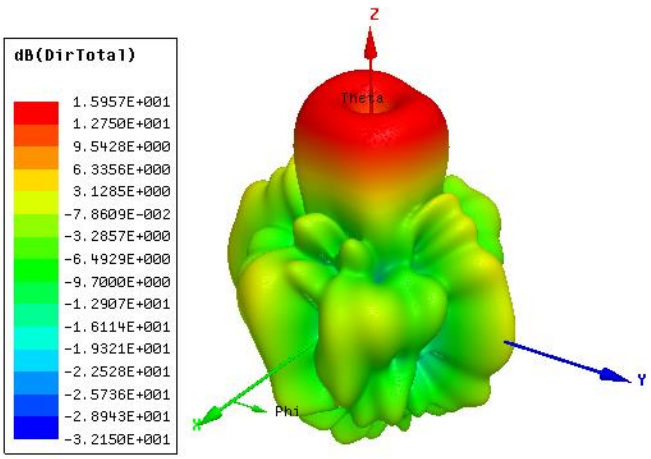

(a)

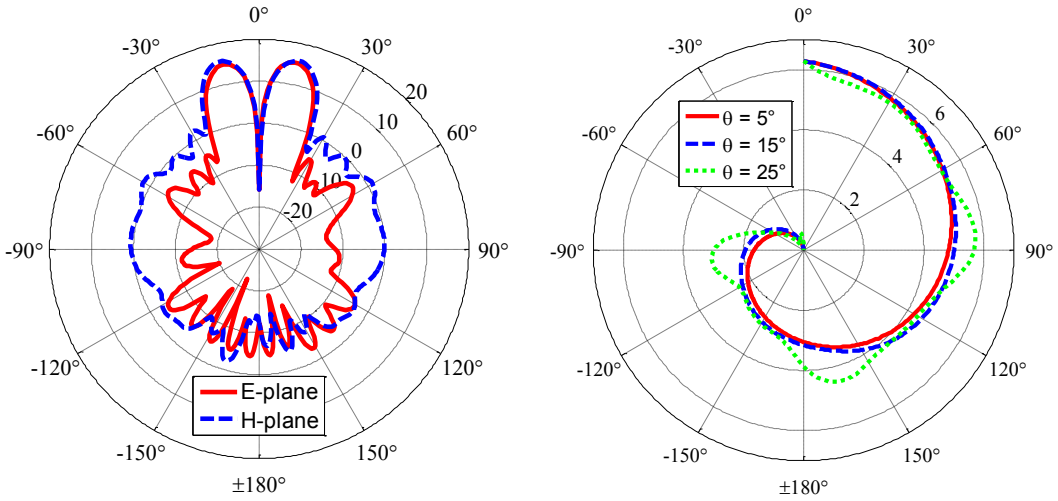

(b) (c)

Figure III-18: Radiation and phase patterns of the FP OAM antenna at 2.5 GHz: (a) 3D radiation pattern; (b) 2D radiation patterns in E and H planes; (c) Normalized phase patterns (in radians) at different θ angles

The magnitude and phase patterns of the E_x component of the propagated wave, observed on a plane perpendicular to the direction of propagation, are plotted in Figure III-19. The observation window is a circular area with a radius of 300 mm, lying 30 mm above the PRS. It can be seen that the magnitude is minimum at the center and the phase rotates around the center with a 2π phase shift in one turn. This confirms the generation of an OAM bearing wave with $\ell = 1$.

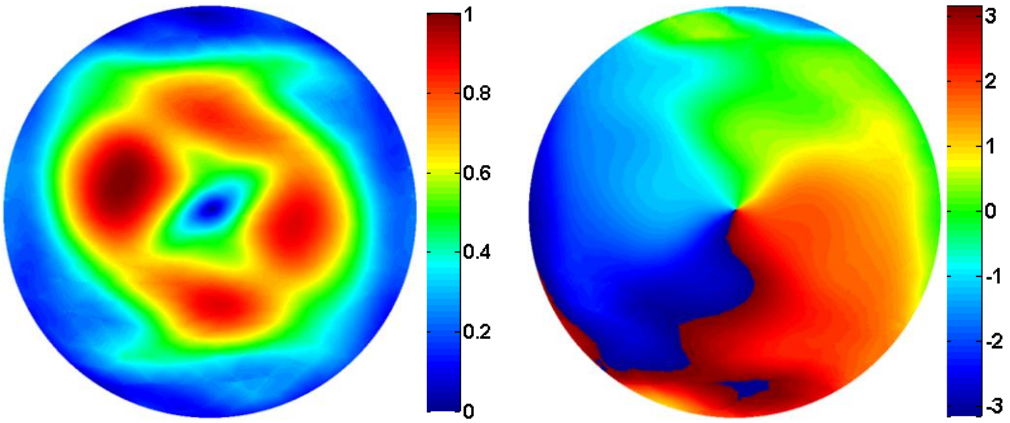

Figure III-19: Normalized magnitude (left) and phase (right) patterns of E_x component for the FP OAM antenna at 2.5 GHz (circular observation window with a radius of 300 mm, lying 30 mm above the PRS)

According to the simulation results, the directivity of the OAM antenna is significantly enhanced by using the FP cavity. However, the big dimension of the substrate makes it difficult

to realize this antenna in practice. To solve this problem, in the next part we propose another design method.

III.4 Design of the FP OAM antenna with the PRS made of metallic tubes

In this part, the metallic strips are replaced by metallic tubes. In this way, the big substrate is no more needed which makes it easier to realize the FP cavity.

III.4.1 Characterization of the PRS

The geometry of the PRS made of periodic metallic tubes is shown in Figure III-20a. The tubes have a diameter of d and a period of e. These two parameters affect the reflection and transmission coefficients of the PRS. To study the relationship between them, we simulate again a unit cell of the PRS alone, as shown in Figure III-20b. The side length of the square TEM waveguide is identical to the period of the tubes, and again a Floquet port is used to send a plane wave with any desired incidence angle.

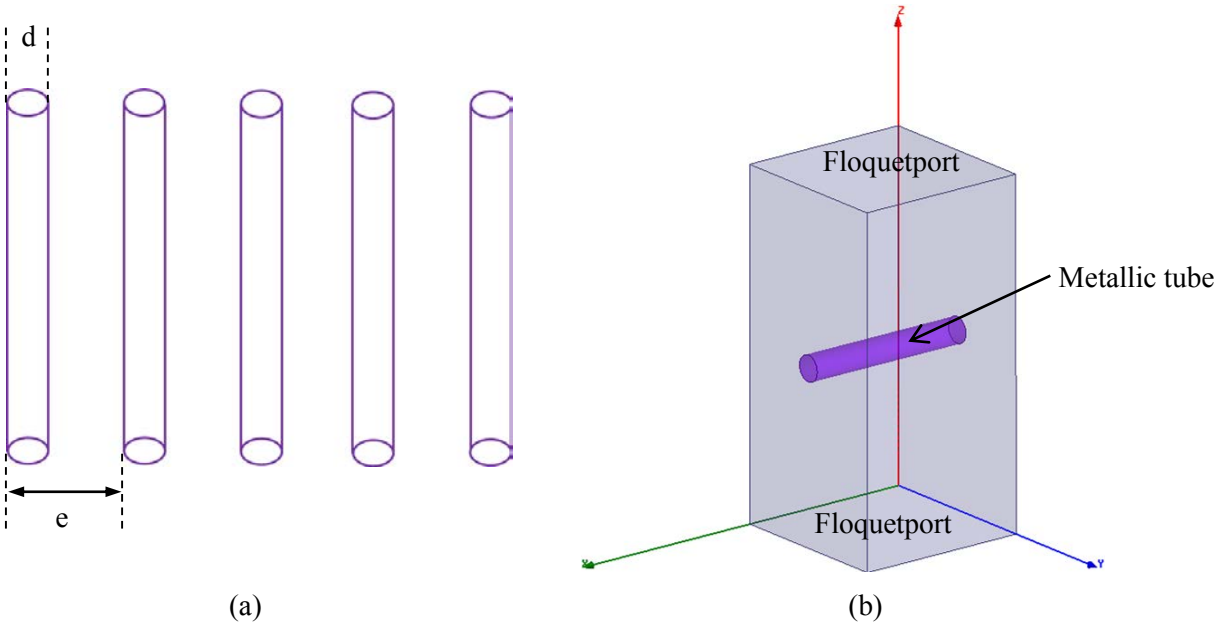

Figure III-20: (a) Geometry of the PRS made of metallic tubes; (b) a unit cell of the PRS

We define the parameter δ as the ratio between the diameter and the period of the tubes, i.e. $\delta = \frac{d}{e}$. The parameter e is normalized to the wavelength. The variations of the magnitude and phase of the PRS reflection coefficient as a function of the normalized period (e/λ) are shown in Figure III-21 for different values of δ at 2.5 GHz. It can be observed that these curves are similar to those of the PRS made of metallic strips. When δ is constant, as the ratio e/λ increases, the magnitude of the reflection coefficient tends to be 0 (maximum transmission) and

vice versa, when e/λ decreases, the magnitude tends to be 1 (no transmission) and the corresponding phase tends to be π. For a constant e/λ, the higher is δ, the bigger is the magnitude of the reflection coefficient and the closer to π is the phase.

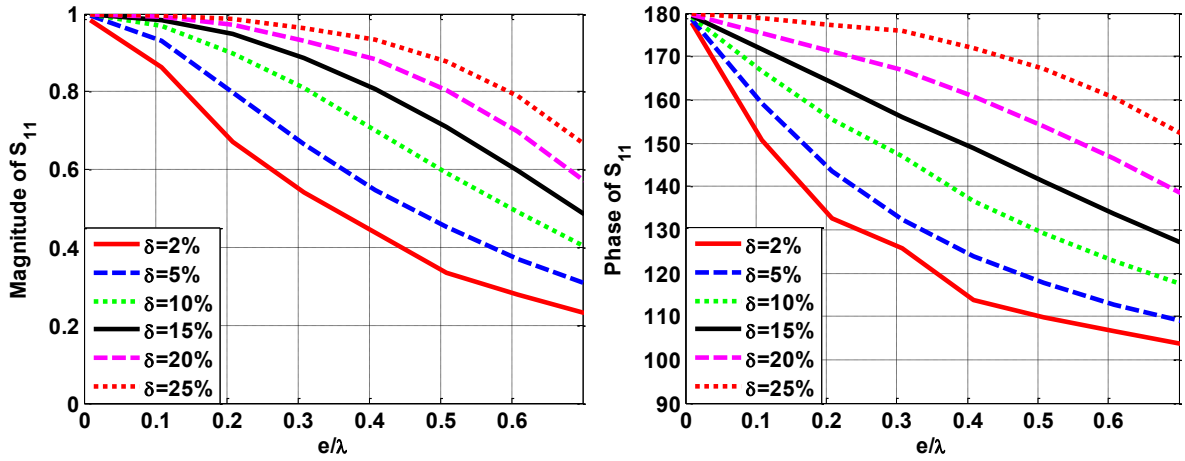

(a) (b)

Figure III-21: Reflection coefficient of the PRS versus the normalized period (e/λ) for different values of δ at 2.5 GHz: (a) Magnitude; (b) Phase.

In this new design, the diameter of the tubes is set at 4 mm. To obtain a maximum directivity of the OAM antenna, the reflection coefficient of the new PRS should be close to the previous one, i.e. the magnitude and phase of the reflection coefficient of the new PRS should be near 0.94 and 0.89π, respectively. According to the simulations, this corresponds to a period of the tubes of 26 mm.

III.4.2 Influences of different kinds of walls on the OAM antenna directivity

As shown in Figure III-22, the FP cavity is closed on the sides using 4 walls, of which two are used to support the metallic tubes. The circular patch array is still manufactured on a FR4 substrate with a thickness of 1.6 mm and a relative permittivity of 4.4 and works at 2.5 GHz. All the array elements are probe fed using the same signal but with a 90° phase shift between each element. Again the array radius is set at 110 mm and the cavity aperture has a dimension of 600 mm × 600 mm. To obtain an optimal directivity of the OAM antenna, in this section the influences of different kinds of walls on the antenna directivity will be investigated.

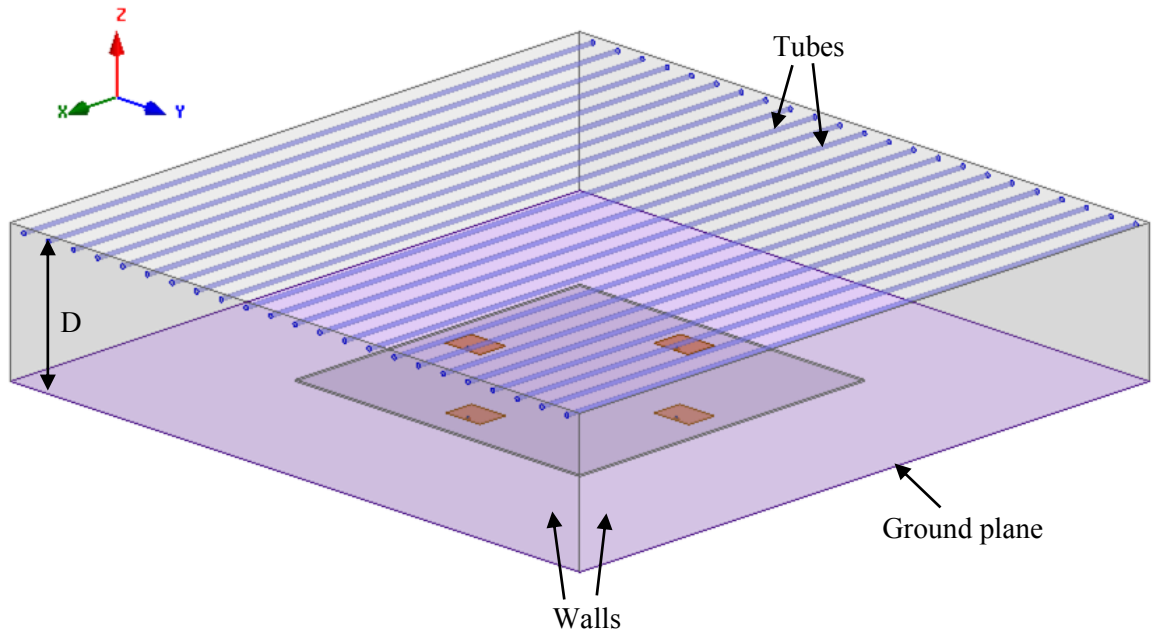

Figure III-22: Configuration of the ideal model of the second FP OAM antenna with the PRS made of metallic tubes

III.4.2.1 4 PVC walls

Because the plastic wall is lighter, which makes it a good choice for realization, we firstly use 4 PVC walls with a thickness (*T*) of 15 mm to close the FP cavity. According to the optimized results of the previous FP OAM antenna, the cavity thickness for obtaining a best directivity is 58 mm. We have varied the cavity thickness to validate this for the new antenna, the results are shown in Table III-4. It can be seen that the variation of the directivity as a function of the cavity thickness is in good agreement with that of the previous antenna. The new structure achieves a best directivity of 16.3 dB for the angle of 10° with a cavity thickness of 58 mm.

Table III–4: Maximum directivity value and position of the OAM antenna for different cavity thicknesses (D)

Cavity thickness (mm)	Max directivity (dB)	Position (°)
58.5	15.5	10
58	16.3	10
57.5	15.8	10

To show the influences of the PVC walls on the antenna directivity, we make a comparison of the E and H plane radiation patterns for three different cases: no PVC walls (i.e. T = 0), T = 5 mm and T = 15 mm in Figure III-23. It can be seen that both E and H planes obtain

a maximum directivity for the angle of 10°, and the H-plane has a higher side lobe level than E-plane. Besides, as the thickness of the PVC wall increases, the side lobe level becomes higher in E-plane, but remains almost the same in H-plane. Therefore, it is appropriate to use the PVC wall with a small enough thickness to obtain a low side lobe level of the E-plane. However, to decrease the side lobe level of H-plane, a new material of the wall is needed.

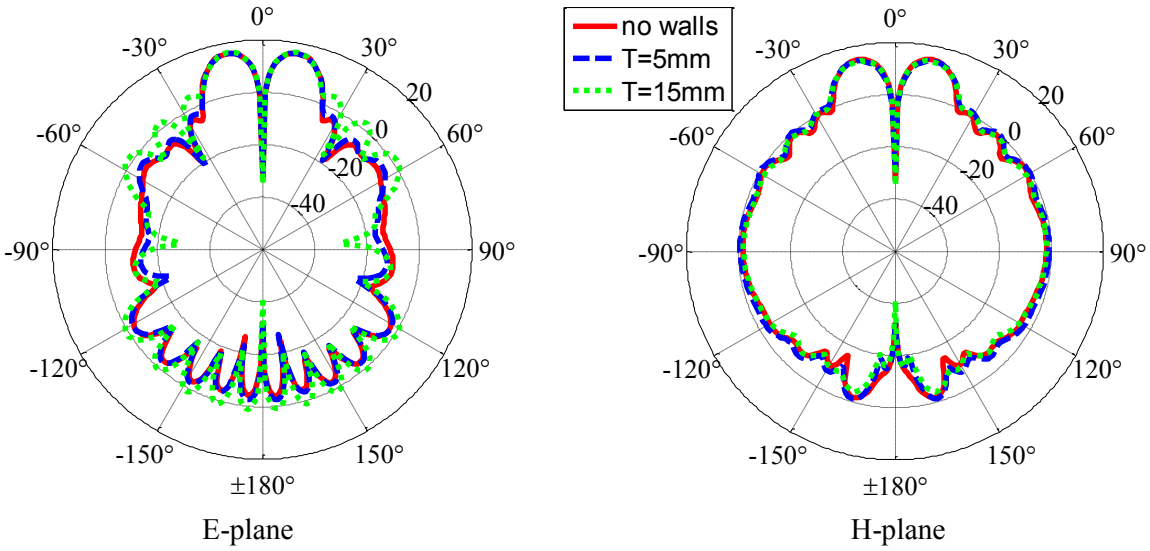

Figure III-23: Comparison of E and H plane radiation patterns of the FP OAM antenna for three different cases: no walls, 5-mm-thick wall and 15-mm-thick wall

III.4.2.2 4 PEC walls

Because the performance of the FP cavity closed by 4 PVC walls is not satisfactory, here we use 4 ideal metal walls (PEC) which have a zero thickness to close the FP cavity. Figure III-24 presents the E and H plane radiation patterns of the FP OAM antenna with PEC or 5-mm-thick PVC walls. It can be seen that by replacing the PVC walls with PEC ones, the side lobe level is significantly decreased in H-plane, but becomes worse in E-plane. Therefore, a good choice should be to keep the PVC walls in H-plane and use only the PEC walls in E-plane.

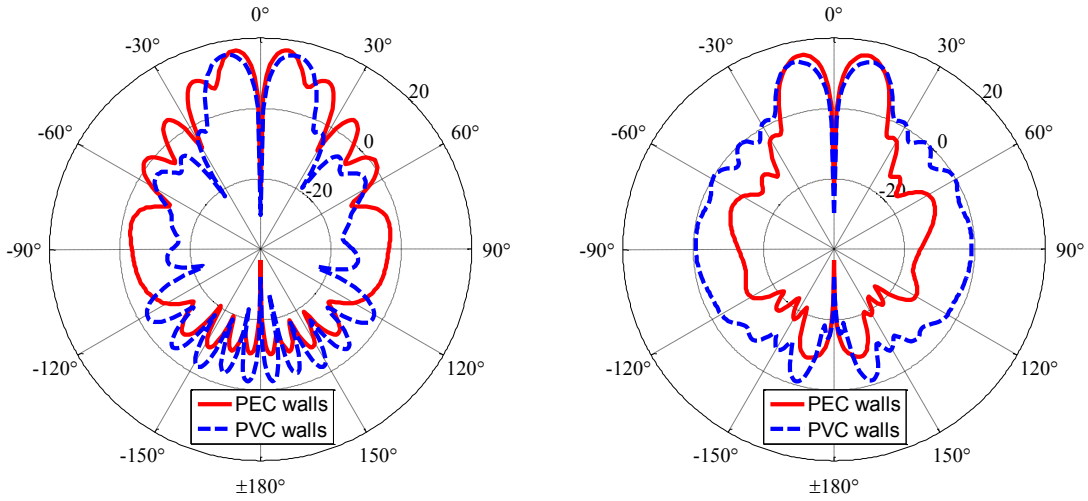

Figure III-24: E and H plane radiation patterns of the FP OAM antenna with PEC and 5-mm-thick PVC walls

III.4.2.3 2 PEC and 2 PVC walls

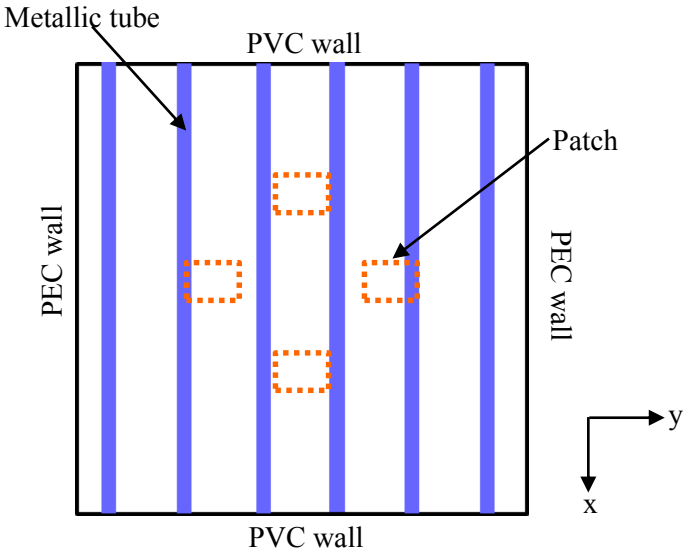

Figure III-25: Top view of the FP cavity for showing the material of the walls

Based on the above analysis, the FP cavity is finally closed by 2 PEC walls in E-plane and 2 PVC walls in H-plane, as shown in Figure III-25. The PVC walls are necessary for supporting the metallic tubes in the process of realization. As shown in section III.4.2.1, to decrease the E-plane side lobe level, the thickness of the PVC wall should be as small as possible. However, the thickness should also enable the PVC walls to assemble well with the

PEC walls and the ground plane in practice. To meet the two requirements, we choose a thickness of 6 mm.

Figure III-26 presents the E and H plane radiation patterns of FP OAM antenna with 2 PEC walls in E-plane and 2 PVC walls in H-plane. We can observe that for both E and H planes, the side lobe level is low enough compared to the main lobe. Therefore, the results are good enough.

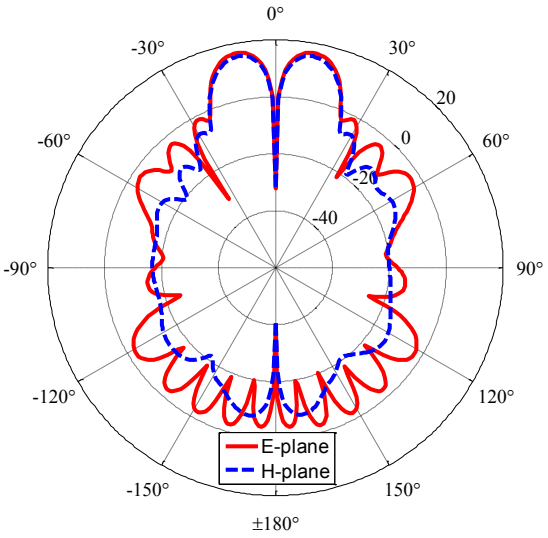

Figure III-26: E and H plane radiation patterns of the FP OAM antenna with 2 PEC walls in E-plane and 2 PVC walls in H-plane

III.4.3 Characterization of the FP OAM antenna with the phase shifter-power divider

III.4.3.1 Simulation model

The configuration of the practical design of the second FP OAM antenna is shown in Figure III-27. The structure of the OAM antenna itself is the same as the previous one. The patch array is connected with the same phase shifter-power divider to obtain a 90° phase difference between two neighboring elements and a uniform amplitude for all the elements. The main difference between the two FP antennas is the PRS that makes up the FP cavity. For the first one, it is made of metallic strips which are printed on a FR4 substrate; for the latter one, it is made of metallic tubes. Besides, to the purpose of realization, the latter FP cavity is closed by 2 PEC walls in E-plane and 2 PVC walls in H-plane.

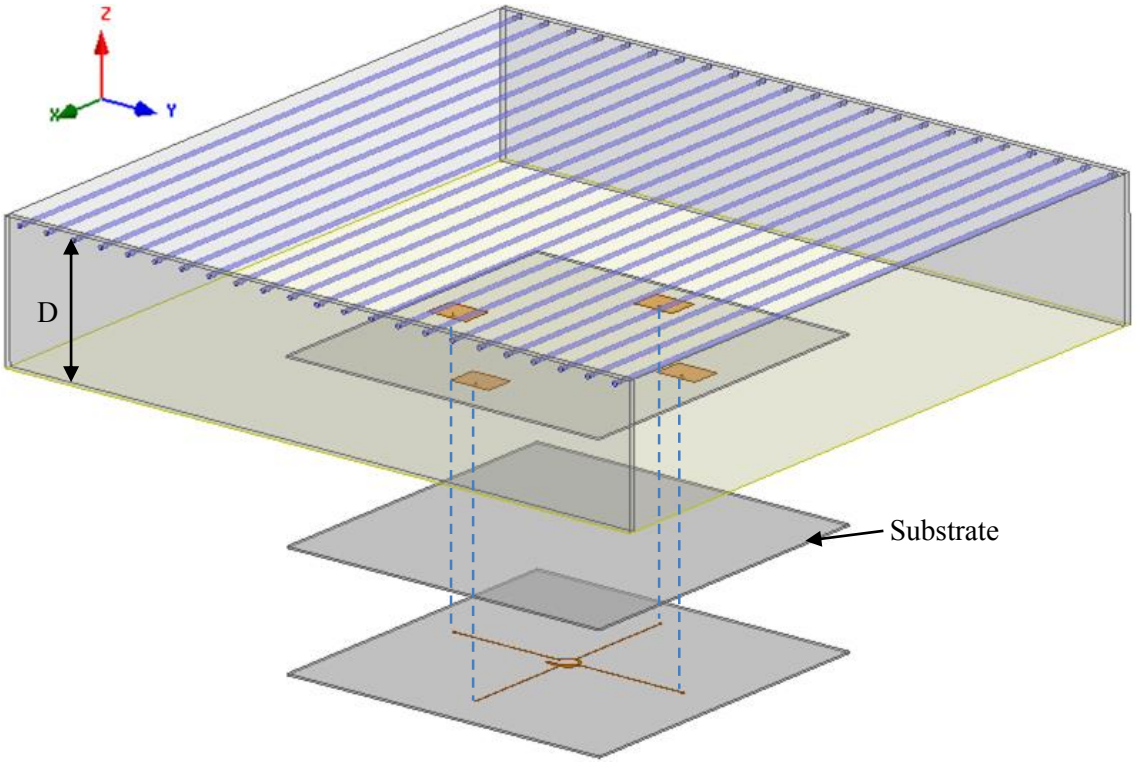

Figure III-27: Configuration of the practical design of the second FP OAM antenna

To obtain a good radiation pattern and satisfy the impedance matching, the length and width of single patch antenna are optimized at respectively 26.5 mm and 36.5 mm and the position of the feeding point is 7.4 mm from the bottom side of the patch antenna.

Figure III-28 shows the 3D radiation pattern of the FP OAM antenna at 2.5 GHz. We can observe a null in the center that is characteristic of OAM waves. The magnitude and phase patterns of the E_x component of the propagated wave, plotted on a circular area with a radius of 300 mm, lying 30 mm above the PRS, are presented in Figure III-29. It can be seen that the magnitude at the center is much smaller than the surroundings and the phase rotates around the center with a 2π phase shift in one turn. This shows indeed that both the amplitude and the phase correspond to an OAM bearing wave with $\ell = 1$.

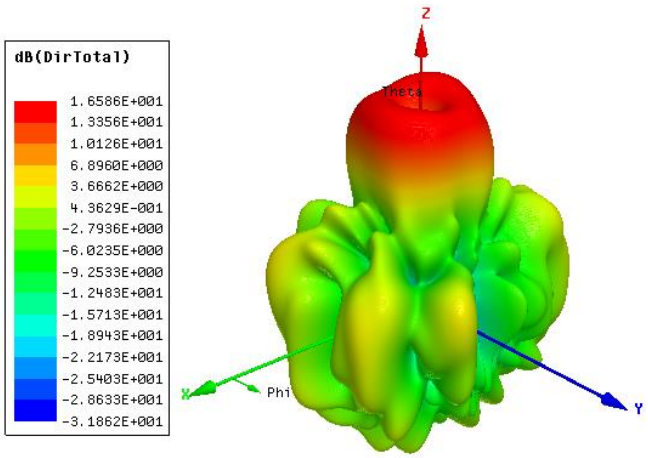

Figure III-28: Simulated 3D radiation pattern of the second FP OAM antenna at 2.5 GHz

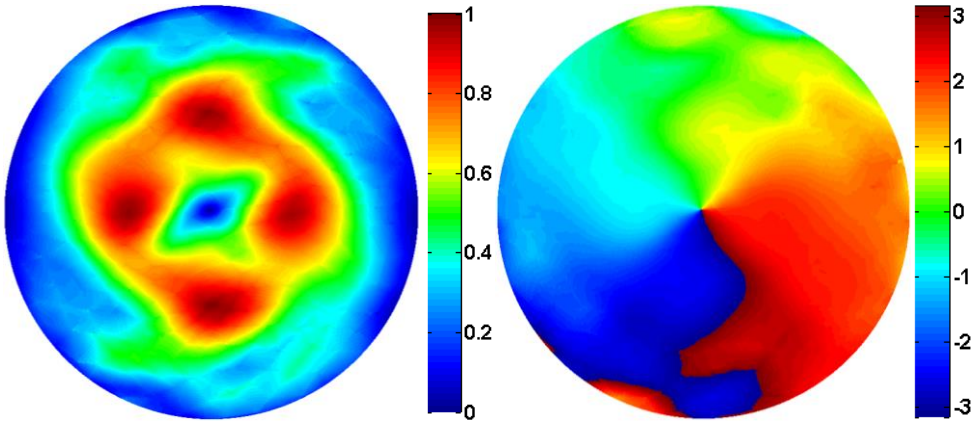

Figure III-29: Normalized magnitude (left) and phase (right) patterns of E_x component for the second FP OAM antenna at 2.5 GHz, plotted on a circular area with a radius of 300 mm, lying 30 mm above the PRS

III.4.3.2 Realized prototype

Due to the technical problem, we are not able to realize the FP OAM antenna with an array radius of 110 mm, we only realize the antenna with a small radius of 60 mm to validate the simulation results. Before the realization, we firstly make a comparison of the E-plane radiation patterns of the FP OAM antenna with different array radiuses, as shown in Figure III-30. It can be seen that with a radius of 60 mm, the antenna directivity decreases in E-plane, from 16.6 to 14.8 dB, while the maximum directivity is still obtained for an angle of 11°.

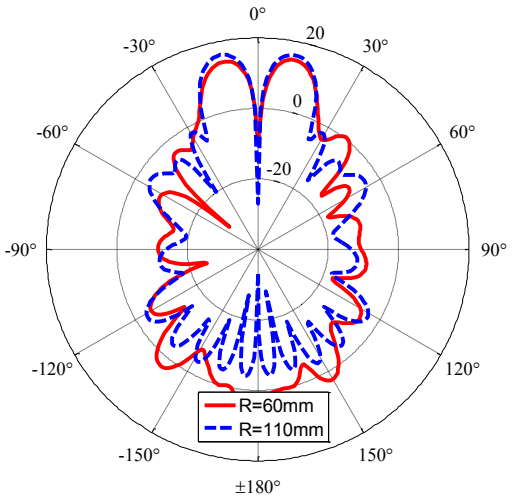

Figure III-30: Comparison of E-plane radiation patterns of the FP OAM antenna with different array radiuses

The realized prototype of the FP OAM antenna is shown in Figure III-31. The measurements are performed in an anechoic chamber.

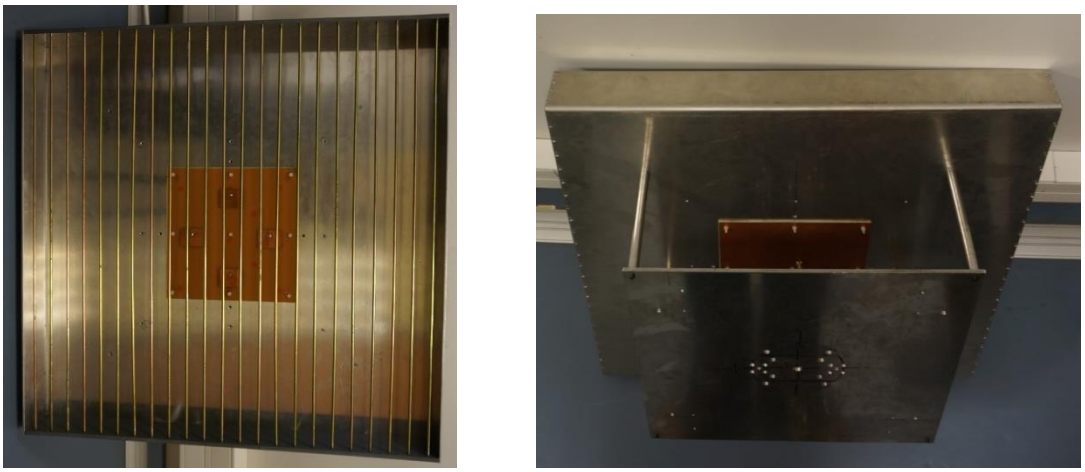

Figure III-31: Realized prototype of the FP OAM antenna (array radius equals to 60 mm): (a) Front view; (b) Back view.

As depicted in Figure III-32, the antenna is well matched around 2.5 GHz in the simulation. However, the well matched frequency range shifts up by about 40 MHz in the measurement. This may be caused by the holes drilled on the substrate for assembling. Figure III-33 presents the measured 3D radiation pattern of the FP OAM antenna. To see the central hole more clearly, it is mapped onto a plane. We have checked the patterns for different frequencies and found that the best result is obtained at 2.54 GHz. It can be seen that the OAM waves generated by the realized prototype are very directive, and the maximum directivity is obtained for the angle of 11°, which is in a good agreement with the simulation results.

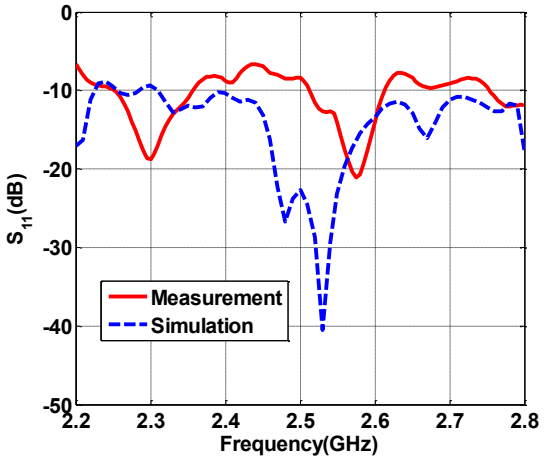

Figure III-32: Simulated and measured return losses of the FP OAM antenna (array radius equals to 60 mm)

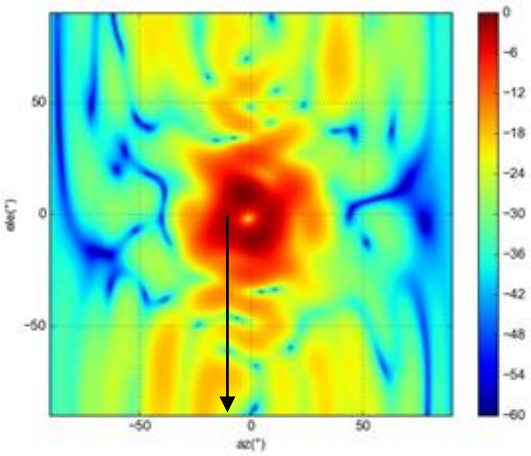

Figure III-33: Measured 3D radiation pattern of the FP OAM antenna at 2.54 GHz (array radius equals to 60 mm)

III.5 Conclusions

In this chapter we presented a method to enhance the directivity of an OAM antenna by embedding it inside a FP cavity. This OAM antenna is based on a 4-element circular phased patch array with an array radius of 110 mm and works at 2.5 GHz.

We used the FP cavity with two different PRS. The first one is made of a set of periodic metallic strips printed on a FR4 substrate, and the second, made of metallic tubes. We chose the strips with a width of 4 mm and the tubes with a diameter of 4 mm. The influences of the parameters of the FP cavity on the antenna directivity were studied. To obtain a maximum directivity, the periods of the strips and the tubes were optimized at 20 and 26 mm, the cavity thickness at 58 mm and the dimension of the cavity aperture at 600 mm × 600 mm. In addition, the second PRS is closed on the sides using 4 walls: 2 PVC walls in H-plane for supporting the

tubes and 2 PEC walls in E-plane for mechanical balance and decreasing the side lobe level of the radiation pattern. The FP OAM antenna finally achieved a directivity of 16.2 dB with an enhancement of 9.2 dB compared to the phased patch array alone.

A circular phase shifter-power divider was used to supply the required phases and amplitudes for the array elements. The design procedure and the simulation data of the two practical FP OAM antennas were given, as well as the measurements of the second antenna.

Chapter IV

Generation of Radio OAM Waves with Circular Metallic Waveguide

IV.1 Introduction

In the previous chapters, the OAM waves are generated by a circular phased array of patch antennas. An ideal circular array is flexible to generate different OAM modes, but with a low directivity. To improve this, we have embedded it inside a Fabry-Perot cavity. However, with the use of FP cavity, the overall dimension of the system is increased, which makes the antenna difficult to realize.

In this chapter, we present a new and simple way to create middle directivity OAM antenna using a horn structure. The OAM waves are generated by two main methods: i) transformation of the guided modes of a circular waveguide with a spiral phase plate (SPP); ii) combination of the guided modes. For the first method, we present three structures based on TE_{11}, TM_{01} and TE_{21} modes; for the second one, the OAM waves are created either by combing the two kinds of TE_{21} modes or TM_{01} with the1st kind of TE_{21} modes.

This chapter is organized as follows. Firstly, we simply introduce the structure of a circular waveguide; then, we present the first method to generate OAM waves; finally, we present the second method to generate OAM waves.

IV.2 Circular waveguide

A waveguide is a structure that guides waves. At radio frequencies, it is usually a hollow metallic pipe. It allows the EM waves to pass through its interior, and its metallic walls provide excellent shielding between the exterior and interior. It is often utilized in conjunction with a horn antenna to transmit the EM waves to the free space. Although a waveguide may assume any arbitrary but uniform cross section, common waveguides are either rectangular or circular. Some examples of waveguides are shown in Figure IV-1. In this chapter we use the modes of a circular waveguide to create an OAM mode of $\ell = 1$, so only the circular waveguide will be considered.

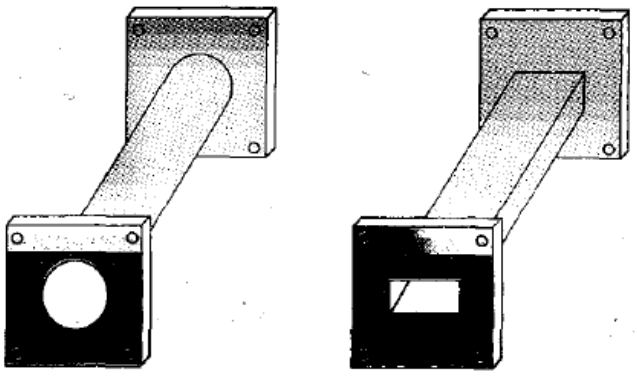

Circular Rectangular

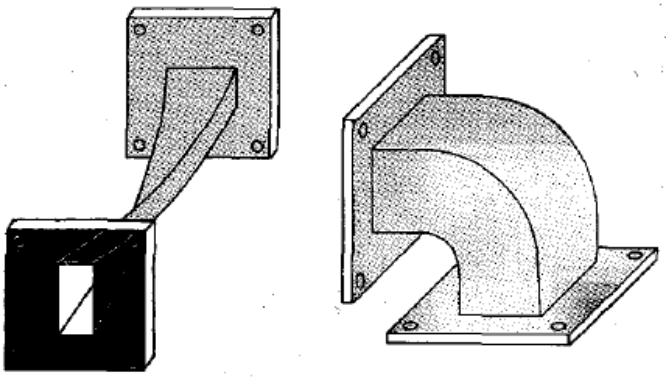

Twist 90° elbow

Figure IV-1: Some examples of waveguides [71]

The circular waveguide is occasionally used as an alternative to the rectangular waveguide. Its round cross section makes it easy to machine, and it is often used to feed the conical horns. Like other waveguides, a circular waveguide can support both transverse electric (TE) and transverse magnetic (TM) modes. These modes have a cut-off frequency, below which the EM energy is severely attenuated. The equation for calculating the cut-off frequency f_c of a circular metallic waveguide can be easily found in a waveguide handbook, and it is expressed as following [72]:

$$f_c = \frac{c\eta}{2\pi r} \tag{IV-1}$$

where c is the speed of light in free space, η a constant depending on the guided mode, and r the radius of the waveguide.

For a circular waveguide, the first three modes are TE_{11}, TM_{01} and TE_{21} modes, and the corresponding values of η are respectively 1.841, 2.405 and 3.054. Therefore, when the diameter of the waveguide is set as 4.4 cm (the value used in the next part), the calculated cut-off frequencies of these three modes are 4, 5.2 and 6.6 GHz. Figure IV-2 presents the simulated propagation constants versus frequency for the first three modes of a circular waveguide. We can see that the simulated cut-off frequencies, where the propagation constant becomes 0, have a good agreement with the theoretical values.

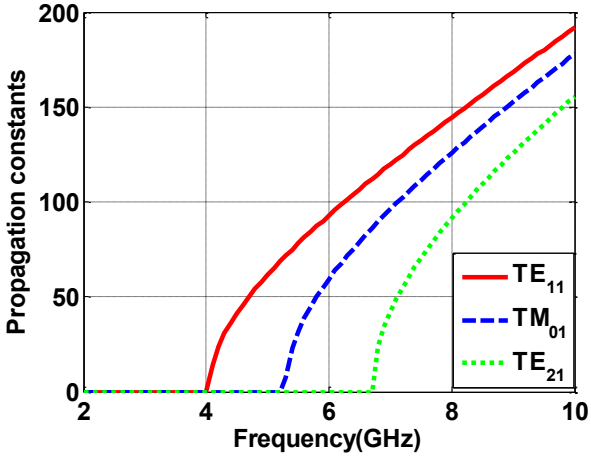

Figure IV-2: Simulated propagation constants versus frequency for the first three modes (TE_{11}, TM_{01} and TE_{21} modes) of a circular waveguide with a diameter of 4.4 cm

IV.3 Generation of OAM waves by using spiral phase plate

In the first chapter, we mentioned that a Spiral Phase Plate (SPP) is able to transform a plane wave to a wave bearing an OAM topical charge, and it has already been used in both optical and radio domains. However, the technique of SPP is usually used to generate OAM waves in free space, it is rarely used in the waveguide except in [73]. In this part, we present three original methods to generate the OAM mode in a waveguide by combining the classical modes of a circular waveguide with the SPP. The first one is based on TE_{11} mode, the second one on TM_{01} mode, and the last one on TE_{21} mode.

IV.3.1 TE_{11} mode and a single SPP

IV.3.1.1 SPP in waveguide

The first structure to generate OAM wave is presented in Figure IV-3. The SPP is made of Teflon ($\varepsilon_r \approx 2.1$) and is placed inside the waveguide with the same diameter. The height step h of the SPP has been chosen to generate an OAM mode $\ell = 1$. The TE_{11} mode is excited ideally by a waveport in HFSS software. The E-field is polarized along x axis. The other end of the waveguide is covered by a Perfectly Matched Layer (PML) to make sure that the reflected wave is totally vanished.

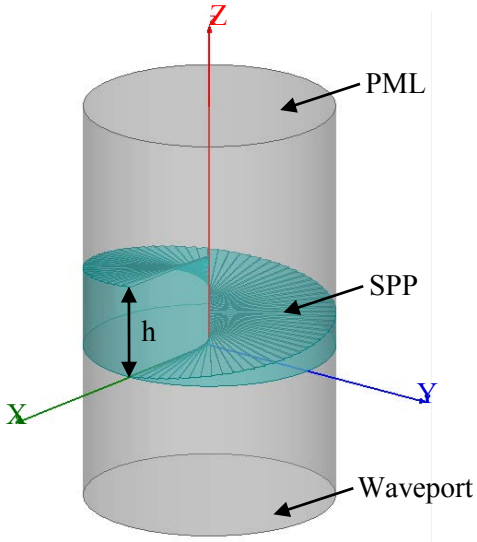

Figure IV-3: Geometry of the waveguide for generating OAM wave, using TE_{11} mode with a single SPP (Spiral Phase Plate) (PML: Perfectly Matched Layer)

The field distribution of the TE_{11} mode is shown in Figure IV-4a, and the corresponding magnitude and phase patterns of the E_x component in Figure IV-4b and Figure IV-4c. One can see that the magnitude of the electrical field of the TE_{11} mode is very strong at the center, while it should be null or very weak for the OAM wave (due to the field vortex or singularity, created by the linear variation of the phase on the wavefront). Hence, the main difficulty to generate OAM wave from the TE_{11} mode is to shape the magnitude and phase diagrams of the electrical field. It can be seen from the simulations that in order to achieve this behavior, we should increase the working frequency until the wavelength becomes quite small compared to the waveguide diameter.

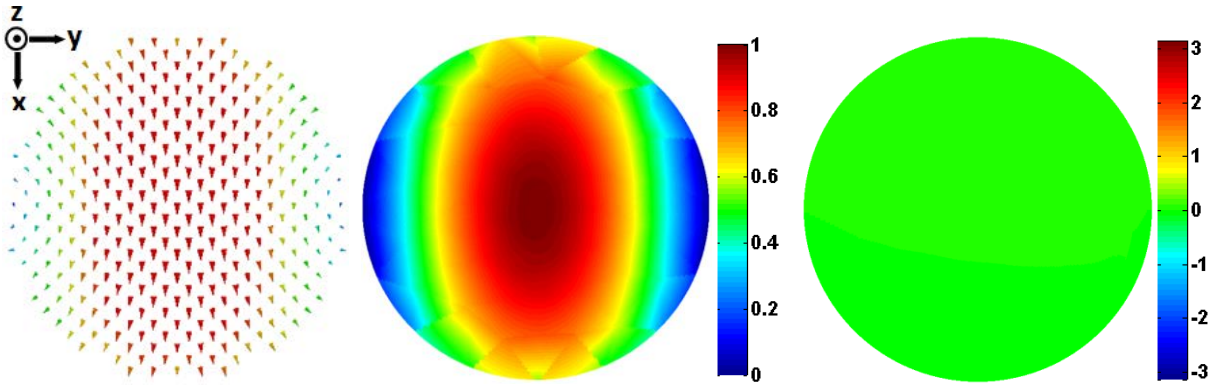

(a) (b) (c)

Figure IV-4: Field distribution of TE_{11} mode and the corresponding magnitude and phase patterns of E_x component: (a) Field distribution; (b) Normalized magnitude pattern; (c) Phase pattern.

The phase of the E_x component of the TE_{11} mode is constant on the wavefront. Thus, to create an OAM mode $\ell = 1$, the SPP should realize a phase shift of 2π in one turn (along φ angle) and the required step height h is given by [39]:

$$h = \frac{2\pi}{k_1 - k_2} \tag{IV-2}$$

However, in waveguide, k_1 and k_2 should be replaced by k_{g1} and k_{g2} which are the guided propagation constants for waveguide filled respectively with Teflon and air:

$$k_{gi} = \sqrt{k_0^2 \varepsilon_i - k_c^2} = \sqrt{\left(\frac{2\pi f}{c}\right)^2 \varepsilon_i - \left(\frac{\eta}{r}\right)^2} \tag{IV-3}$$

where f is the working frequency, c the speed of light in free space, ε_i the dielectric permittivity of the material inside the waveguide ($i = 1$ for Teflon and $i = 2$ for air), r the radius of the waveguide, and η a constant which depends on the guided mode. For TE_{11} mode, η is equal to 1.841.

Here, we set the diameter of the empty waveguide as 4.4 cm. The corresponding cut-off frequency of the TE_{11} mode is 4 GHz. Since the wavelength of the working frequency needs to be quite small compared to the waveguide diameter, we choose a working frequency of 40 GHz, and therefore, the height step of the SPP becomes: $h = 1.7$ cm.

The magnitude and phase patterns of the E_x component for the wave passing through the SPP are plotted in Figure IV-5. We can note that the magnitude at the center is much smaller than the surroundings and the phase variation in one turn is equal to 2π. This shows indeed that both the amplitude and the phase correspond to a wave bearing an OAM mode with $\ell = 1$. We can also observe that even at the frequency of 40 GHz, the magnitude and phase of the E_x field are not quite satisfactory. To improve the results, one solution would be to increase again the frequency. In the next section we propose another solution by using a horn structure.

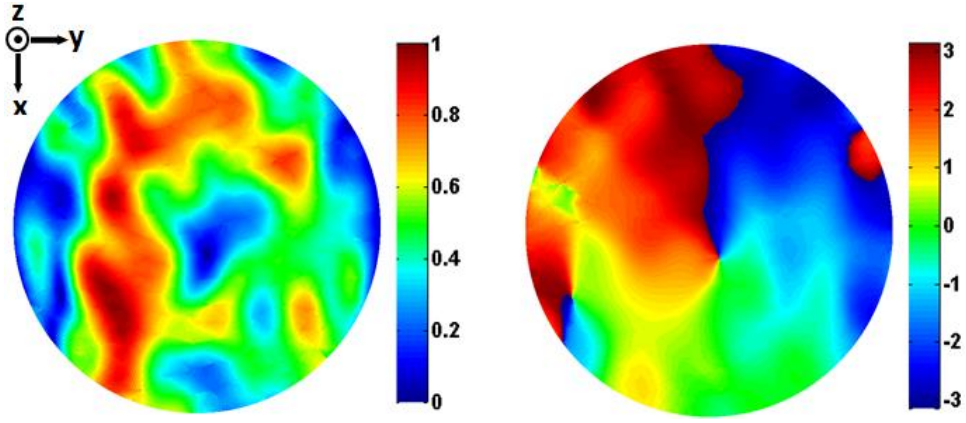

Figure IV-5: Normalized magnitude (left) and phase (right) patterns of E_x component for the structure with a single SPP at the frequency of 40 GHz

IV.3.1.2 Horn antenna design

IV.3.1.2.1 Ideal design

Our purpose is to create a directive OAM antenna. Thus, we design a conical horn antenna based on the circular waveguide, as shown in Figure IV-6. The TE_{11} mode is still excited ideally by a waveport polarized in x direction. The diameters of the waveguide and the horn aperture are respectively 4.4 and 12 cm, and the heights are 5 and 10 cm. We keep the working frequency at 40 GHz so that the wavelength at the working frequency is much smaller than the waveguide diameter, and therefore, the height step of the SPP is still 1.7 cm.

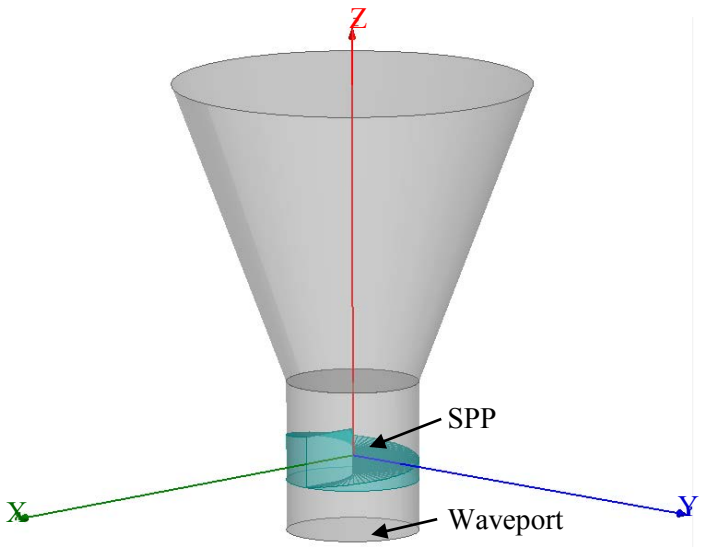

Figure IV-6: Geometry of the OAM horn antenna with a single SPP (SPP inside the waveguide)

Figure IV-7 shows the 3D radiation pattern of the OAM horn antenna at 40 GHz. The central hole is a signature of waves carrying OAM. Moreover, it can be observed that the OAM waves are very directive. The magnitude and phase patterns of the propagated wave, plotted on a circular area with a radius of 6 cm, lying 0.5 cm above the horn aperture, are presented in Figure IV-8. We can see that the magnitude at the center is much smaller than the surroundings and the phase rotates around the center with a 2π phase shift in one turn. This shows indeed that both the amplitude and the phase correspond to a wave bearing an OAM mode with $\ell = 1$. Besides, compared to the results of the waveguide structure with PML boundary, both the magnitude and the phase of E_x field are improved.

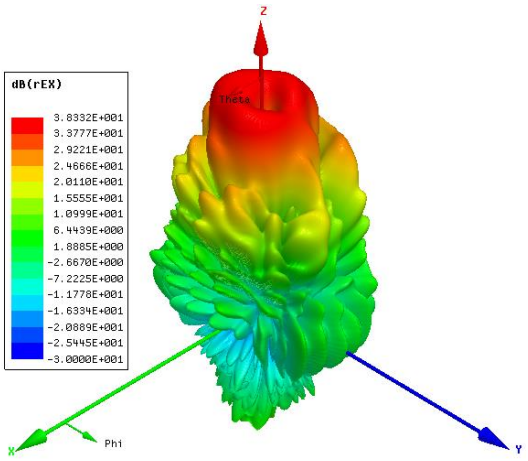

Figure IV-7: 3D Radiation pattern of the OAM horn antenna with a single SPP (SPP inside the waveguide) at the frequency of 40 GHz

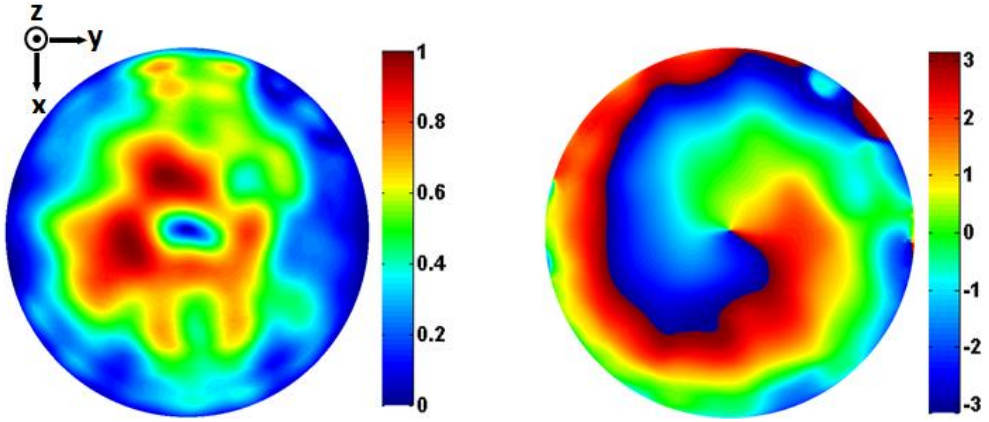

Figure IV-8: Normalized magnitude (left) and phase (right) patterns of E_x component for the OAM horn antenna with a single SPP (SPP inside the waveguide) at the frequency of 40 GHz

IV.3.1.2.2 Practical design

According to the above analysis, when the SPP is placed inside the waveguide, the wavelength at the working frequency should be much smaller than the diameter of the waveguide (~ 1/10). This will enable the high-order modes of the circular waveguide to exist at the same time, which makes it difficult to obtain a pure TE_{11} mode in practice. To solve this problem, we place the SPP inside the horn instead of inside the waveguide, as shown in Figure IV-9. In this way, the working frequency can be reduced to be quite near to the cut-off frequency of the TE_{11} mode.

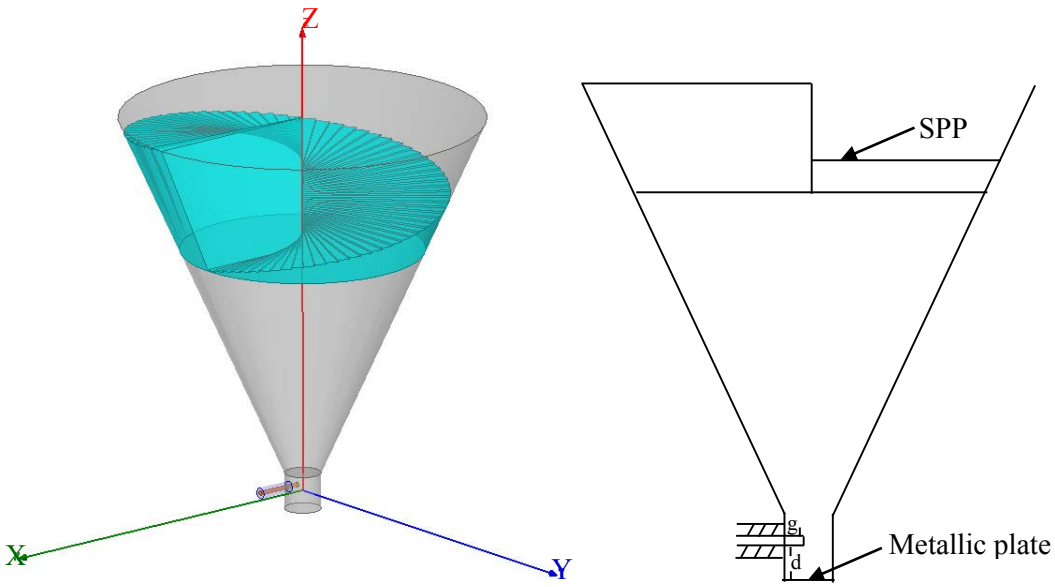

Figure IV-9: Geometry of the OAM horn antenna with a single SPP (SPP inside the horn): (a) 3D view of the antenna structure; (b) 2D view for showing the probe parameters

In this practical design, the empty waveguide has a diameter of 1 cm and the corresponding cut-off frequency of the TE_{11} mode is 17.6 GHz. The horn aperture has a diameter of 10 cm. The heights of the waveguide and the horn are respectively 1 and 10 cm. We choose a working frequency of 20 GHz to ensure that the corresponding wavelength is small enough compared the horn aperture diameter. The bottom surface of the waveguide is set as a metallic plate. A coaxial line exciting the monopole probe is placed along the radial direction of the circular waveguide, d = 0.7 cm above the metallic plate, for creating the TE_{11} mode. The coaxial line with ε_r = 2.1 (Teflon) has an inner diameter of 1.3 mm and an outer diameter of 4.4 mm, and these parameters correspond to a characteristic impedance of 50 Ω. The probe length is optimized at g = 0.3 cm to realize a good impedance matching. The SPP has been chosen to generate an ℓ = 1 OAM mode. Because the SPP here is placed inside the horn, we can no more use the above equations to calculate the height step of the SPP. According to the simulations, the optimized height step of the SPP becomes: h = 3.7 cm.

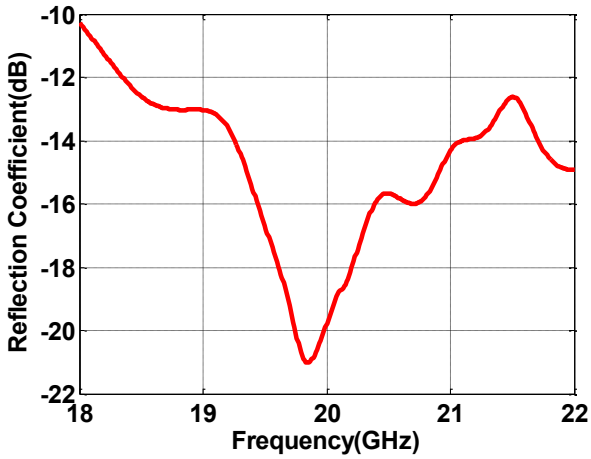

Figure IV-10: Reflection coefficient of the OAM horn antenna with a SPP inside the horn

As depicted in Figure IV-10, the horn antenna is well matched around 20 GHz and has a very large frequency bandwidth for the input impedance. Figure IV-11 presents the 3D radiation pattern and the 2D radiation and phase patterns at 20 GHz. The 3D radiation pattern has a null at the center that is a signature of OAM waves. The 2D radiation patterns correspond to the xOz and yOz cuts of the 3D plot. It can be seen that the maximum directivity is obtained at an angle of 14°. Compared to the OAM antenna using a circular phased array of 4 patches presented in Chapter II, where the maximum directivity is at 30°, the new antenna is therefore much more directive. We present the phase patterns (Figure IV-11c) for three values of the spherical angle (aperture) θ: 10°, 15° and 20°. The spiral form of the phase variation versus roll angle φ is due to the polar representation of the linear phase variation. We can observe that the quality of the phase pattern is good at small values of θ angle, but degrades as θ increases.

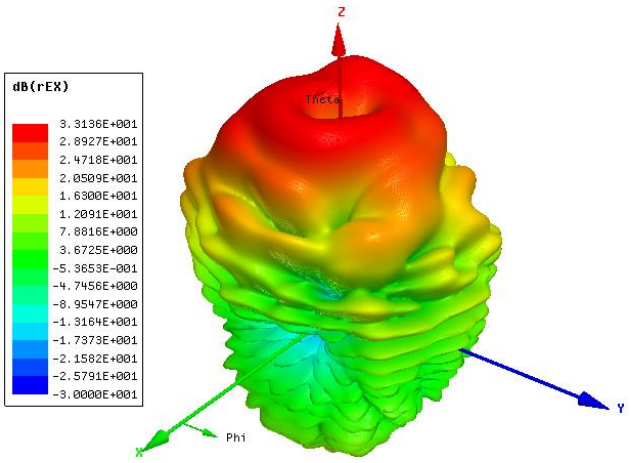

(a)

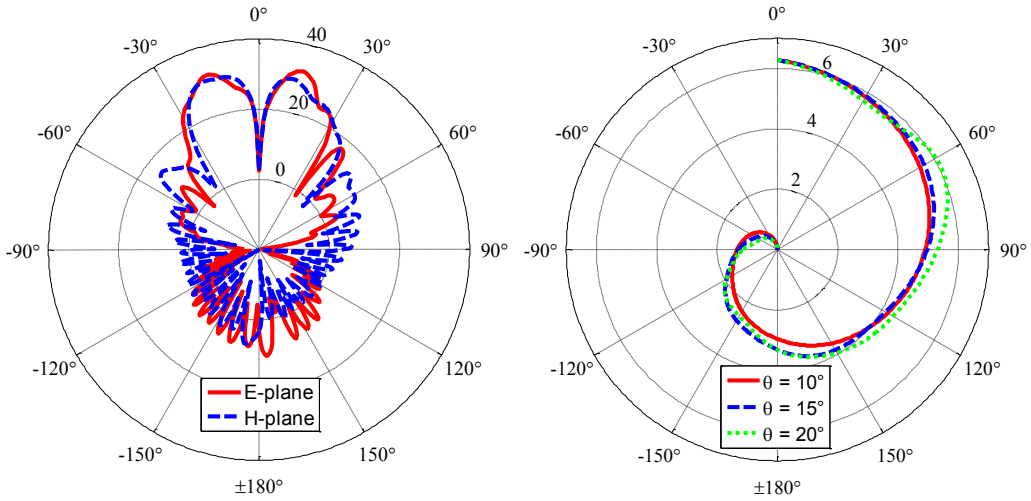

(b) (c)

Figure IV-11: Radiation and phase patterns of the OAM horn antenna with a single SPP (SPP inside the horn) at the frequency of 20 GHz: (a) 3D radiation pattern; (b) 2D radiation patterns in E and H planes: (c) Normalized phase patterns (in radians) at different θ angles

The magnitude and phase patterns of the propagated wave, observed on a plane perpendicular to the direction of propagation, are plotted in Figure IV-12. The observation window is a circular area with a radius of 5 cm, lying 2 cm above the horn aperture. It can be seen that the magnitude is minimum at the center and the phase rotates around the center with a 2π phase shift in one turn. This confirms the generation of a wave bearing an OAM with $\ell = 1$. Besides, we can observe that compared to the results in Figure IV-5, the quality of the phase of E_x field is improved, while the magnitude is still not very satisfactory. To improve this, in the next sections we design other horn antennas based on the TM_{01} or TE_{21} mode.

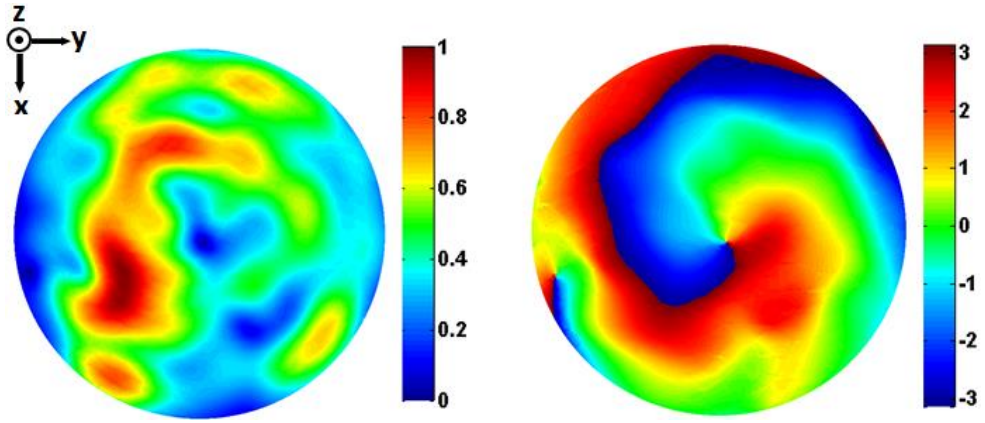

Figure IV-12: Normalized magnitude (left) and phase (right) patterns of E_x component for the OAM horn antenna with a single SPP at the frequency of 20 GHz (observation window: circular area with a radius of 5 cm, lying 2 cm above the horn aperture)

IV.3.2 TM_{01} mode and two half-turn SPPs

IV.3.2.1 SPP in waveguide

The geometry of the second structure is presented in Figure IV-13. It is similar to the previous one in the sense that again a SPP is used to create the phase shift. The main difference is that it contains two half-turn SPPs which have the same geometry. The two SPPs are placed inside the waveguide at the same height with a 180° rotation along z axis from each other.

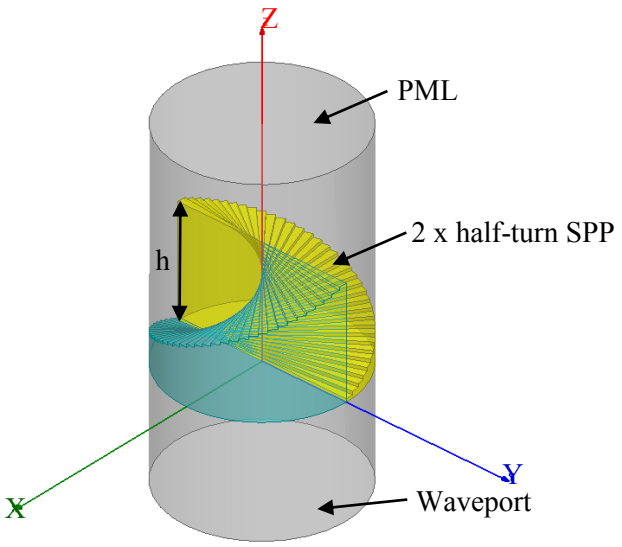

Figure IV-13: Geometry of the waveguide using TM_{01} mode, with two half-turn SPPs (PML: Perfectly Matched Layer)

Figure IV-14 shows the field distribution of the TM_{01} mode and the corresponding magnitude and phase patterns of the E_x component. The magnitude of the electrical field of the TM_{01} mode is minimal at the center and in this respect; it is close to the OAM wave (there is in fact a field vortex or singularity, created by the linear variation of the phase on the wavefront). Therefore, it should be easier to transform the TM_{01} mode into an OAM wave. The phase of the E_x component of the TM_{01} mode (Figure IV-14c) can be divided into two parts. For each part, the phase is constant on a plane perpendicular to the direction of propagation, and the phase difference between the two parts equals π. Thus, for creating the OAM mode of $\ell = 1$, two half-turn SPPs are needed. The step height of each SPP should realize a phase shift equal to π. In this way, the total phase shift in one turn will meet the requirement of 2π. We use again the equations (IV-2) and (IV-3) to calculate the step height of each half-turn SPP, but we should replace 2π by π in (IV-2). And for TM_{01} mode, the η parameter is equal to 2.405 in (IV-3).

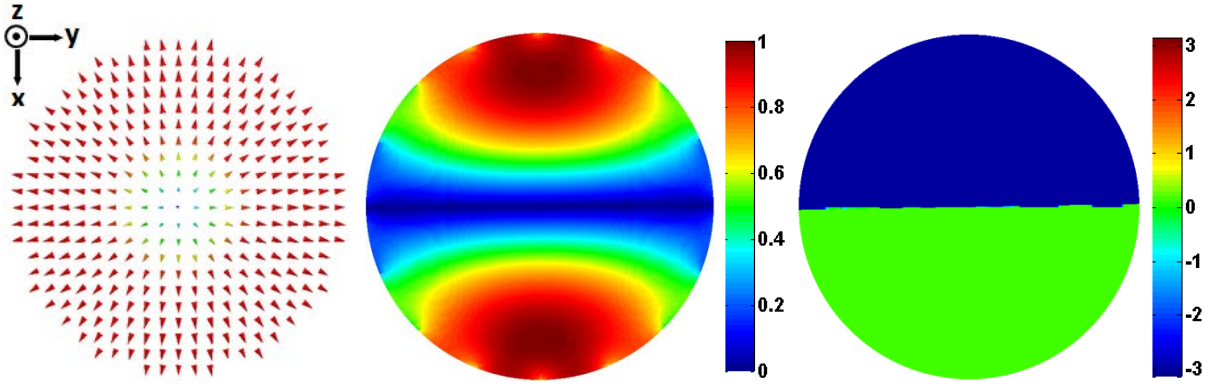

(a) (b) (c)

Figure IV-14: Field distribution of TM_{01} mode and the corresponding magnitude and phase patterns of E_x component: (a) Field distribution; (b) Normalized magnitude pattern; (c) Phase pattern.

The waveguide has a diameter of 4.4 cm, and the cut-off frequency of the TM_{01} mode is 5.2 GHz. The working frequency can be chosen to be much lower than that of the first structure; in fact, it just needs to be higher than the cut-off frequency of the TM_{01} mode. We choose a working frequency of 7.4 GHz, and therefore, the height step of each half-turn SPP becomes: h = 3.6 cm.

The magnitude and phase patterns of the E_x component for the wave at the end of the SPPs are given in Figure IV-15. We can observe that the magnitude pattern has a null at the center and the phase pattern has a linear variation along the roll angle φ with a 2π phase shift in one turn. This shows indeed that an OAM bearing wave with $\ell = 1$ is generated. We can also note that the results are better than those of the first structure.

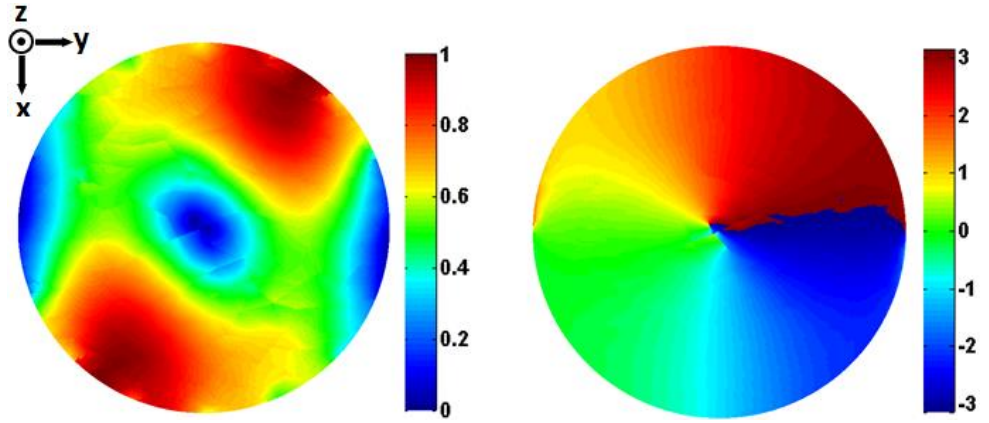

Figure IV-15: Normalized magnitude (left) and phase (right) patterns of E_x component for the structure with two half-turn SPPs at the frequency of 7.4 GHz (based on TM_{01} mode)

IV.3.2.2 Horn antenna design

We also design a practical conical horn antenna based on TM_{01} mode to make the OAM waves more directive, as shown in Figure IV-16. As discussed above, for TM_{01} mode, the working frequency can be quite near to the cut-off frequency, so no high-order modes will exist. Besides, the SPPs can be kept inside the waveguide. The diameters of the waveguide and the horn aperture are respectively 4.4 and 12 cm, and the heights are both 10 cm. The working frequency is kept at 7.4 GHz, and the height step of each "Teflon" half-turn SPP at 3.6 cm. The bottom surface of the waveguide is also set as a metallic plate. A coaxial line exciting the monopole probe placed along the direction of propagation is used to create the TM_{01} mode and it has the same parameters (material, inner and outer diameters) as the previous one. The SPPs are 2 cm above the probe. To satisfy the impedance matching, the probe length is optimized at 1.7 cm.

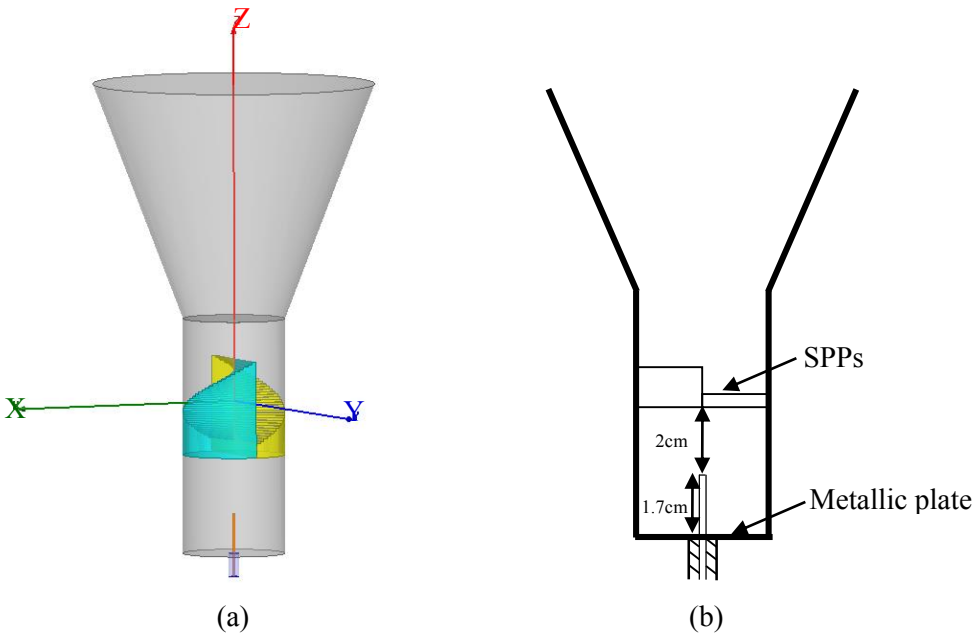

Figure IV-16: Geometry of the OAM horn antenna with two half-turn SPPs, based on TM_{01} mode: (a) 3D view of the antenna structure; (b) 2D view for showing the probe parameters

We can see from Figure IV-17 that the horn antenna with two half-turn SPPs is well matched around 7.4 GHz and the bandwidth is quite large (~13%). The 3D radiation pattern and the 2D radiation and phase patterns at 7.4 GHz are shown in Figure IV-18. We can again observe a central hole in the 3D radiation pattern that is characteristic of an OAM wave. Moreover, compared to the previous antenna, the main lobe is more smooth and symmetric and the side lobes are lower. The 2D radiation patterns also correspond to the xOz and yOz cuts of the 3D plot. We can see that the maximum directivity is obtained at the angle of 15°. The phase

patterns are plotted again for three values of the spherical angle (aperture) θ: 10°, 20° and 30°. We can also observe that the quality of the phase pattern degrades as θ increases.

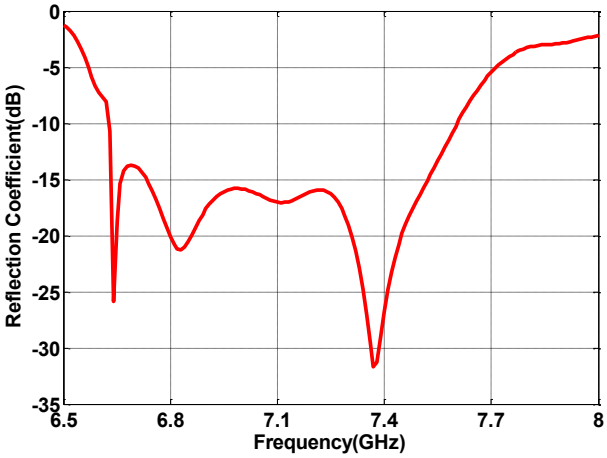

Figure IV-17: Reflection coefficient of the OAM horn antenna with two half-turn SPPs (based on TM_{01} mode)

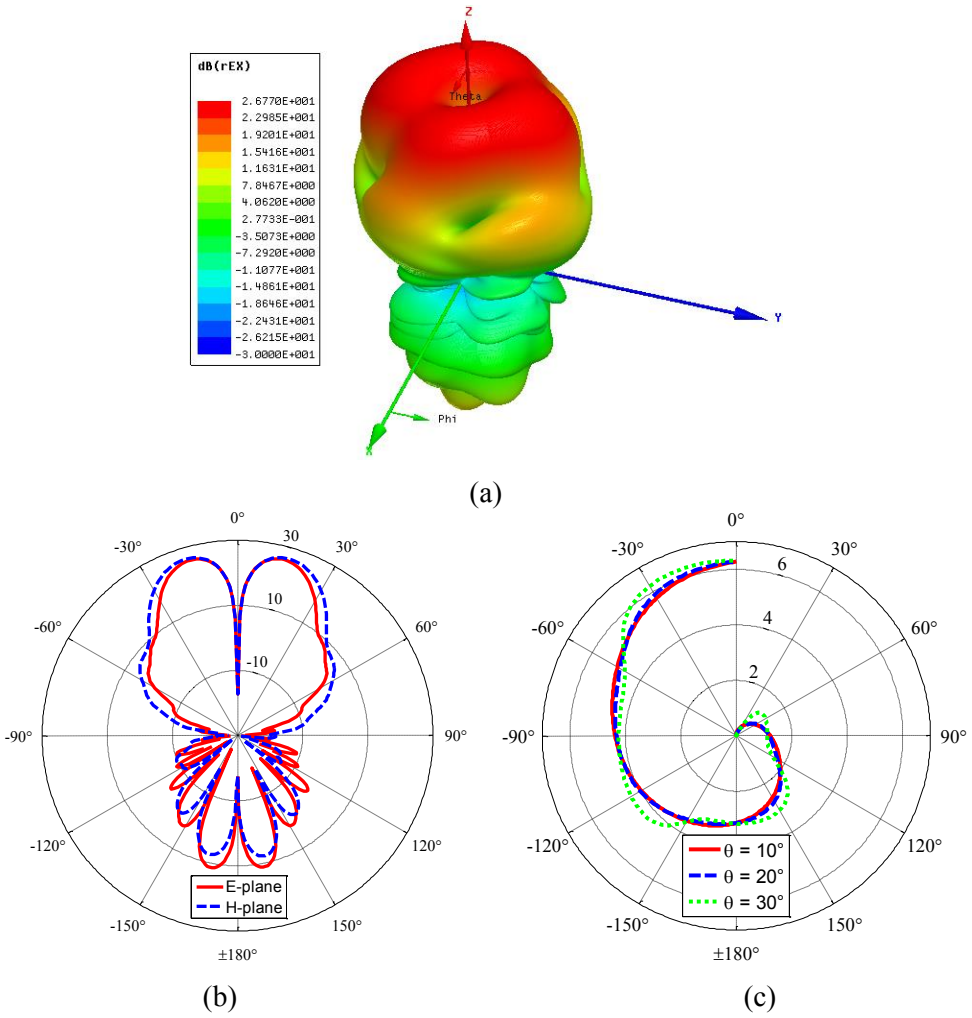

Figure IV-18: Radiation and phase patterns of the OAM horn antenna with two half-turn SPPs at the frequency of 7.4 GHz (based on TM_{01} mode): (a) 3D radiation pattern; (b) 2D radiation patterns in E and H planes; (c) Normalized phase patterns (in radians) at different θ angles

The magnitude and phase patterns of the propagated wave, plotted on a circular area with a radius of 7 cm, lying 1 cm above the horn aperture, are presented in Figure IV-19. We can observe that the magnitude at the center is much smaller than the surroundings and the phase rotates around the center with a 2π phase shift in one turn. This shows indeed that both the amplitude and the phase correspond to a wave carrying an OAM mode with $\ell = 1$. Besides, compared to the previous horn antenna, the magnitude of E_x field is improved.

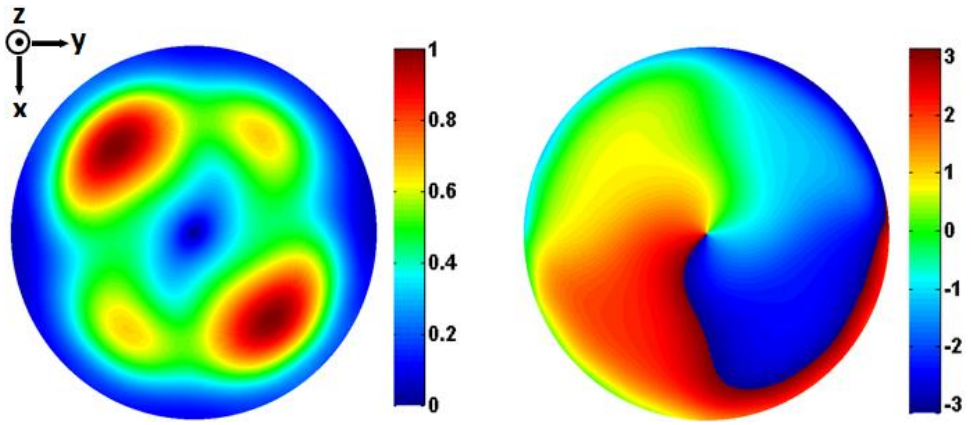

Figure IV-19: Normalized magnitude (left) and phase (right) patterns of E_x component for the OAM horn antenna with two half-turn SPPs at the frequency of 7.4 GHz (based on TM_{01} mode) (observation window: circular area with a radius of 7 cm, lying 1 cm above the horn aperture)

IV.3.3 TE_{21} mode and two half-turn SPPs

IV.3.3.1 SPP in waveguide

The third structure to generate OAM wave is presented in Figure IV-20. It is quite similar to the second one. The main difference is that the two half-turn SPPs both rotate π/2 along z axis.

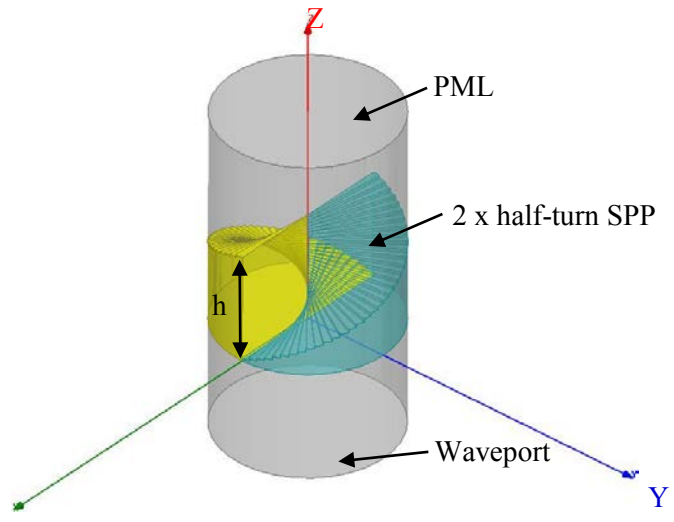

Figure IV-20: Geometry of the waveguide with two half-turn SPPs, using TE_{21} mode (PML: Perfectly Matched Layer)

Figure IV-21 shows the field distribution of the 1st kind of TE_{21} mode and the corresponding magnitude and phase patterns of the E_x component. We can observe that the E-field patterns have quite a similar distribution compared to the TM_{01} mode (Figure IV-14). The main difference is that there is a $\pi/2$ rotation of both magnitude and phase patterns. Therefore, as what has been done for the TM_{01} mode, we can use again two half-turn SPPs to transform the TE_{21} mode to an OAM wave. The equations (IV-2) and (IV-3) are used to calculate the step height of each half-turn SPP, but the 2π should be replaced by π in (IV-2). And for TE_{21} mode, the η parameter is equal to 3.054 in (IV-3).

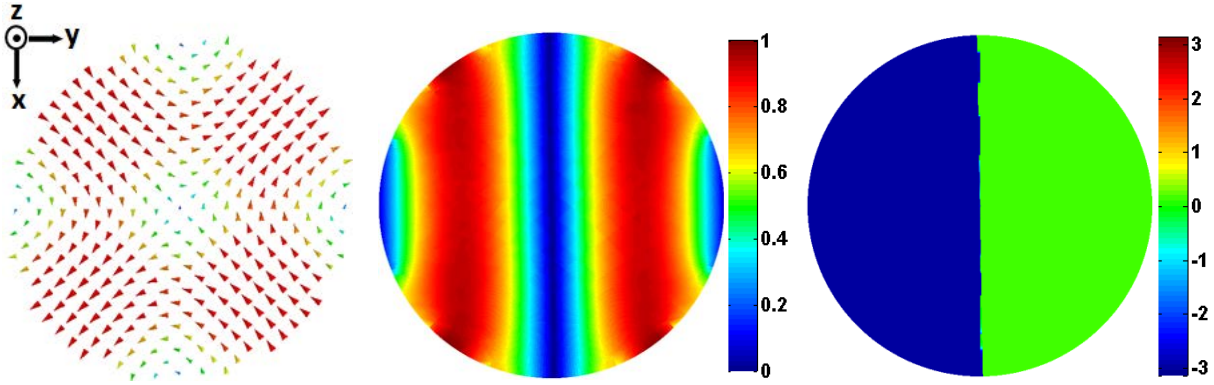

(a) (b) (c)

Figure IV-21: Field distribution of the 1st kind of TE_{21} mode and the corresponding magnitude and phase patterns of E_x component: (a) Field distribution; (b) Normalized magnitude pattern; (c) Phase pattern.

The diameter of the empty waveguide is 4.4 cm, and the corresponding cut-off frequency of the TE_{21} mode is 6.6 GHz. Similar to the TM_{01} mode, the working frequency just needs to be higher than the cut-off frequency of the TE_{21} mode. We choose a working frequency of 10 GHz, and therefore, the height step of each half-turn SPP becomes: $h =$ 2.7 cm.

The magnitude and phase patterns of the E_x component for the wave at the end of the SPPs are shown in Figure IV-22. We can note that the magnitude pattern has a null at the center and the phase pattern has a linear variation along the roll angle φ with a 2π phase shift in one turn. This confirms the generation of an OAM bearing wave with $\ell = 1$. We can also observe that the results are as good as those of the second structure.

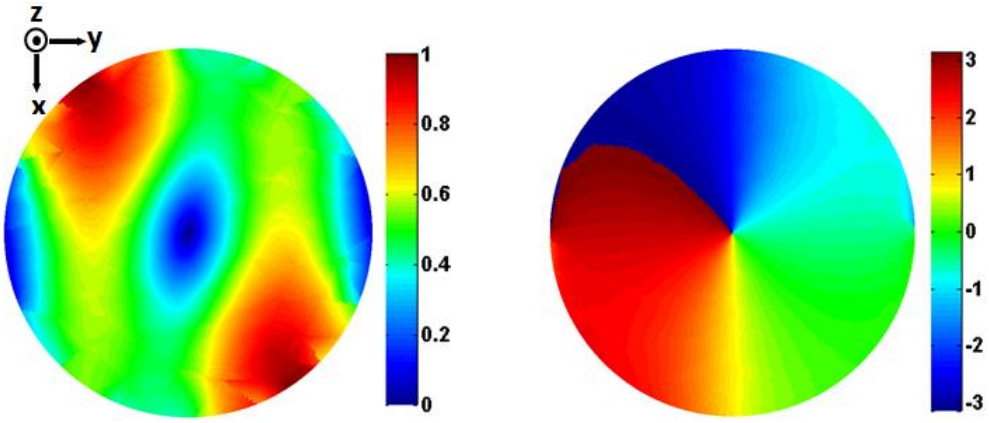

Figure IV-22: Normalized magnitude (left) and phase (right) patterns of E_x component for the structure with two half-turn SPPs at the frequency of 10 GHz ((based on TE_{21} mode)

IV.3.3.2 Horn antenna design

We use again a horn structure to enhance the directivity of the OAM antenna, as shown in Figure IV-23. Because it is difficult to excite a pure TE_{21} mode in practice, we only study the ideal model. The diameters of the waveguide and the horn aperture are respectively 4.4 and 12 cm, and the heights are both 8 cm. The working frequency is kept at 10 GHz, and the height step of each half-turn SPP at 2.7 cm.

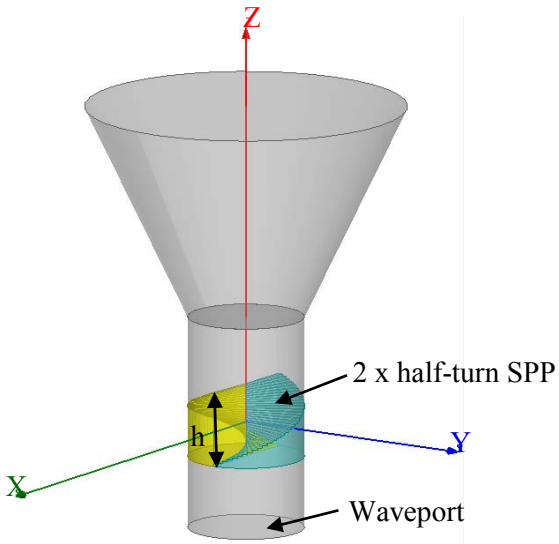

Figure IV-23: Geometry of the OAM horn antenna with two half-turn SPPs (based on TE_{21} mode)

Figure IV-24 shows the 3D radiation pattern of the OAM horn antenna at 10 GHz. The central hole is a signature of waves carrying OAM. The magnitude and phase patterns of the propagated wave, plotted on a circular area with a radius of 6 cm, lying 1 cm above the horn aperture, are presented in Figure IV-25. We can see that the magnitude at the center is much

smaller than the surroundings and the phase rotates around the center with a 2π phase shift in one turn. This shows indeed that both the amplitude and the phase correspond to a wave bearing an OAM mode with $\ell = 1$. Besides, compared to the horn antenna based on TM_{01} mode, both the 3D radiation pattern and the magnitude of E_x field are less symmetric.

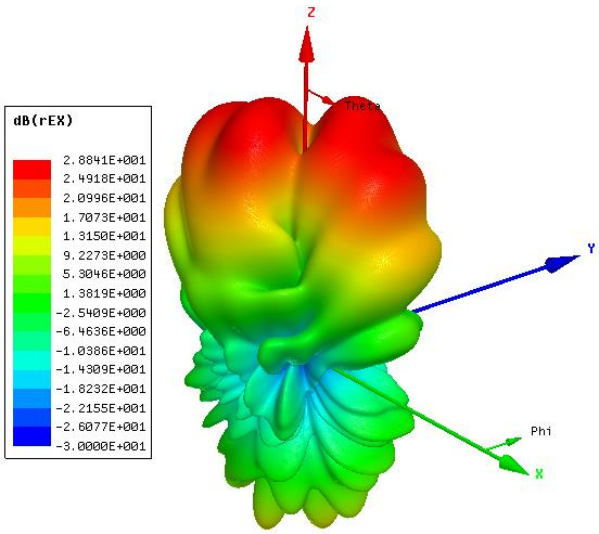

Figure IV-24: 3D Radiation pattern of the OAM horn antenna with two half-turn SPPs at the frequency of 10 GHz (based on TE_{21} mode)

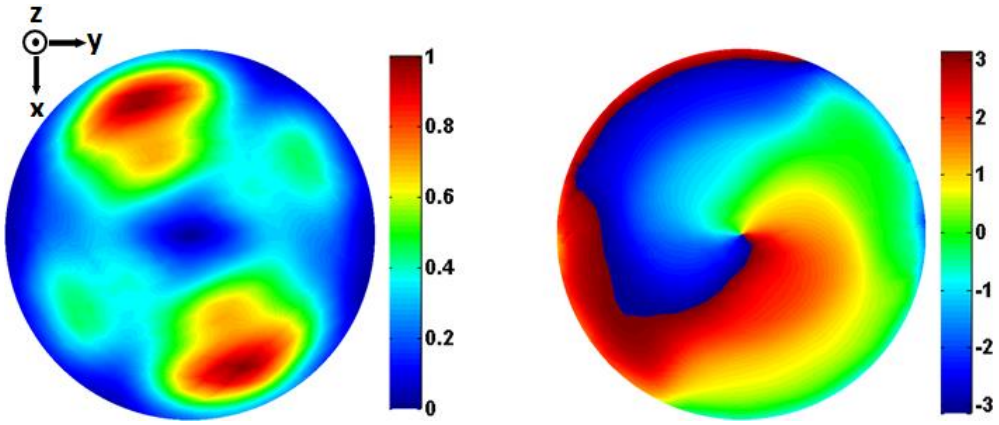

Figure IV-25: Normalized magnitude (left) and phase (right) patterns of E_x component for the OAM horn antenna with two half-turn SPPs at the frequency of 10 GHz (based on TE_{21} mode) (observation window: circular area with a radius of 6 cm, lying 1 cm above the horn aperture)

IV.4 Generation of OAM waves by combining guided modes

In the first chapter, we showed that in optics the Laguerre-Gaussian (LG) modes have rotational symmetry along their propagation axis and carry an OAM of $\ell\hbar$ per photon. They can be produced by combing two Hermite-Gaussian (HG) modes. As an example, a helically phased

LG_{01} mode ($\ell = 1$ or -1) is obtained by combining two HG modes of HG_{01} and HG_{10} with a $\pi/2$ phase difference between them [1]. Along this way, a rectangular silicon waveguide has already been used to generate optical OAM beams by combining the E^x_{21} and E^x_{12} modes [74].

In the same manner, by combining some proper modes of a metallic waveguide we can create OAM waves in radio frequency bands. In this part, we propose two methods to obtain the OAM mode of $\ell = 1$: i) combination of two kinds of TE_{21} modes; ii) combination of TM_{01} and TE_{21} modes.

IV.4.1 Combination of two kinds of TE_{21} modes

The first method to generate OAM waves in a circular metallic waveguide is based on the combination of two kinds of TE_{21} modes. Figure IV-21 shows the field distribution of the 1st kind of TE_{21} mode and the corresponding magnitude and phase patterns of E_x component and Figure IV-26, the 2nd kind of TE_{21} mode. One can see that the E-field patterns of the 2nd kind of TE_{21} mode have quite a similar distribution compared to the 1st kind of TE_{21} mode. The main difference is just a $\pi/2$ rotation of both magnitude and phase patterns. Moreover, due to the symmetrical distribution of the electrical field, for each kind of TE_{21} mode the magnitude and phase patterns of E_y component have an identical distribution compared to the E_x component, the only difference is that both the magnitude and phase patterns rotate $\pi/2$ (see Figures IV-27 and IV-28).

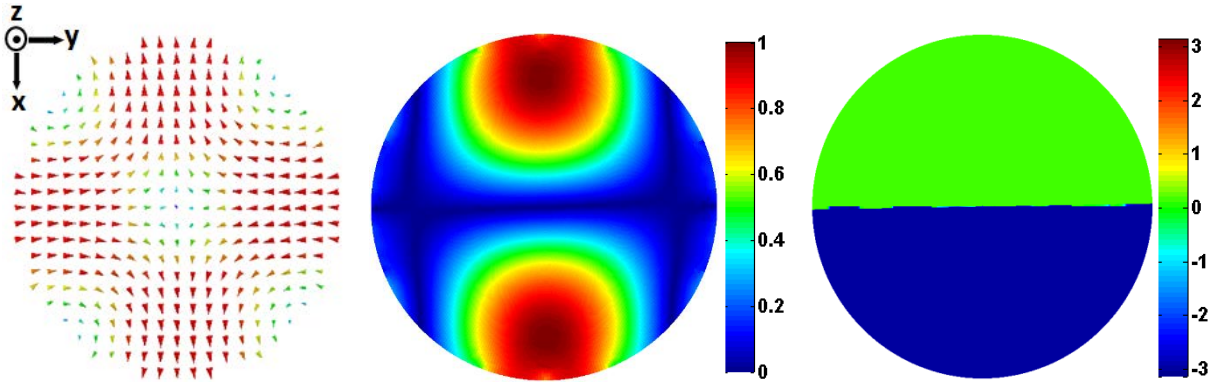

(a) (b) (c)

Figure IV-26: Field distribution of the 2nd kind of TE_{21} mode and the corresponding magnitude and phase patterns of E_x component: (a) Field distribution; (b) Normalized magnitude pattern; (c) Phase pattern.

Inspired from what was done in optics, we simultaneously excite the two kinds of TE_{21} modes with a $\pi/2$ phase difference. The evolutions of the magnitude and phase patterns of E_x and E_y components for the generation of an OAM wave are respectively shown in Figures IV-

27 and IV-28. It can be seen that the magnitude pattern is uniformly distributed with a null at the center and the phase rotates around the center with a 2π phase shift in one turn. This shows indeed that for each component, both the amplitude and the phase correspond to a wave bearing an OAM mode ℓ equal to 1.

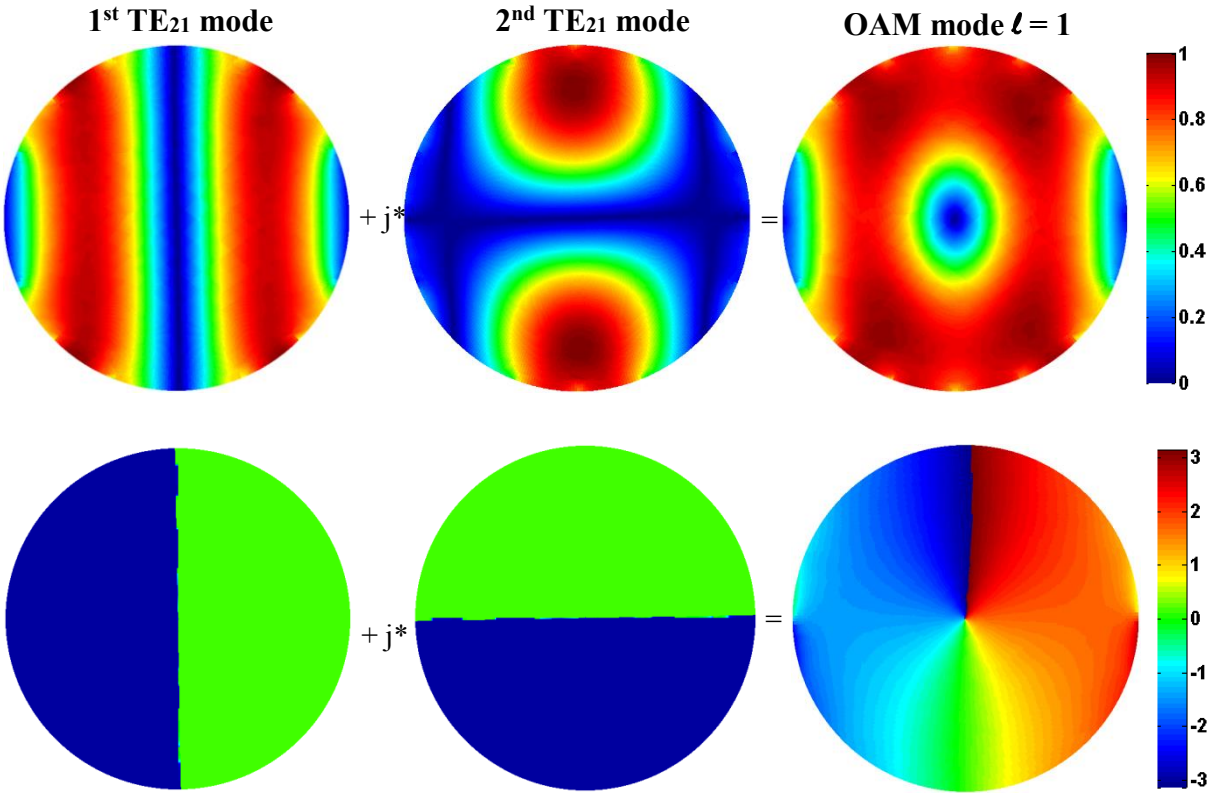

Figure IV-27: Evolutions of magnitude (top) and phase (bottom) patterns of E_x component for the generation of an OAM wave, by combining two kinds of TE_{21} modes with a π/2 phase difference

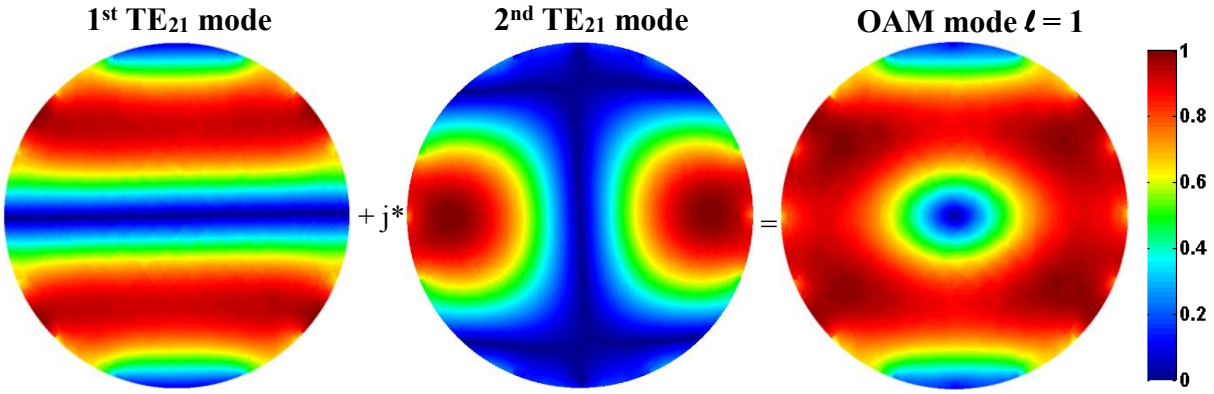

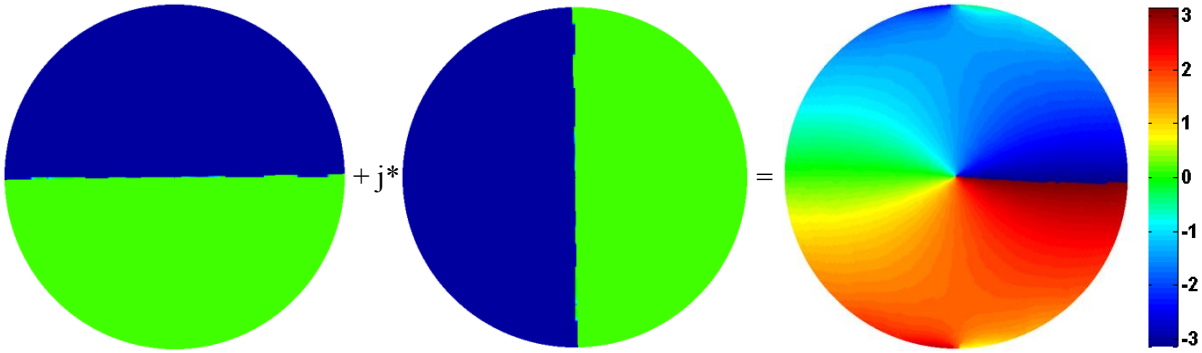

Figure IV-28: Evolutions of magnitude (top) and phase (bottom) patterns of E_y component for the generation of an OAM wave, by combining two kinds of TE_{21} modes with a π/2 phase difference

Because it is difficult to excite a pure TE_{21} mode in practice, we only study the ideal situation where the two TE_{21} modes are excited by a waveport in HFSS software. In the next section we propose another method by combining the TM_{01} and TE_{21} modes, as well as the design of an "OAM antenna" based on this method.

IV.4.2 Combination of TM_{01} and TE_{21} modes

The second method to generate OAM waves in a circular metallic waveguide is similar to the first one. It is by a combination of TM_{01} and the 1st kind of TE_{21} modes. The field distributions of these two modes and the corresponding magnitude and phase patterns of E_x component are shown in Figures IV-14 and IV-21. We can observe again that the E-field patterns of these two modes are quite similar. The main difference is just a π/2 rotation of both magnitude and phase patterns. Besides, the E-field of the TM_{01} mode also has a symmetrical distribution. Thus, its E_y component is almost the same with the E_x component except a π/2 rotation of both magnitude and phase patterns along z axis.

To create the OAM guided wave, we simultaneously excite the TM_{01} and TE_{21} modes with a π/2 phase difference. The resulting magnitude and phase patterns of E_x and E_y components are shown in Figure IV-29. We can observe that the magnitude patterns have a null at the center and the phases have a linear variation along the roll angle φ with a 2π phase shift in one turn. This shows indeed that for each component, both the amplitude and the phase correspond to a wave carrying an OAM mode with $\ell = 1$.

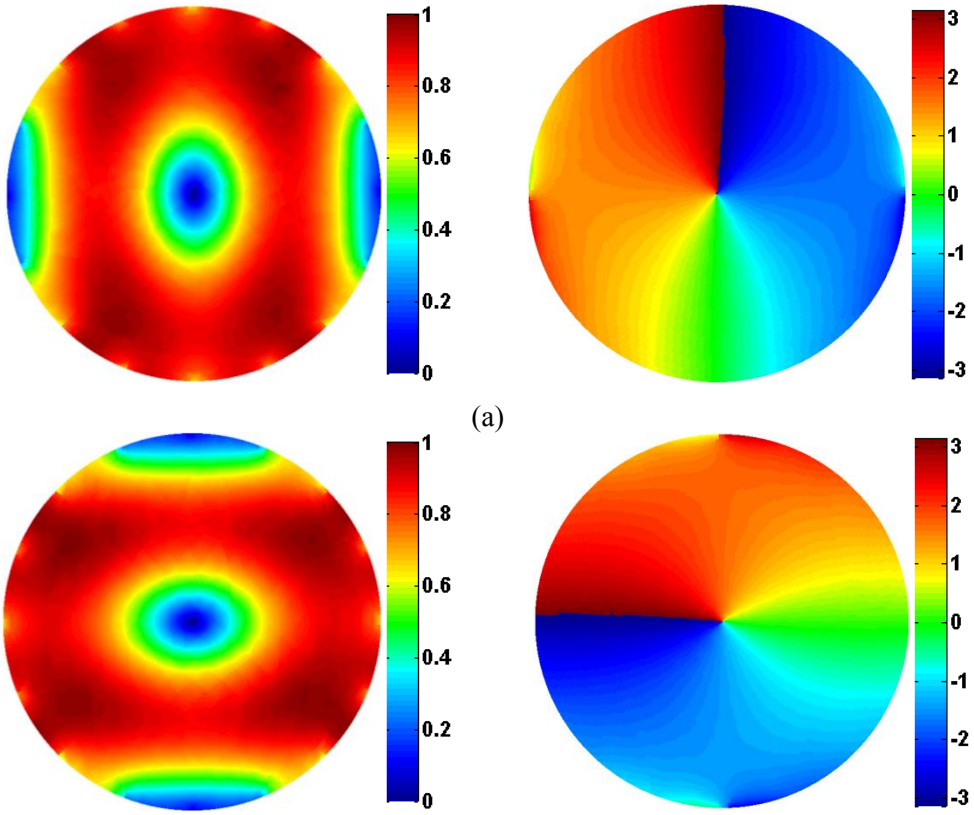

(a)

(b)

Figure IV-29: Magnitude (left) and phase (right) patterns of the combined TM_{01} and TE_{21} modes: (a) E_x component; (b) E_y component

To realize this antenna, we introduce two printed monopoles inside a circular metallic waveguide to simultaneously create the TM_{01} and TE_{21} modes. The configuration of the proposed "OAM antenna" is shown in Figure IV-30. The empty waveguide has a diameter of 4 cm and a height of 5 cm, the corresponding cut-off frequencies of the TM_{01} and TE_{21} modes are respectively 5.7 and 7.3 GHz. We choose a working frequency of 8.3 GHz to allow the propagation of the TM_{01} and TE_{21} modes and to prevent other high-order modes existing.

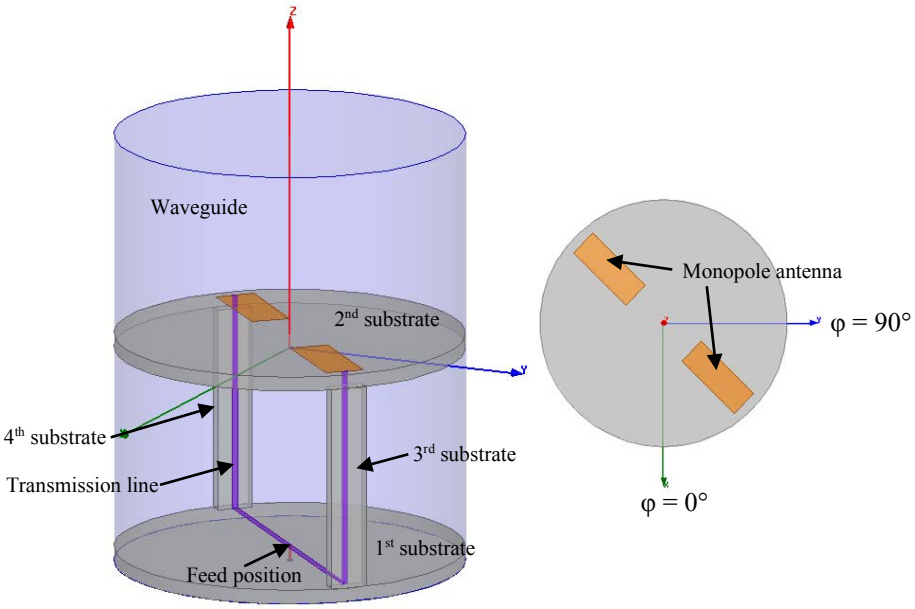

Figure IV-30: Configuration of the proposed OAM antenna, using the combination of TM_{01} and TE_{21} modes

From the electrical field distributions of the TM_{01} and the 1st kind of TE_{21} modes (see Figures IV-14 and IV-21); we can find that to create these two modes, the two monopole antennas should be placed on the same line and be out of phase. To this purpose, the two monopole antennas are connected with a single transmission line which is back-fed at the center point with a 50 Ω coaxial cable. In addition, since the field intensity of the TE_{21} mode is maximal at $\varphi = \pm 45°$ and $\pm 135°$, the monopole antennas should also be placed at the corresponding positions. In our design, we place the monopole antennas at $\varphi = 45°$ and -135°.

The monopole antennas and the transmission line are both manufactured on FR4 substrates with a thickness of 1.6 mm and a relative permittivity of 4.4. The substrate totally has 4 parts. The 1st substrate is placed at the bottom of the waveguide with the same diameter and the 2nd one, in the middle of the waveguide. The 3rd and 4th substrates are placed along the side wall of the waveguide and are used to connect the 1st and 2nd substrates. The transmission line has a width of 0.7 mm and an impedance of 100 Ω. To satisfy the working frequency and the impedance matching, the length and width of each monopole antenna are optimized at 12 and 4.5 mm, respectively.

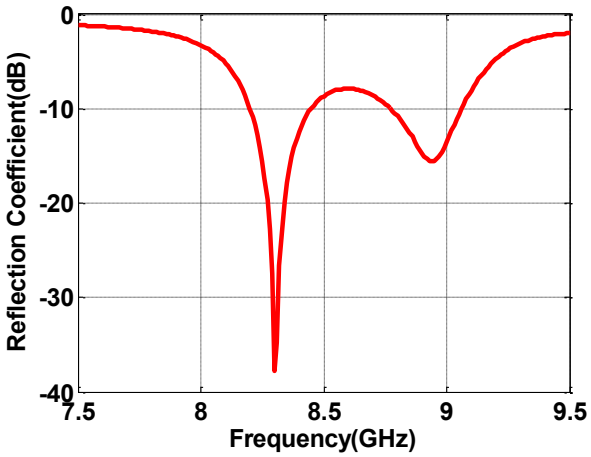

Figure IV-31: Reflection coefficient of the OAM antenna, using the combination of TM_{01} and TE_{21} modes

As depicted in Figure IV-31, the antenna is well matched around 8.3 GHz. The magnitude and phase patterns of the propagated wave, observed on a plane perpendicular to the direction of propagation, are shown in Figure IV-32. The observation window is a circular area with a radius of 3 cm, lying 1 cm above the waveguide aperture. It can be seen that for both E_x and E_y components, the magnitude at the center is much smaller than the surroundings and the phase rotates around the center with a 2π phase shift in one turn. This shows indeed that for each component, both the amplitude and the phase of the generated wave correspond to an OAM bearing wave with $\ell = 1$.

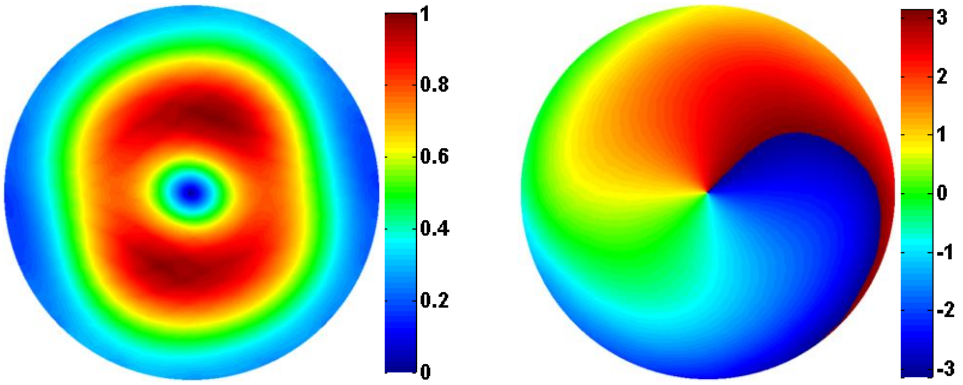

(a)

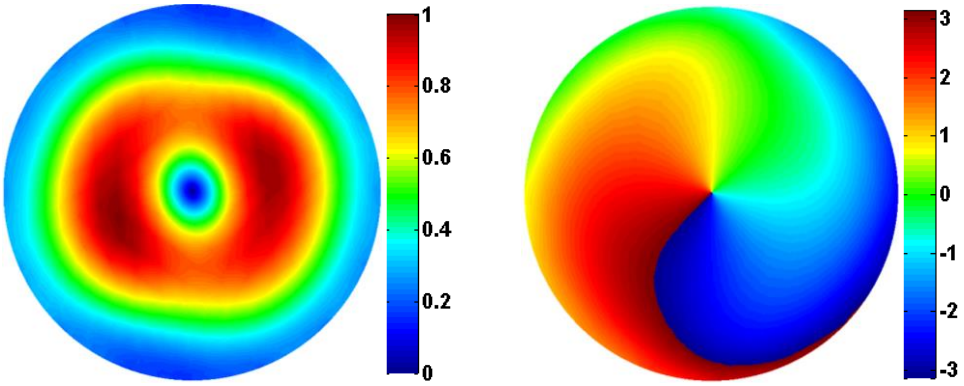

(b)

Figure IV-32: Magnitude (left) and phase (right) patterns of the propagated wave: (a) E_x component; (b) E_y component (observation window: circular area with a radius of 3 cm, lying 1 cm above the waveguide aperture)

At a working frequency of 8.3 GHz, the TE_{11}, TM_{01} and two kinds of TE_{21} modes are able to propagate in the waveguide. However, the monopole antennas are out of phase and they are placed at φ = 45° and -135°. Due to this fact, the TE_{11} and the 2nd kind of TE_{21} modes are eliminated. Thus, we can conclude that the OAM wave is generated by a combination of the TM_{01} and the 1st kind of TE_{21} modes.

Figure IV-33 shows the 3D radiation and phase patterns of the OAM antenna. For each component, the radiation patterns in magnitude and phase depict the vortex that is characteristic of an OAM wave. The spiral form of the phase pattern, plotted in polar coordinates, corresponding to the linear variation of the phase against the roll angle (φ, in Figure IV-33b).

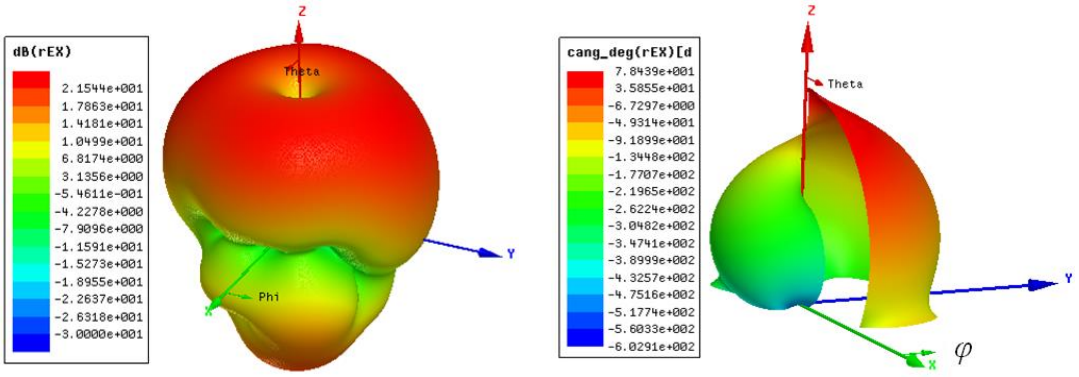

(a)

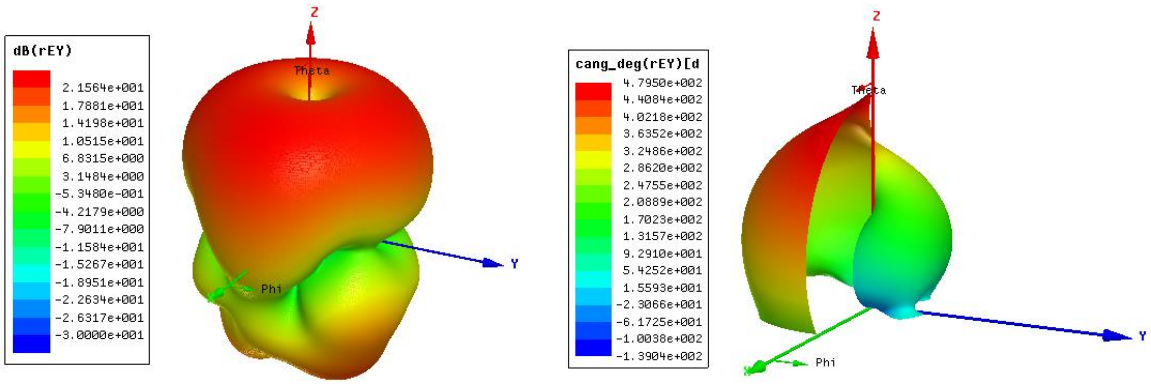

(b)

Figure IV-33: 3D radiation (left) and phase (right) patterns of the OAM antenna: (a) E_x component; (b) E_y component

IV.5 Conclusions

In this chapter, we have presented two main methods to generate radio OAM waves in a circular waveguide. The first method is to transform the classical guided modes of a circular waveguide to an OAM wave by using SPP. A horn structure is used to create a directive OAM antenna. The OAM mode of $\ell = 1$ is generated for the E_x component, based on TE_{11} mode with a single SPP, or TM_{01} mode with two half-turn SPPs, or TE_{21} mode with two half-turn SPPs. The resulting magnitude and phase patterns of the electrical field, and the radiation and phase patterns all confirm the generation of an OAM bearing wave. There are some differences between the three horn antennas: i) to enable the working frequency to be near cut-off, for TE_{11} mode, the SPP should be placed inside the horn, while for TM_{01} and TE_{21} modes, it can be maintained inside the waveguide; ii) the magnitude pattern of E_x field of the horn antenna based on TM_{01} mode is better than those of the other two antennas; iii) the horn antenna based on TM_{01} mode has also a smoother and more regular radiation pattern with lower side lobes.

The second method is by a combination of the classical guided modes. Actually, we have developed two different ways to obtain the OAM mode: i) combination of two kinds of TE_{21} modes; ii) combination of TM_{01} and 1st kind of TE_{21} modes. The OAM mode of $\ell = 1$ is generated for both the E_x and E_y components. The resulting magnitude and phase patterns of the electrical field confirm the generation of an OAM bearing wave. In addition, we designed an antenna using two printed monopoles and a single transmission line to simultaneously create the TM_{01} and TE_{21} modes and hence, to generate an OAM wave with $\ell = 1$. Both the electrical field patterns and the radiation patterns of this antenna evidence the presence of an OAM carrying wave.

Conclusions and Perspectives

In this thesis we have presented several new antennas for generating radio waves bearing Orbital Angular Momentum (OAM), which is necessary for any existing and future application.

In the first chapter we introduced the properties of waves bearing OAM and reviewed the typical methods for generating these waves. According to the working frequency, these methods can be used either in optics or in radio domain. In optics, three main techniques were used to generate OAM beams: spiral phase plate, Laguerre-Gaussian mode and diffraction grating. In radio domain, two main families of antennas were proposed to generate OAM waves: plane wave transformers (spiral phase plate, flat phase plat, diffraction grating and spiral reflector) and circular phased arrays.

In the second chapter, we developed an OAM antenna using 4 patches and an original circular phase shifter-power divider to generate an $\ell = 1$ OAM wave at 2.5 GHz. We firstly investigated the influences of the array parameters (number of array elements (N) and array radius (R)) on the performance of an ideal phased patch array and made the following conclusions: i) as N increases, the OAM modes become purer and of better quality, but the array becomes larger and more complex to realize; ii) $N = 4$ the smallest number of array elements that can produce the mode $\ell = 1$ with quite good quality; iii) as R increases, the OAM beam becomes more directive, but naturally some side lobes appear and the antenna geometry becomes larger.

On the other hand, we designed and realized an OAM antenna based on these conclusions. This antenna consists of 4 elements with an array radius of 50 mm. Appropriate weights (phase and amplitude) were obtained for the array elements with the use of the phase shifter-power divider. Both the 3D radiation & phase patterns and the 2D magnitude & phase patterns of the electrical field confirm the generation of an OAM bearing wave with $\ell = 1$. Besides, good agreement is obtained between theoretical results, simulation data and measurements.

In the third chapter we present a method to enhance the directivity of the previous developed OAM antenna by using a Fabry-Perot (FP) cavity. A FP cavity is generally composed of a ground plane, an air cavity and a partially reflecting surface (PRS). It is highly frequency selective and is often used to improve the antenna directivity in antenna applications.

We embed the OAM antenna inside the FP cavity with two different PRS. The first one is made of a set of periodic metallic strips printed on a FR4 substrate, and the second, made of metallic tubes. We chose the strips with a width of 4 mm and the tubes with a diameter of 4

mm. The influences of the parameters of the FP cavity on the antenna directivity were studied. To obtain a maximum directivity, the periods of the strips and the tubes were optimized at 20 and 26 mm, the cavity thickness at 58 mm and the dimension of the cavity aperture at 600 mm × 600 mm. In addition, the second PRS is closed on the sides using 4 walls: 2 PVC walls in H-plane for supporting the tubes and 2 PEC walls in E-plane for mechanical balance and decreasing the side lobe level of the radiation pattern. The FP OAM antenna finally achieved a directivity of 16.2 dB with an enhancement of 9.2 dB in E and H planes.

In the practical design, a circular phase shifter-power divider was used to supply the required phases and amplitudes for the array elements. The design procedure and the simulation data of the two practical FP OAM antennas were given, as well as the measurements of the second antenna.

In the fourth and last chapter, we presented several horn antennas and a waveguide antenna for generating radio OAM waves. These structures are all based on a circular metallic waveguide. Actually, we have developed two major methods to obtain the OAM mode: i) transformation of the guided modes of a circular waveguide by using the spiral phase plate; ii) combination of the guided modes.

For the first method, the OAM mode of $\ell = 1$ is generated for the E_x component, based on TE_{11} mode with a single SPP, or TM_{01} mode with two half-turn SPPs, or TE_{21} mode with two half-turn SPPs. The resulting magnitude and phase patterns of the electrical field, and the radiation and phase patterns all confirm the generation of an OAM bearing wave. There are some differences between the three proposed horn antennas: i) to enable the working frequency to be near cut-off, for TE_{11} mode, the SPP should be placed inside the horn, while for TM_{01} and TE_{21} modes, it can be maintained inside the waveguide; ii) the magnitude pattern of E_x field of the horn antenna based on TM_{01} mode is better than those of the other two antennas; iii) the horn antenna based on TM_{01} mode has also a smoother and more regular radiation pattern with lower side lobes.

For the second method, the OAM mode of $\ell = 1$ is generated for both the E_x and E_y components, by combining the two kinds of TE_{21} modes or TM_{01} and 1st kind of TE_{21} modes. The resulting magnitude and phase patterns of the electrical field confirm the generation of an OAM bearing wave. In addition, we designed an antenna using two printed monopoles and a single transmission line to simultaneously create the TM_{01} and TE_{21} modes and hence, to generate an OAM wave with $\ell = 1$. Both the electrical field patterns and the radiation patterns of this antenna evidence the presence of an OAM carrying wave.

In continuation of this thesis, the following perspectives are considered:

- Realize the horn antennas and the waveguide antenna for validation of the simulation results.
- Use the proposed OAM horn antennas as a “primary source” for simple parabolic reflectors to obtain high directivities at a low cost.
- Use the proposed OAM horn antennas as a “primary source” for twisted parabolic reflectors to produce a higher order OAM while maintain the high directivity.
- Apply the proposed OAM antennas to radio communications [5-9] and radars [11-13].

References

[1] L. Allen, M. W. Beijersbergen, R. J. C. Spreeuw, and J. P. Woerdman, "Orbital angular momentum of light and the transformation of Laguerre-Gaussian laser modes," *Phys. Rev. A*, vol. 45, no. 11, pp. 8185–8189, Jun. 1992.

[2] J. E. Curtis and D. G. Grier, "Structure of optical vortices," *Phys. Rev. Lett.*, vol. 90, 133901, Apr. 2003.

[3] G. Knöner, S. Parkin, T. A. Nieminen, V. L. Y. Loke, N. R. Heckenberg, and H. Rubinsztein-Dunlop, "Integrated optomechanical microelements," *Opt. Express*, vol. 15, no. 9, pp. 5521-5530, Apr. 2007.

[4] T. Kuga, Y. Torii, N. Shiokawa, T. Hirano, Y. Shimizu, and H. Sasada, "Novel Optical Trap of Atoms with a Doughnut Beam," *Phys. Rev. Lett.*, vol. 78, no. 25, pp. 4713-4716, Jun. 1997.

[5] S. M. Mohammadi, L. K. S. Daldorff, J. E. S. Bergman, R. L. Karlsson, B. Thide, K. Forozesh, T. D. Carozzi, and B. Isham, "Orbital angular momentum in radio - a system study," *IEEE Trans. Ant. Propag.*, vol. 58, no. 2, pp. 565–572, Feb. 2010.

[6] F. Tamburini, E. Mari, A. Sponselli, B. Thidé, A. Bianchini, and F. Romanato, "Encoding many channels on the same frequency through radio vorticity: First experimental test," *New J. Phys.*, vol. 14, 033001, Mar. 2012.

[7] J. Wang, J. Y. Yang, I. M. Fazal, N. Ahmed, Nisar Ahmed, Y. Yan, H. Huang, Y. Ren, Y. Yue, S. Dolinar, M. Tur, and A. E. Willner, "Terabit free-space data transmission employing orbital angular momentum multiplexing," *Nat. Photon.*, vol. 6, no. 7, pp. 488-496, Jun. 2012.

[8] Y. Yan, G. D. Xie, M. P. J. Lavery, H. Huang, N. Ahmed, Nisar Ahmed, C. Bao, Y. Ren, Y. Cao, L. Li, Z. Zhao, A. F. Molisch, M. Tur, M. J. Padgett, and A. E. Willner, "High-capacity millimetre-wave communications with orbital angular momentum multiplexing," *Nat. Commun.*, vol. 5, 4876, Sep. 2014.

[9] X. Hui, S. Zheng, Y. Chen, Y. Hu, X. Jin, H. Chi, and X. Zhang, "Multiplexed millimeter wave communication with dual orbital angular momentum (OAM) mode antennas," *Sci. Rep.*, vol. 5, 10148, May 2015.

[10] B. Thidé, H. Then, J. Sjöholm, K. Palmer, J. Bergman, T. D. Carozzi, Y. N. Istomin, N. H. Ibragimov, and R. Khamitova, "Utilization of photon orbital angular momentum in the low-frequency radio domain," *Phys. Rev. Lett.*, vol. 99, 087701, Aug. 2007.

[11] O. Edfors and A. J. Johansson, "Is orbital angular momentum (OAM) based radio communication an unexploited area?," *IEEE Trans. Ant. Propag.*, vol. 60, no. 2, pp. 1126–1131, Feb. 2012.

[12] M. Tamagone, C. Craeye, and J. Perruisseau-Carrier, "Comment on 'Encoding many channels on the same frequency through radio vorticity: First experimental test," *New J. Phys.*, vol. 14, 118001, Nov. 2012.

[13] F. Tamburini, B. Thidé, E. Mari, A. Sponselli, A. Bianchini, and F. Romanato, "Reply to Comment on 'Encoding many channels on the same frequency through radio vorticity: First experimental test," *New J. Phys.*, vol. 14, 118002, Nov. 2012.

[14] N. Uribe-Patarroyo, A. Fraine, D. S. Simon, O. Minaeva, and A. V. Sergienko, "Object identification using correlated orbital angular momentum states," *Phys. Rev. Lett.*, vol. 110, 043601, Jan. 2013.

[15] K. Liu, Y. Chen, Z. Yang, H. Wang, Y. Qin, and X. Li "Orbital-Angular-Momentum-based electromagnetic vortex imaging," *IEEE Ant. Wirel. Propag. Lett.*, vol. 14, pp. 711-714, Mar. 2015.

[16] M. Lin, Y. Gao, P. Liu, and J. Liu, “Improved OAM-based radar targets detection using uniform concentric circular arrays,” *Int. J. Ant. Propa.*, vol. 2016, ID 1852659, 2016.
[17] M. Lin, Y. Gao, P. Liu, and J. Liu, “Super-resolution orbital angular momentum based radar targets detection,” *IET Electron. Lett.*, vol. 52, no. 13, pp. 1168–1170, Jun. 2016.
[18] S. D. Coomber, C. D. Cameron, J. R. Hughes, D. T. Sheerin, C. W. Slinger, M. A. G. Smith, and M. Stanley, “Optically addressed spatial light modulators for replaying computer-generated holograms,” *Spatial Light Modulators: Technology and Applications*, vol. 4457, pp. 9–19, San Diego, CA, USA, Jul. 2001.
[19] X. Cai, J. Wang, M. J. Strain, B. J. Morris, J. Zhu, M. Sorel, J. L. O’Brien, M. G. Thompson, and S. Yu, “Integrated Compact Optical Vortex Beam Emitters,” *Science*, vol. 338, no. 6105, pp. 363-366, Oct. 2012.
[20] P. Genevet, J. Lin , M. A. Kats, and F. Capasso, “Holographic detection of the orbital angular momentum of light with plasmonic photodiodes,” *Nat. Commun.*, vol. 3, 1278, Dec. 2012.
[21] G. Rui, D. C. Abeysinghe, R. L. Nelson, and Q. Zhan, “Demonstration of beam steering via dipole-coupled plasmonic spiral antenna,” *Sci. Rep.*, vol. 3, 2237, Jul. 2013.
[22] A. Liu, X. Xiong, X. Ren, Y. Cai, G. Rui, Q. Zhan, G. Guo, and G. Guo, “Detecting orbital angular momentum through division-of-amplitude interference with a circular plasmonic lens,” *Sci. Rep.*, vol. 3, 2402, Aug. 2013.
[23] R. Niemiec, “Etude des propriétés du moment angulaire orbital des ondes électromagnétiques : développement de capteurs, transfert de moment et applications,” PhD thesis, Université de Rennes 1, France, 2014.
[24] R. Niemiec, C. Brousseau, K. Mahdjoubi, O. Emile and A. Ménard, “Characterization of an OAM flat plate antenna in the millimeter frequency band,” *IEEE Ant. Wirel. Propag. Lett.*, vol. 13, pp. 1011–1014, 2014.
[25] A. Bennis, R. Niemiec, C. Brousseau, K. Mahdjoubi, and O. Emile, “Flat plate for OAM generation in the millimeter band,” *European Conference on Antennas & Propagation (EuCAP)*, Gothenburg, Sweden, Apr. 2013.
[26] F. Tamburini, E. Mari, B. Thidé, C. Barbieri, and F. Romanato, “Experimental verification of photon angular momentum and vorticity with radio techniques,” *Appl. Phys. Lett.*, vol. 99, 204102, Nov. 2011.
[27] A. Tennant and B. Allen, “Generation of OAM radio waves using circular time-switched array antenna,” *IET Electron. Lett.*, vol. 48, no. 21, pp. 1365–1366, Oct. 2012.
[28] Q. Bai, A. Tennant, B. Allen, and M. U. Rehman, “Generation of orbital angular momentum (OAM) radio beams with phased patch array,” *Loughborough Antennas and Propagation Conference (LAPC)*, pp. 410–413, Nov. 2013.
[29] Q. Bai, A. Tennant, and B. Allen, “Experimental circular phased array for generating OAM radio beams,” *IET Electron. Lett.*, vol. 50, no. 20, pp. 1414–1415, Sep. 2014.
[30] X. Bai, R. Jin, L. Liu, J. Geng, and X. Liang, “Generation of OAM radio waves with three polarizations using circular horn antenna array,” *Int. J. Ant. Propag.*, vol. 2015, ID 132549, 2015.
[31] J. H. Poynting, “The wave motion of a revolving shaft, and a suggestion as to the angular momentum in a beam of circularly polarised light,” *Proc. R. Soc. Lond. Ser. A*, vol. 82, no. 557, pp. 560–567, Jul. 1909.
[32] C. C. Tannoudji, J. Dupont-Roc, and G. Grynberg, “Photons et atomes - Introduction à l’électrodynamique quantique,” Paris: EDP Sciences, 1987.
[33] “Angular momentum of light,” https://en.wikipedia.org/wiki/Angular_momentum_of_light
[34] M. J. Padgett, J. Arlt, N. Simpson, and L. Allen. “An experiment to observe the intensity and phase structure of Laguerre-Gaussian laser modes,” *Am. J. Phys.*, vol. 64, no. 1, pp. 77-82, Jan. 1996.

[35] L. Allen, M. J. Padgett, and M. Babiker, "The orbital angular momentum of light," *Prog. Opt.*, vol. 39, pp. 291–372, May 1999.
[36] A. E. Siegman, "Lasers." (University Science Books, 1986.)
[37] M. I. Kolobov ed., "Quantum Imaging." (Springer, 2007.)
[38] A. M. Yao and M. J. Padgett, "Orbital angular momentum: origins, behavior and applications," Advances in Optics and Photonics, vol. 3, no. 2, pp. 161–204, May 2011.
[39] M. W. Beijersbergen, R. P. C. Coerwinkel, M. Kristensen, and J. P. Woerdman, "Helical-wavefront laser beams produced with a spiral phaseplate," *Opt. Commun.*, vol. 112, pp. 321–327, Dec. 1994.
[40] G. A. Turnbull, D. A. Robertson G. M. Smith, L. Allen, and M .J. Padgett, "The generation of free-space Laguerre-Gaussian modes at millimeter-wave frequencies by use of a spiral phaseplate," *Opt. Commun.*, vol. 127, no. 4-6, pp. 183–188, Jun. 1996.
[41] P. Schemmel, G. Pisano, and B. Maffei, "A modular spiral phase plate design for orbital angular momentum generation at millimetre wavelengths," *Opt. Express*, vol. 22, no. 12, pp. 14712–14726, Jun. 2014
[42] K. Sueda, G. Miyaji, N. Miyanaga, and M. Nakatsuka, "Laguerre-Gaussian beam generated with a multilevel spiral phase plate for high intensity laser pulses," *Opt. Express*, vol. 12, no. 15, pp. 3548-3553, Jul. 2004.
[43] S. N. Khonina, V. V. Kotlyar, M. V. Shinkaryev, V. A. Soifer, and G. V. Uspleniev, "The phase rotor filter," *J. Mod. Opt.*, vol. 39, no. 5, pp. 1147–1154, 1992.
[44] G. Biener, A. Niv, V. Kleiner, and E. Hasman, "Formation of helical beams by use of Pancharatnam-Berry phase optical elements," *Opt. Lett.*, vol. 27, no. 21, pp. 1875–1877, Nov. 2002.
[45] M. Harris, C. A. Hill, and J. M. Vaughan, "Optical helices and spiral interference fringes," *Optics Commun.*, vol. 106, no. 4-6, pp. 161-166, Mar. 1994.
[46] M. W. Beijersbergen, L. Allen, H. van der Veen, and J. P. Woerdman, "Astigmatic laser mode converters and transfer of orbital angular momentum," *Opt. Commun.*, vol. 96, no. 1-3, pp.123–132, Feb. 1993.
[47] D. Gabor, "A new microscopic principle," *Nature*, vol. 161, no. 4098, pp. 777–778, May 1948.
[48] V. Bazhenov, M. S. Soskin, and M. V. Vasnetsov, "Screw dislocations in light wavefronts," *J. Mod. Opt.*, vol. 39, no. 5, pp. 985–990, 1992.
[49] N. R. Heckenberg, R. McDuff, C. P. Smith, H. Rubinsztein-Dunlop, and M. Wegener, "Laser beams with phase singularities," *Opt. Quantum. Electron.*, vol. 24, no. 9, pp. S951–S962, Sep. 1992.
[50] M. J. Padgett, J. Courtial, and L. Allen, "Light's orbital angular momentum," *Phys. Today*, vol. 57, no. 5, pp. 35–40, May 2004.
[51] J. Arlt and M. J. Padgett, "Generation of a beam with a dark focus surrounded by regions of higher intensity: the optical bottle beam," *Opt. Lett.*, vol. 25, no. 4, pp. 191-193, Feb. 2000.
[52] X. Hui, S. Zheng, Y. Hu, C. Xu, X. Jin, H. Chi, and X. Zhang, "Ultralow reflectivity spiral phase plate for generation of millimeter-wave OAM beam," *IEEE Ant. Wirel. Propag. Lett.*, vol. 14, pp. 966–969, 2015.
[53] L. Cheng, W. Hong, and Z. C. Hao, "Generation of electromagnetic waves with arbitrary Orbital Angular Momentum modes," *Sci. Rep.*, vol. 4, 4814, Apr. 2014.
[54] F. E. Mahmouli and S. Walker, "4-Gbps uncompressed video transmission over a 60 GHz Orbital Angular Momentum wireless channel," *IEEE Wirel. Commun. Lett.*, vol. 2, no. 2, pp. 223–226, Apr. 2013.

[55] F. E. Mahmouli and S. Walker, "Orbital angular momentum generation in a 60GHz wireless radio channel," *20th Telecommunications forum (TELFOR)*, Belgrade, Serbia, pp. 315-318, Nov. 2012.
[56] C.A., Balanis, "Antenna theory: analysis and design." (John Wiley and Sons, 1997, 2nd edn.)
[57] T. Akalin, J. Danglot, O. Vanbésien, and D. Lippens, "A highly directive dipole antenna embedded in a Fabry–Perot type cavity," *IEEE Microw. Wireless Compon. Lett.*, vol. 12, no. 2, pp. 48–50, Feb. 2002.
[58] H. Boutayeb, K. Mahdjoubi, A. C. Tarot, and T. A. Denidni, "Directivity of an antenna embedded inside a Fabry-Perot cavity: Analysis and Design," *Microw. Opt. Technol. Lett.*, vol. 48, no. 1, pp. 12–17, Jan. 2006.
[59] R. Gardelli, M. Albani, and F. Capolino, "Array thinning by using antennas in a Fabry–Perot cavity for gain enhancement," *IEEE Trans. Ant. Propag.*, vol. 54, no. 7, pp. 1979-1990, Jul. 2006.
[60] H. Talleb, D. Lautru, and V. Fouad Hannaa, "Characterization of electronically controlled electromagnetic band gap structures," *Eur. Phys. J. Appl. Phys.*, vol. 38, pp. 7–13, Mar. 2007.
[61] S. Enoch, G. Tayeb, P. Sabouroux, N. Guerin and P. Vincent, "A metamaterial for directive emission," *Phys. Rev. Lett.*, vol. 89, 213902, Nov. 2002.
[62] A. A. Oliner and D. R. Jackson, "Leaky-wave antennas," Chapter 11 in "Antenna Engineering Handbook," 1993.
[63] D. R. Jackson, A. A. Oliner, and A. Ip, "Leaky-wave propagation and radiation for a narrow-beam multiple-layer dielectric structure," *IEEE Trans. Ant. Propag.*, vol. 41, no. 3, pp. 344–348, Mar. 1993.
[64] G. V. Trentini, "Partially reflecting sheet arrays," *IRE Trans. Ant. Propag.*, vol. 4, no. 4, pp. 666–671, Oct. 1956.
[65] H. Boutayeb, K. Mahdjoubi and A. C Tarot, "Antenna inside PBG and Fabry-Perot cavities", *Journées Internationales de Nice sur les Antennes (JINA)*, Nov. 2002.
[66] M. Thevenot, J. Drouet, B. Jecko, T. Monediere, L. Leger, L. Freytag, R. Chantalat, and M. Diblanc, "New advancements to exploit the potentialities of the EBG resonator antennas," *IEEE Antennas and Propagation Society International Symposium*, vol. 3A, pp. 22–25, 2005,
[67] K. Mahdjoubi, T.H. Vu, A. C. Tarot, and S. Collardey, "An overview on the design and properties of EBG antennas," *European Conference on Antennas & Propagation (EuCAP)*, Barcelona, Spain, Apr. 2010.
[68] O. Ronciere, "Antennes à bande interdite électromagnétique et à cavité Fabry-Pérot reconfigurables," PhD thesis, Université de Rennes 1, France, 2007.
[69] E. Rodes. "Nouveaux concepts d'antenne à base de matériaux BIE métalliques. Application aux réseaux de télécommunications," PhD thesis, Université de Limoges, France, 2006.
[70] T. H. Vu, "Antennes à bande interdite électromagnétique directive: contribution à l'élargissement de la bande passante et à l'évaluation de l'impédance," PhD thesis, Université de Rennes 1, France, 2009.
[71] M. Sadiku, "Waveguides", Chapter 12 in "Elements of Electromagnetics." (Oxford University Press, 2001, 3rd edn)
[72] R. S. Elliott, "An introduction to guided waves and microwave circuits." (Prentice-Hall, Inc. 1993)
[73] M. Kristensen, M. W. Beijersbergen, and J. P. Woerdman, "Angular momentum and spin-orbit coupling for microwave photons," *Opt. Commun.*, vol. 104, no. 4-6, pp. 229–233, Jan. 1994.

[74] D. Zhang, X. Feng, K. Cui, F. Liu, and Y. Huang, “Generating in-plane optical orbital angular momentum beams with silicon waveguides,” *IEEE Photon. J.*, vol. 5, 2201206, Apr. 2013.

Bibliography of the author

Journals:

1. **W. L. Wei**, K. Mahdjoubi, C. Brousseau, O. Emile, "Generation of OAM waves with circular phase shifter and array of patch antennas," *IET Electronics Letters*, vol. 51, no. 6, pp. 442-443, Mar. 2015.

2. **W. L. Wei**, K. Mahdjoubi, C. Brousseau, O. Emile, "Horn antennas for generating radio waves bearing orbital angular momentum by using spiral phase plate," *IET Microwaves, Antennas & Propagation*, vol. 10, no. 13, pp. 1420-1427, Oct. 2016.

3. O. Emile, R. Niemiec, C. Brousseau, J. Emile, K. Mahdjoubi, **W. L. Wei**, B. Thide, "Mechanism of angular momentum transfer from microwaves to a copper ring," *The European Physical Journal D*, vol. 70, no. 8, 172, Aug. 2016.

Conferences:

1. **W. L. Wei**, K. Mahdjoubi, C. Brousseau, O. Emile, A. Sharaiha, "Enhancement of directivity of an OAM antenna by using Fabry-Perot cavity," *10th European Conference on Antennas and Propagation (EuCAP)*, Davos, Swizerland, Apr. 2016.

2. **W. L. Wei**, K. Mahdjoubi, C. Brousseau, O. Emile, A. Sharaiha, "Two monopole antennas for generating radio OAM waves in circular waveguide," *10th European Conference on Antennas and Propagation (EuCAP)*, Davos, Swizerland, Apr. 2016.

3. **W. L. Wei**, K. Mahdjoubi, C. Brousseau, O. Emile, "Generation of radio orbital angular momentum (OAM) waves with circular metallic waveguide," *2015 Asia-Pacific Microwave Conference (APMC)*, Nanjing, China, Dec. 2015.

4. **W. L. Wei**, K. Mahdjoubi, C. Brousseau, O. Emile, A. Sharaiha, "Horn antenna for generating orbital angular momentum (OAM) waves," *2015 Loughborough Antennas & Propagation Conference (LAPC)*, Loughborough, UK, Nov. 2015.

5. R. Niemiec, **W. L. Wei**, K. Mahdjoubi, C. Brousseau, O. Emile, "Antennas for generating electromagnetic waves bearing OAM," *1st URSI Atlantic Radio Science Conference (URSI AT-RASC)*, Las Palmas, Spain, May 2015.

VU :

Le Directeur de Thèse
(Nom et Prénom)

VU :

Le Responsable de l'École Doctorale

VU pour autorisation de soutenance

Rennes, le

Le Président de l'Université de Rennes 1

Guy CATHELINEAU

VU après soutenance pour autorisation de publication :

Le Président de Jury,
(Nom et Prénom)

Résumé

Il est bien connu dans la théorie de Maxwell que le rayonnement électromagnétique (EM) d'une onde porte à la fois du moment linéaire (énergie) et du moment angulaire. Ce dernier possède deux parties: le Moment Angulaire de Spin (ou SAM) qui est également connu sous le nom de la polarisation et le Moment Angulaire Orbital (ou OAM). Le SAM ne comprend que deux états (gauche et droite) et est utilisé en télécommunications pour doubler la capacité du canal. Par contre, le moment angulaire orbital (OAM) peut en théorie, avoir un nombre infini d'états appelés les modes OAM. Par conséquent, en radiofréquences, les premières applications de l'OAM ont été proposées dans le domaine des communications sans fil. Mais, tout d'abord, il est nécessaire de développer des antennes générant de telles ondes.

L'objectif de cette thèse est de concevoir des antennes pour générer des ondes ayant un OAM. Le manuscrit se décompose en trois parties. Dans la première partie, un réseau d'antennes « patches » utilisant un déphaseur original est développé et testé. Ce réseau génère une onde ayant de l'OAM. Dans la deuxième partie, une cavité Fabry-Perot (FP) est utilisée pour apporter plus de directivité à ce réseau d'antennes. Enfin, la troisième partie consiste à générer des ondes guidées possédant du moment OAM. Ces ondes ont ensuite été utilisées pour exciter des antennes en cornet et rayonner des faisceaux directifs transportant du moment angulaire orbital.

Mots clés: moment angulaire orbital, antenne patch, cavité Fabry-Perot, antenne à cornet, antenne à guide d'onde, lame de phase spirale.

Abstract

It is well known from Maxwell's theory that electromagnetic (EM) radiation carries both linear momentum (energy) and angular momentum. The latter has two parts: Spin Angular Momentum (SAM) which corresponds to the polarization of an EM wave and Orbital Angular Momentum (OAM) which is associated with the spatial distribution of an EM wave. The SAM has only two states (left and right) and is used to double the channel capacity in telecommunications. On the other hand, the OAM can theoretically have an infinite number of states called the OAM modes. Therefore, the first applications of OAM have been proposed in wireless communications at radio frequencies. However, first of all, it is necessary to develop the antennas for generating such waves.

The objective of this thesis is to design the antennas for the generation of radio waves bearing OAM. The manuscript contains three parts. In the first part, an antenna using 4 patches and an original phase shifter is developed and tested to generate an OAM wave. In the second part, a Fabry-Perot (FP) cavity is used to enhance the directivity of this antenna. The third part is to generate guided OAM waves. Some horn antennas are used to radiate these waves with good directivity.

Key words: orbital angular momentum, patch antenna, Fabry-Perot cavity, horn antenna, waveguide antenna, spiral phase plate.